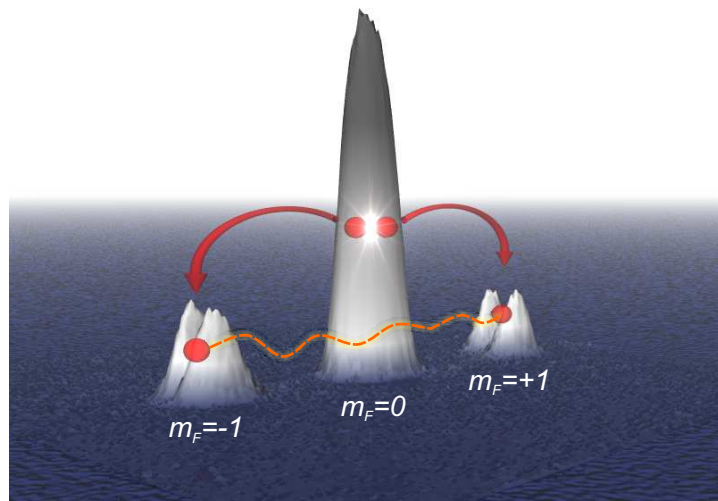


Multi-particle entanglement in a spinor Bose-Einstein condensate for quantum-enhanced interferometry



Von der Fakultät für Mathematik und Physik der
Gottfried Wilhelm Leibniz Universität Hannover

zur Erlangung des Grades

Doktor der Naturwissenschaften
- Dr. rer. nat. -

genehmigte Dissertation von

Dipl.-Phys. Bernd Lücke,
geboren am 30.11.1982 in Clausthal-Zellerfeld

2014

Referent: Prof. Dr. Wolfgang Ertmer

Korreferent: Prof. Dr. Jan Arlt

Korreferent: Prof. Dr. Luis Santos

Tag der Promotion: 05. 06. 2014

Zusammenfassung

Die kontrollierte Erzeugung von Verschränkung ist eine zentrale Voraussetzung für die Verwirklichung vieler Quantentechnologien. Neben weiteren Anwendungen kann Verschränkung genutzt werden, um abhörsichere Quantenkommunikation zu ermöglichen, um Quantencomputer zu realisieren, die bestimmte Aufgaben um ein Vielfaches schneller lösen als derzeitige Rechner und um Präzisionsmessungen zu verbessern. Insbesondere kann die Genauigkeit von Atominterferometern erhöht werden, die Rotation, Beschleunigung, Zeit und viele weitere Größen mit höchster Präzision vermessen. Je mehr Teilchen für die Interferometrie verwendet werden, desto genauer werden diese Sensoren. Daher ist die Verschränkung möglichst großer Ensembles wünschenswert. Die Herstellung solcher hochgradig nicht-klassischen Zustände stellt eine große Herausforderung dar, da diese für große Teilchenzahlen zunehmend fragil und sensitiv auf Störeinflüsse werden.

Im Rahmen dieser Arbeit wurden kohärente atomare Stöße in einem ^{87}Rb Bose-Einstein Kondensat untersucht, die Atome vom Zeeman-Zustand $m_F = 0$ nach $m_F = +1$ und $m_F = -1$ transferieren. Durch diesen Prozess, der als Spindynamik bezeichnet wird, entsteht ein hochgradig verschränkter Spin-Zustand mit bis zu 10 000 Teilchen, der einem idealen Dicke-Zustand sehr nahe kommt. Wir messen einen verallgemeinerten spin-squeezing Parameter von $-11.4(5)$ dB, was den besten veröffentlichten Wert in atomaren Ensembles darstellt. Mit einem neuen Kriterium konnte Vielteilchen-Verschränkung nachgewiesen werden. Das Ensemble enthält Gruppen von 68 verschränkten Teilchen, die nicht separierbar sind und als ein einziges quantenmechanisches Objekt beschrieben werden müssen.

Darüber hinaus wurde experimentell gezeigt, dass der verschränkte Zustand genutzt werden kann, um in einem neuartigen Interferometer Genauigkeiten jenseits des klassischen Limits zu erreichen. Das untersuchte Verfahren weist somit neue Wege zur Steigerung der Präzision von Sensoren durch Verschränkung auf.

Abstract

The well-controlled creation of entanglement is a key requirement for many quantum technologies. Besides other applications, entanglement is useful to establish tap-proof quantum communication, to realize a quantum computer capable of solving specific tasks in a fraction of the time needed by today's fastest computers and for the improvement of precision measurements. Of particular interest is the precision enhancement of atom interferometers for exact measurements of time, rotation, acceleration and many other quantities. Interferometry with a larger number of particles can reach higher precision. Therefore, it is desirable to create large ensembles of entangled atoms. However, the preparation of such highly non-classical states is challenging since they become increasingly fragile and sensitive to noise for larger particle numbers.

In this work, we studied coherent collisions in a ^{87}Rb Bose-Einstein condensate which transfers atoms from the $m_F = 0$ Zeeman state to $m_F = +1$ and $m_F = -1$. This process is called spin dynamics and creates a highly entangled spin state of up to 10 000 atoms close to an ideal Dicke state. We measure a generalized spin-squeezing parameter of $-11.4(5)$ dB, the best value reported for any atomic system. With a new criterion we were able to confirm many-particle entanglement. The ensemble contains groups of 68 entangled particles that are non-separable and have to be treated as one quantum object.

Furthermore, we demonstrated experimentally that the entangled state can be used in a new type of interferometer to obtain sensitivities beyond the classical limit. Hence, our experiments demonstrate new methods to enhance the precision of sensors by entanglement.

Contents

1. Introduction	1
2. Entanglement and interferometry	5
2.1. Entanglement	5
2.1.1. Entanglement and the intriguing quantum world	5
2.1.2. Formal definition of entangled states	7
2.2. Limits of interferometric sensitivity	9
2.2.1. The shot-noise limit of interferometric phase sensitivity	9
2.2.2. Quantum-enhanced interferometry and the Heisenberg limit	10
2.3. The Bloch sphere representation	12
2.3.1. The single-particle Bloch sphere	12
2.3.2. The multi-particle Bloch sphere	14
2.3.3. The Heisenberg uncertainty for phase and particle number difference	15
2.3.4. The interferometer sequence in the Bloch sphere representation .	16
2.4. Spin squeezing and entanglement	18
2.4.1. Interferometric gain and the spin-squeezing parameter	18
2.4.2. The spin-squeezing parameter as an entanglement witness	19
2.5. The phase sum and the total number of particles	20
3. Spin dynamics	23
3.1. Spin-changing collisions	23
3.2. Analogy to parametric down conversion	24
3.3. Theoretical description	25
3.4. Spin dynamics resonances	27
3.5. Properties of the two-mode squeezed vacuum	30
3.6. Beyond the parametric approximation	33
4. Preparation, manipulation and detection of a ^{87}Rb spinor condensate	35
4.1. Preparation of the initial ^{87}Rb condensate	35
4.2. Manipulation of the energy levels via microwave dressing	36
4.3. Manipulation of the internal states via microwave pulses	39
4.4. High precision absorption detection	42
4.4.1. Techniques for atom detection	43
4.4.2. Calculating the number of atoms from an absorption signal	44
4.4.3. Calibration of the absolute number of atoms	46
4.4.4. Photo-electron shot noise - the fundamental limit	50

4.4.5.	The setup for the high-precision absorption detection	52
4.4.6.	Estimation of the detection noise	54
5.	The twin-Fock interferometer	57
5.1.	Beyond spin squeezing	57
5.2.	The principle of the twin-Fock interferometer	58
5.3.	Experimental creation of twin-Fock states	59
5.4.	Measurement of sub-shot-noise number fluctuations	61
5.5.	Estimation of the sensitivity gain	62
5.6.	Sensitivity limit set by the detection noise	64
6.	Multi-particle entanglement in a spinor Bose-Einstein condensate	67
6.1.	Entanglement detection based on measurements of the collective spin . .	67
6.2.	Spin dynamics in $F=1$	69
6.3.	Estimation of the generalized spin-squeezing parameter	71
6.4.	Detection of multi-particle entanglement in spin-squeezed ensembles . .	73
6.5.	A new criterion for multi-particle entanglement	77
6.6.	Characterization of the multi-particle entanglement	79
7.	Outlook	81
7.1.	Improving the detection system	81
7.1.1.	Precision limits of absorption detection	81
7.1.2.	Fluorescence detection	83
7.2.	The Fock interferometer	85
A.	Symmetric spin states	89
A.1.	Spin length of symmetric states	89
A.2.	Number squeezing and entanglement of symmetric states	90
B.	The spin-squeezing parameter as an entanglement witness	93
C.	Time evolution of the K-vector	95
D.	CCD camera calibration	97
D.1.	Calibration of the camera gain	97
D.2.	Calibration of the quantum efficiency	98
E.	Statistically correct error bars for estimated variances	101
E.1.	Augmented and monomial symmetric functions	102
E.2.	$\text{var}(\hat{\mu}_2)$ in terms of μ_4 and μ_2^2	102
E.3.	Finding estimators for μ_4 and μ_2^2	103
E.4.	The estimator for $\text{var}(\hat{\mu}_2)$	104

1. Introduction

”I would not call [entanglement] *one* but rather *the* characteristic trait of quantum mechanics, the one that enforces its entire departure from classical lines of thought” (Schrödinger) [1].

Quantum entanglement describes a type of intriguing correlations that are only observed in the microscopic quantum world and do not appear in our macroscopic world. For larger macroscopic systems, this fascinating quantum phenomenon disappears. The transition from the intriguing microscopic world governed by quantum mechanics to the macroscopic world described by classical physics, that we experience in everyday life, is not yet completely understood [2]. The quantum features of large systems become fragile due to an increasing sensitivity to environmental noise sources which leads to strong decoherence of many-particle entangled states. A small coupling to the environment is sufficient to destroy the quantum mechanical features of such a state and the system will start to behave classically. Hence, the creation of large systems containing massive entanglement is very challenging. On the other hand, such states are a key resource for the implementation of many exciting quantum technologies. Therefore, researchers all over the world try to entangle as many particles as possible pushing the system further towards the macroscopic regime.

Experimental efforts to achieve entanglement between more than two particles started in 1999, when the group of A. Zeilinger succeeded in creating a Green-Horn-Zeilinger state of 3 entangled photons [5]. Only one year later, the group of D. Wineland demonstrated the entanglement of 4 ions [6]. Since then, new multi-particle entanglement records for ions have been reported by the group of R. Blatt achieving the entanglement of up to 14 ions [3, 7], and new records for photons have been reported by the group of J.W.Pan achieving the entanglement of up to 8 photons [4, 8, 9]. Other systems like super-conducting qubits [10, 11] and nitrogen-vacancy defect centres in diamond [12] have been used to create tripartite entanglement.

These implementations have the advantage of providing manipulation and read-out of the individual constituents with high fidelity. The most prominent prospect application for these systems is the so-called quantum computer, that can perform specific calculations in a fraction of the time needed by today’s best computers. The main challenge in building such a quantum computer is to scale the system up to larger and larger numbers of constituents. This up-scaling is hindered by the increased sensitivity to environmental noise described above.

In contrast to the ”bottom-up” approach offered by these systems, squeezed ensembles of ultra-cold atoms provide a ”top-down” approach. These ensembles contain a large number of particles that can be entangled by various mechanisms. A breakthrough result has been achieved in 2010 by the group of M. Oberthaler. They created a spin-squeezed

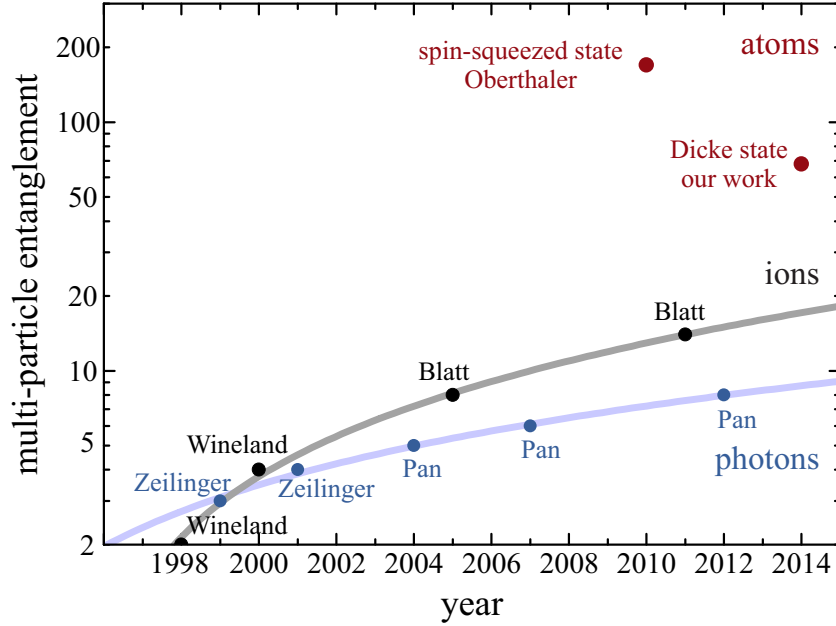


Figure 1.1.: **Multi-particle entanglement.** Starting in the late nineties, experiments using photons and ions were able to experimentally create and detect multi-particle entanglement with an increasing number of entangled particles. The largest numbers in these system have been reported by the group of R. Blatt achieving the entanglement of 14 ions [3] and by the group of J. W. Pan achieving the entanglement of 8 photons [4]. In 2010 the group of M. Oberthaler demonstrated massive multi-particle entanglement in a spin-squeezed ensemble of neutral atoms containing non-separable groups of 170 entangled atoms. In our work we demonstrate the preparation of substantial multi-particle entanglement of neutral atoms in a new class of states: the Dicke states.

state and showed that it contains more than 80-particle entanglement with a 3 standard deviation uncertainty level [13]. Moreover, the mean values of their measurements indicates a multi-particle entanglement of 170 atoms. However, the control and detection on the single particle level is hard to obtain in these systems. The most prominent application of highly entangled many-particle states of ultra-cold atoms is quantum enhanced interferometry.

Many of today's most precise sensors are interferometers. A common application is the CD- or DVD-Player, which is based on a laser interferometer that precisely scans the disk surface to read the stored data. High-precision laser interferometers are used for gravitational wave detection [14, 15], the measurement of the earth's rotation [16] and for many other tasks, including rotation and acceleration sensors for navigation. A comparably new emerging technique is interferometry with atoms. For many applications, they have the potential to outperform interferometers operated with coherent laser light. Moreover, they can measure quantities that are not accessible to interferometers

operated with light. Most prominently, the legal time is based on time measurements performed by atomic clocks. The global positioning system (GPS) uses atomic clocks on satellites to precisely synchronise the emitted signals and enable the high spatial resolution of GPS. Other applications feature the measurement of inertial forces, magnetic [17] and microwave fields [18]. The precise measurement of earth's rotation [19–21] and gravity [22] is of importance for applications in geodesy [23, 24].

The sensitivity of interferometers is fundamentally limited by the so-called shot noise. It scales as $\frac{1}{\sqrt{N}}$ with the number of particles N . Hence, the sensitivity can be improved by using more particles. However, this may lead to technical problems like high collision rates and losses due to increased densities in the case of atom interferometers. Additionally, it is favorable to use a very pure ensemble of coherent atoms, the so-called Bose-Einstein condensate (BEC), for atom interferometry, which provides a very high degree of control and thus reduced noise. The very narrow velocity distribution of a BEC leads to low expansion rates during free fall, which allows for long evolution times, efficient detection and beam splitting processes for inertial measurements. For gravimeters, the start position, which defines the reference point of the gravitational potential, can be precisely defined. As an example, this will be of particular importance for future experiments like the very long baseline atom interferometer (VLBAI), that will be build in Hanover. For this interferometer, atoms will be dropped in a 10 m vacuum tube, which allows for very long free-fall times and a precise test of Einsteins equivalence principle in a differential measurement. However, due to technical limitations, such a BEC contains less atoms than a thermal ensemble. Hence, shot noise is a severe limitation of the achievable performance of atom interferometers operated with BECs. In order to overcome this limitation, entangled atoms can be used. Ideally, this allows to reach the Heisenberg limit of sensitivity which scales with $\frac{1}{N}$. Hence, interferometry with 10 000 entangled particles can yield a 100-fold improved sensitivity compared to interferometry with the same number of uncorrelated particles. This shows the potential of multi-particle entangled ensembles for the improvement of interferometric sensors. However, it is a challenge to prepare such a mesoscopic state of multi-particle entangled atoms.

The techniques for the creation of multi-particle entanglement in ensembles of neutral atoms can be divided into two groups: (i) entanglement by atom-light interaction and (ii) entanglement by interatomic collisional interaction. The most mature concepts using atom-light interactions rely on the well-developed methods for the preparation and detection of light to generate and read out multi-particle entangled states of neutral atoms. These concepts can be applied to room-temperature vapour cells [25], laser-cooled atoms [26] and BECs [27]. Techniques based on interatomic collisions make use of the well-controllable ultra-cold collisions in a BEC. These collisions can add up to a mean nonlinear interaction, which is analogous to a χ^3 -nonlinearity in an optical crystal. Such a source of entanglement has been first demonstrated using external states in a double-well potential [28] and later in the spin degree of freedom [13, 29]. This method allowed for sub-shot-noise interferometry with spin-squeezed states [13].

In this work, we have investigated coherent spin-changing collisions in a ^{87}Rb Bose-Einstein condensate (BEC) as a tool for the creation of multi-particle entanglement. The underlying Hamiltonian of the process is formally equivalent to the Hamiltonian

1. Introduction

of parametric down-conversion in optics - a well established method for the creation of entangled photons based on the χ^2 -nonlinearity in an optical crystal. In prior work, our group has developed a detailed understanding of spin-dynamics resonances [30] and demonstrated the amplification of pure vacuum fluctuations [31], which are important prerequisites for the production of entanglement. Parallel to the work presented here, the group of M. Oberthaler demonstrated a proof of entanglement based on a homodyne measurement [32] and the group of M. Chapman observed spin-nematic squeezing [33] in ensembles created by spin-dynamics.

Here, we characterize the state produced by spin dynamics and show that it is close to a highly entangled Dicke state. We measure a generalized spin-squeezing parameter of $-11.4(5)$ dB, the largest reported value in any atomic system. By employing a newly developed entanglement measure, we find that the state contains 68-particle entanglement [34]. Furthermore, we prove that the created state is useful for quantum-enhanced interferometry [35]. Compared to other proof-of-principle experiments, the large number of 10 000 particles in the entangled ensemble provides a perspective for highly sensitive measurements in a new generation of atom interferometers.

This thesis is organized as follows: In chapter 2, the basic theory of entanglement is described and its connection to sensitivities below the shot-noise limit is discussed. The generalized Bloch sphere is introduced, a useful tool to visualize the action of an interferometer and entangled multi-particle states. In chapter 3, the theory of spin-changing collisions is explained and the properties of the state created by spin dynamics are discussed. In chapter 4, a new type of interferometer is introduced which can make use of the entanglement of this state to reach a sensitivity beyond the shot-noise limit. In chapter 5, the entanglement of the state created by spin dynamics is characterized in detail using new methods. Finally, an outlook on future improvements for the detection and characterization of the multi-particle entangled state is given and a possible application for a new type of interferometer is presented.

2. Entanglement and interferometry

2.1. Entanglement

2.1.1. Entanglement and the intriguing quantum world

Quantum mechanics is one of the most successful physical theories, especially well suited for describing the microscopic world. Although its mathematical treatment is well known, some conceptional points of quantum mechanics are very puzzling as they seem to be contradictory to the reality that we experience in the macroscopic world.

One of these puzzling features of quantum mechanics is the existence of superposition states. For example, a particle can be at two places at the same time. When its position is measured it will be found at either of the two places. Nonetheless, the particle was in a superposition of being at place one and two, since there is no way to know the outcome of this measurement in advance. Even though we may have all possible information about the quantum mechanical state of the particle at hand the measurement result remains unpredictable. Its position cannot be assigned to one place only.

”God doesn’t play dice.”, Einstein said. Every randomness, he believed, is only subjective randomness due to a lack of information. Thus, he concluded, quantum mechanics does not give us all the necessary information and must be incomplete. Ironically, when he tried to prove his statement with his colleagues Podolsky and Rosen he made the first step to reveal another counter-intuitive constituent of quantum mechanics: entanglement.

The Einstein-Podolsky-Rosen thought experiment

The quantum mechanical state describing the motion of a particle allows the prediction of the mean result of a position and a momentum measurement. It also predicts the fluctuations for these measurements. However, it never predicts the exact result of both measurements. The product of the fluctuations Δx and Δp of these measurements have to be larger than Planck’s constant \hbar

$$\Delta x \Delta p \geq \hbar. \quad (2.1)$$

This famous Heisenberg uncertainty principle cannot be surpassed by any measurement device. Hence, every measurement described in the framework of quantum mechanics is subject to random fluctuations and position and momentum cannot be precisely defined at the same time. Einstein, Podolsky and Rosen tried to show that this lack of a precise prediction of measurement results is due to an incompleteness of quantum mechanics.

2. Entanglement and interferometry



Figure 2.1.: **Correlated particles.** In their famous thought experiment, Einstein, Podolsky and Rosen considered two particles from a common source with opposite position and momentum.

Einstein et al. presented the following famous thought experiment [36]: Two particles emerge from a common source and fly in opposite direction. They are correlated such that they have opposite momentum $p_1 = -p_2$ and position $x_1 = -x_2$. Hence, a position measurement of particle one can be used to predict the result of a position measurement of particle two. The uncertainty of this prediction $\Delta(x_2 + x_1)$ is always zero in the ideal case. In the same way, the result of a momentum measurement of particle one can be used to predict the result of a momentum measurement of particle two with an uncertainty $\Delta(p_2 + p_1)$. Only one of these two possible measurements can be performed with high precision due to Heisenbergs uncertainty principle. Nonetheless, particle one seems to carry all the information about both, momentum and position of particle two. Einstein et al. gave an explicit example of a quantum mechanical state with

$$\Delta(x_2 + x_1)\Delta(p_2 + p_1) < \hbar \quad (2.2)$$

They concluded that position and momentum of particle two are defined better than allowed by quantum mechanics according to Eq. (2.1).

The only way around this conclusion is, that the measurement performed on particle one changes the state of particle two, as Einstein et al. pointed out. In addition, this change must depend on whether position or momentum was recorded. However, this seems to lead to a contradiction to Einstein's special relativity theory. The time a signal needs to travel from particle one to particle two is at least $t = c(x_1 - x_2)$ as it travels at maximum with the speed of light c . Assume that position or momentum of both particles are measured simultaneously faster than t . Then, no information if momentum or position of particle one is measured can reach the position of particle two before the measurement is complete.

There are two possible explanations for the paradox: First, quantum mechanics might be incomplete and position and momentum of a particle can be defined with a higher precision in the framework of some other more precise theory. In such theories, exact values for the outcome of position-, momentum- and other measurements are encoded in so-called hidden variables. If such hidden variables exist, quantities like momentum and position are "real" even before they are measured - an assumption called realism. This in contrast to quantum mechanics, which predicts that in general position and momentum do not have a definite value before they are measured. Additionally, Einstein et al. envisioned that such a theory beyond quantum mechanics has to be local, meaning that distant events have no faster-than-light effects on local measurements. The discovery of Bell's inequalities [37] made it possible to experimentally address the question if a theory based on local realism can be a proper replacement of quantum mechanics. Most

prominently, A. Aspect [38, 39] showed that local realism is not compatible with the measurement results of his experiments. Consequently, locality, realism or even both assumptions have to be wrong. Moreover, experiments by S. Görrblacher suggest that it is not enough to reject locality only [40]. In summary, there is some evidence that quantum mechanics gives a correct and complete description of the microscopic world.

Hence, today most physicist agree that the second way to resolve the paradox has to be the correct one: The measurement on particle one actually has an instantaneous non-local effect on particle two. The two particles cannot be treated independently and are said to be in an entangled state. Despite the described instantaneous non-local effect of a measurement, this does not imply a contradiction to special relativity. There is no way to exploit this Einstein-Podolsky-Rosen (EPR) entanglement for the transmission of a signal [41].

2.1.2. Formal definition of entangled states

After this review of the history of entanglement let us now turn to the formal definition of entanglement following Ref. [42]. For this purpose we consider a physical system that can be divided into several subsystems such that the overall Hilbert space is a tensor product of the subsystems' Hilbert spaces:

$$\mathcal{H} = \otimes_{i=1}^N \mathcal{H}^{(i)} \quad (2.3)$$

In this work, the subsystems will correspond to the individual particles, but in other settings, they might for example correspond to different regions in space or to different internal degrees of freedom. If the system is in a pure state and it is possible to find normalized states $|\psi^{(i)}\rangle \in \mathcal{H}^{(i)}$ such that the overall state can be written as

$$|\Psi\rangle = |\psi^{(1)}\rangle \otimes |\psi^{(2)}\rangle \otimes \dots \otimes |\psi^{(N)}\rangle \quad (2.4)$$

the state is called separable. Such a state can be written as a density matrix

$$\rho = \rho_k^{(1)} \otimes \rho_k^{(2)} \otimes \dots \otimes \rho_k^{(N)} \quad (2.5)$$

with the density matrix $\rho^{(i)} = |\psi^{(i)}\rangle \langle \psi^{(i)}|$ describing the state of the i th subsystem. Obviously, for such uncorrelated states the measurement of some observable A_i on subsystem i does not influence the outcome of measurements performed on the other subsystems. For a compound observable $A^{(1)} \otimes A^{(2)} \otimes \dots \otimes A^{(N)}$ the expectation value is just the product of the individual expectation values

$$\langle A \rangle_\rho = \langle A^{(1)} \rangle_{\rho^{(1)}} \langle A^{(2)} \rangle_{\rho^{(2)}} \dots \langle A^{(N)} \rangle_{\rho^{(N)}} \quad (2.6)$$

and we see that there are no correlations between the measurements performed on the individual subsystems.

Otherwise, of course, there can be classical correlations present. For example, if two particles can be in a spin up $|\uparrow\rangle$ or a spin down $|\downarrow\rangle$ state an apparatus might produce a

2. Entanglement and interferometry

state $|\uparrow\rangle \otimes |\downarrow\rangle$ in 50% of the cases and a state $|\downarrow\rangle \otimes |\uparrow\rangle$ otherwise. While the orientation of an individual spin is random, the two spins will always be anti-parallel and thus correlated. A general state in the presence of classical correlations can be written in the form

$$\rho = \sum_k p_k \rho_k^{(1)} \otimes \rho_k^{(2)} \otimes \cdots \otimes \rho_k^{(N)} \quad (2.7)$$

which arises for example if the uncorrelated states $\rho_k^{(1)} \otimes \rho_k^{(2)} \otimes \cdots \otimes \rho_k^{(N)}$ are produced with probability p_k . States that can be written in this form are called separable. If we cannot write the state in this form, there must be more than classical correlations and the state is called entangled.

Note, that the opposite is not true. There are separable non-entangled states exhibiting quantum correlations [43].

Indistinguishable particles

A definition of entanglement as given above is problematic in the case of indistinguishable particles. For instance, if the Hilbert space of an individual Boson is $\mathcal{H}^{(i)}$, the Hilbert space of the compound system of indistinguishable Bosons is no longer the full tensor product space $\mathcal{H} = \otimes_{i=1}^N \mathcal{H}^{(i)}$ but only the symmetric subspace with respect to particle exchange. In the case of Fermions, the compound system can only be in the antisymmetric subspace. As the particles are indistinguishable it is fundamentally not possible to perform a measurement on an specific particle since we have no means to label them. One may argue that an EPR paradox as described in the previous section cannot be achieved, since it is not possible to talk about a particle one and a particle two. However, the notion of non-separable states is still correct and such states cannot be found in any classical theory. We will see that non-separable states are a useful resource to achieve interferometric sensitivity beyond the classical limit.

Furthermore, additional degrees of freedom can be used to distinguish particles in non-separable states and thereby make an EPR paradox possible. As a simple example, consider two Bosons with an external degree of freedom, their position in space which can be either left $|L\rangle$ or right $|R\rangle$, and an internal degree of freedom, their spin that can be either up $|\uparrow\rangle$ or down $|\downarrow\rangle$. Let us assume the system is prepared in the non-separable, symmetric state

$$|\Psi\rangle = \frac{1}{2} (|L, R\rangle + |R, L\rangle) \otimes (|\uparrow, \downarrow\rangle + |\downarrow, \uparrow\rangle) \quad (2.8)$$

Upon measurement of the position only, one particle will be found on the left side while the other will be found on the right side and they will thus become distinguishable by their position. The spin state is not changed by this measurement. If it was initially non-separable as in our example it will be non-separable after the measurement. An extension of this idea leads to the so-called dilute cloud argument as described in Ref. [44].

Consider a cloud of ultracold, indistinguishable atoms with a non-separable spin. After we turn off the confining trap the cloud of atoms will expand. If the cloud is sufficiently dilute it becomes very unlikely to find more than one atom in a small region of space. By performing a measurement with a high spatial resolution, we can thus distinguish

the particles by their position. Ideally, neither the expansion nor the position detection changes the spin state which can be checked by a subsequent measurement of the spin state. This thought experiment shows that local operations and classical communication (LOCC) are sufficient to distinguish initially indistinguishable particles while keeping them in a non-separable state. Hence, we see again that the non-separability is the crucial ingredient. For the rest of this work we thus equate non-separability with entanglement as it is usually done in the field [45].

2.2. Limits of interferometric sensitivity

As we have seen in section 2.1.1, the existence of quantum entanglement was initially revealed in the context of very fundamental and even philosophical questions about physical reality. Since then, it has become apparent that it is also a valuable resource for many applications. Entanglement is a key ingredient for quantum simulation [46] and quantum information, including quantum computation and communication [47].

In this section, we will see that entanglement can enhance the sensitivity of interferometers. Since today's most sensitive sensors for time [48], length [49], acceleration [50], rotation [16] and other quantities are based on interferometry, this application for entangled particles is of particular importance.

2.2.1. The shot-noise limit of interferometric phase sensitivity

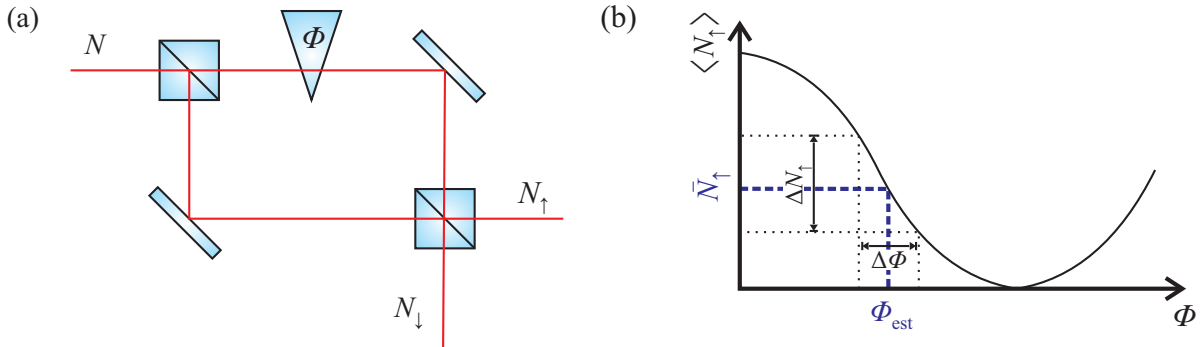


Figure 2.2.: **Typical classical interferometer.** (a) N particles enter the interferometer at one input port while the other one is left empty. After the first beam splitter each particle is in a superposition of state one (depicted as upper path) and state two (lower path). Some quantity of interest q that we seek to measure causes a phase shift ϕ on the upper state. At the second beam splitter this phase shift effects the mean particle number $\langle N_{\uparrow} \rangle$ and $\langle N_{\downarrow} \rangle$ measured at the output ports. (b) These mean particle numbers can thus be used to estimate the phase ϕ and thereby q .

Without correlations, the sensitivity of interferometers is limited by the so-called shot-noise limit. In order to understand the origin of shot noise, consider an interferometer

2. Entanglement and interferometry

operated with N uncorrelated particles as sketched in Fig. 2.2. In such an interferometer, the first beam splitter transfers each particle in a superposition of two states, here depicted as two distinct paths. One state experiences a phase shift ϕ . Subsequently, the two states are combined at a second beam splitter and the number of particles at each output port is measured.

The interferometer is designed such that the phase shift ϕ depends on the quantity that we seek to measure. Hence, an improved estimation of the phase results in an improved interferometric sensor. This phase estimation is based on the number of particles that have been detected at the output ports. Due to the interference at the second beam splitter the probability to find an individual particle at the first output port $p = \cos^2(\phi/2)$ depends on the phase ϕ . Hence, by measuring the mean number of particles \bar{N}_\uparrow at this port we can estimate the probability $p_{\text{est}} = \bar{N}_\uparrow/N$ and the phase $\phi_{\text{est}} = 2 \arccos(\sqrt{p_{\text{est}}})$.

However, since every particle appears randomly at either of the two output ports, the number of particles N_\uparrow and the estimated phase ϕ_{est} fluctuate. The resulting phase estimation error can be calculated by standard error propagation, knowing that the binomial distribution of N_\uparrow has a standard deviation of $\Delta N_\uparrow = \sqrt{Np(1-p)}$.

$$\Delta\phi_{\text{est}} = \frac{\Delta N_\uparrow}{\left(\frac{\partial \langle N_\uparrow \rangle}{\partial \phi}\right)} = \frac{1}{\sqrt{N}} \quad (2.9)$$

This fundamental phase estimation error is known as the shot noise limit. Interestingly, it is independent of the phase ϕ if no technical noise is present. It can be improved by repeating the measurement m times to

$$\Delta\phi_{\text{est}} = \frac{1}{\sqrt{mN}} \quad (2.10)$$

for a simple reason: Since the particles are completely independent, averaging over N particles is statistically the same as averaging over $m = N$ realizations with only one particle. Hence, the phase estimation error only depends on mN . Obviously, this changes in the case of correlated particles, potentially leading to an increased sensitivity as we will see now.

2.2.2. Quantum-enhanced interferometry and the Heisenberg limit

Interferometers with correlated particles can have more general probability distributions, while uncorrelated particles lead unalterably to a binomial distribution of the atom number N_\uparrow measured at one output port. Correlated states leading to more complex distributions with narrow features can improve the phase estimation error. The most prominent example of such states, the so-called spin-squeezed states, will be presented in section 2.4.

In section 2.3.3, we will prove the Heisenberg uncertainty between phase difference and particle number difference of two states

$$\Delta(\phi_\uparrow - \phi_\downarrow)\Delta(N_\uparrow - N_\downarrow) \geq 1. \quad (2.11)$$

This uncertainty leads to a more fundamental precision limit for interferometric phase estimation [51]. If ϕ_{\uparrow} is the phase of one state in between the beam splitters of the interferometer and ϕ_{\downarrow} is the phase of the other state, the phase ϕ we seek to measure is given by the difference $\phi = \phi_{\uparrow} - \phi_{\downarrow}$. The largest possible fluctuations of the particle number difference in these states is $\Delta(N_{\uparrow} - N_{\downarrow}) = N$ if the interferometer is operated with N particles. Hence, due to the Heisenberg uncertainty, the phase ϕ is fundamentally only defined to a precision

$$\Delta\phi \geq \frac{1}{N}. \quad (2.12)$$

This fundamental limit is called Heisenberg limit and cannot be surpassed even with entangled states. Note that the same argument for binomial number fluctuations $\Delta(N_{\uparrow} - N_{\downarrow}) = \sqrt{N}$ leads again to the shot-noise limit of phase estimation $\Delta\phi_{\text{est}} \geq 1/\sqrt{N}$.

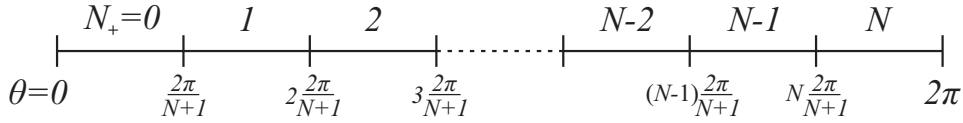


Figure 2.3.: **Intuitive illustration of the Heisenberg limit.** Each possible outcome of a measurement of N_{\uparrow} is associated with an interval in the continuous spectrum of the phase difference ϕ . The width of the intervals is proportional to $1/(N+1) \approx 1/N$ and sets a limit to the precision of the phase measurement.

An intuitive but imprecise way to understand the Heisenberg limit is depicted in Fig. 2.3. Having only a limited number of N particles there are only $N+1$ possible results for a measurement of N_{\uparrow} . In order to use these results to estimate the phase, we have to artificially divide the continuous spectrum of ϕ in $N+1$ intervals, each corresponding to one possible result. The width of such an interval is proportional to $1/(N+1) \approx 1/N$ and gives the precision of the estimate ϕ_{est} .

Hence, the phase estimation error reaches at best Heisenberg scaling $\Delta\phi_{\text{est}} \propto 1/N$. However, the estimation of the quantity of interest q_{est} causing the phase shift can have a better scaling, if the phase shift depends on the number of particles $q = f(N, \phi)$. Error propagation results in an estimation error of

$$\Delta q_{\text{est}} = \frac{\Delta\phi_{\text{est}}}{\left(\frac{\partial f(N, \phi)}{\partial \phi}\right)} \geq \frac{1}{N \left(\frac{\partial f(N, \phi)}{\partial \phi}\right)}. \quad (2.13)$$

Provided that $f(N, \phi) \propto N^x$, a scaling of $\Delta q_{\text{est}} \propto 1/N^{x+1}$ is possible. This can be realized with interactions that are nonlinear in the atom number and has been demonstrated in Ref. [52]. Nonetheless, the estimation of the *phase* is still restricted by the Heisenberg limit.

For a fluctuating number of atoms N , the Heisenberg limit would naively be formulated as

$$(\Delta\phi_{\text{est}})^2 = \frac{1}{\langle N \rangle^2}. \quad (2.14)$$

2. Entanglement and interferometry

However, as pointed out in Ref. [53], the correct limit for the achievable phase sensitivity is

$$(\Delta\phi_{\text{est}})^2 = \frac{1}{\langle N^2 \rangle}, \quad (2.15)$$

in the case of a fluctuating total number of atoms N . This limit is sometimes referred to as the Hofmann limit [54]. Since the fluctuations of the total number of atoms are typically on the shot-noise level $(\Delta N)^2 \sim N$ for most experiments, the Hofmann limit and the Heisenber limit coincide for large particle numbers $\langle N^2 \rangle = \langle N \rangle^2 + (\Delta N)^2 \approx \langle N \rangle^2$.

2.3. The Bloch sphere representation

In this section, we define the collective spin of an ensemble of two-level particles. This can be represented on a generalized Bloch sphere, which gives a geometric visualization of the ensembles state and of manipulations performed on the many-particle state. As important examples, we describe the beam splitting process and an interferometric sequence in the Bloch sphere picture.

2.3.1. The single-particle Bloch sphere

For a single particle in a two level system, it is always possible to define one of the states of an orthonormal normalized basis as spin up $|\uparrow\rangle$ and the other one as spin down $|\downarrow\rangle$. The (pseudo) spin operators s_x, s_y and s_z measuring the spin along orthonormal directions of such a spin-1/2 system with respect to this basis are defined as [55]

$$s_x = \frac{1}{2}(|\downarrow\rangle\langle\uparrow| + |\uparrow\rangle\langle\downarrow|) = \frac{1}{2} \begin{pmatrix} 0 & 1 \\ 1 & 0 \end{pmatrix} = \frac{1}{2}\sigma_x \quad (2.16)$$

$$s_y = \frac{1}{2i}(|\downarrow\rangle\langle\uparrow| - |\uparrow\rangle\langle\downarrow|) = \frac{1}{2} \begin{pmatrix} 0 & -i \\ i & 0 \end{pmatrix} = \frac{1}{2}\sigma_y \quad (2.17)$$

$$s_z = \frac{1}{2}(|\uparrow\rangle\langle\uparrow| - |\downarrow\rangle\langle\downarrow|) = \frac{1}{2} \begin{pmatrix} 1 & 0 \\ 0 & -1 \end{pmatrix} = \frac{1}{2}\sigma_z \quad (2.18)$$

with the well known Pauli matrices σ_k . These operators obey the commutation relations

$$[s_k, s_\ell] = i\epsilon_{k\ell m}s_m \quad (2.19)$$

and have thus the algebraic structure of angular momentum operators.

A general normalized pure spin state $|\psi\rangle = a|\uparrow\rangle + b|\downarrow\rangle = |a|e^{i\varphi_\uparrow}|\uparrow\rangle + |b|e^{i\varphi_\downarrow}|\downarrow\rangle$ can be written in the form

$$|\psi\rangle = e^{i\varphi/2} \cos(\theta/2) |\uparrow\rangle + e^{-i\varphi/2} \sin(\theta/2) |\downarrow\rangle \quad (2.20)$$

with $\varphi = \varphi_\uparrow - \varphi_\downarrow$ using that $|a|^2 + |b|^2 = 1$ and the freedom to drop the global phase $(\varphi_\uparrow + \varphi_\downarrow)/2$. The expectation value of the spin $\mathbf{s} = (s_x, s_y, s_z)^\top$ is then given by

$$\langle \mathbf{s} \rangle = \begin{pmatrix} \langle s_x \rangle \\ \langle s_y \rangle \\ \langle s_z \rangle \end{pmatrix} = \frac{1}{2} \begin{pmatrix} \sin \theta \cos \varphi \\ \sin \theta \sin \varphi \\ \cos \theta \end{pmatrix}, \quad (2.21)$$

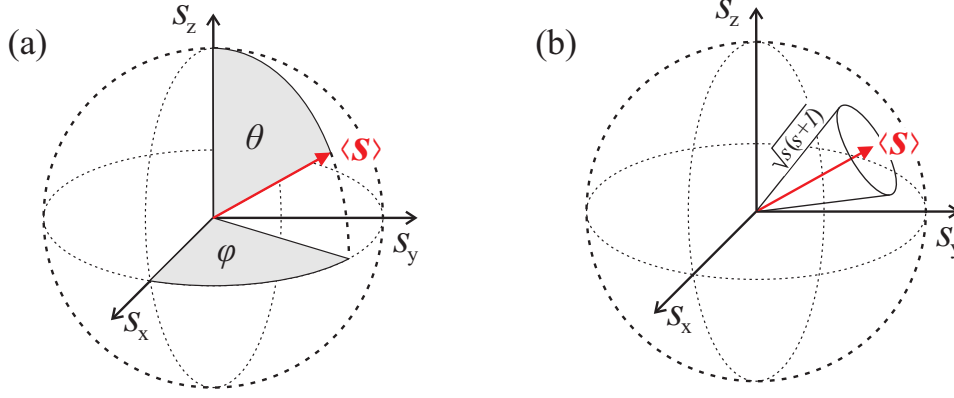


Figure 2.4.: **Pure state representation on the Bloch sphere.** (a) The expectation value of a single pseudo spin $\langle \mathbf{s} \rangle$ can be represented on a sphere with radius $s = 1/2$ according to Eq. (2.21). (b) Since the length of the spin $|\mathbf{s}| = \sqrt{s(s+1)}$ is larger than s , it has to have additional fluctuating components orthogonal to the mean vector. Thus, the spin is commonly depicted as a cone around the mean direction $\langle \mathbf{s} \rangle$.

i.e. $(s = \frac{1}{2}, \theta, \varphi)$ are spherical coordinates of $\langle \mathbf{s} \rangle$. The expectation value of the spin can thus be depicted on a sphere as shown in Fig. 2.4a. Quantum mechanically, the length of the spin is given by $|\mathbf{s}| = \sqrt{\mathbf{s}^2} = s(s+1) = 3/4$. The slightly larger length is due to the unavoidable quantum fluctuations of the spin orthogonal to its mean direction $\langle \mathbf{s} \rangle$.

As an example, let us choose the coordinate system (i.e. the basis $\{|\uparrow\rangle, |\downarrow\rangle\}$) such that the mean spin is pointing in x -direction $\langle \mathbf{s} \rangle = (1/2, 0, 0)^T$. Since this corresponds to an eigenstate of s_x , a measurement of s_x always yields $1/2$. All classical vectors with a length of $|\mathbf{s}| = \sqrt{s(s+1)}$ and a projection $s_x = 1/2$ are located on a cone as depicted in Fig. 2.4b. Quantum mechanically, it is not possible to represent the state by only one of these vectors, since measurements of the orthogonal spin components s_y and s_z have to show fluctuations

$$(\Delta s_y)^2 + (\Delta s_z)^2 = s_y^2 + s_z^2 = \mathbf{s}^2 - s_x^2 = 3/4 - 1/4 = 1/2. \quad (2.22)$$

In most textbooks, the quantum mechanical state is thus represented by the cone [56] rather than by a single vector. In this representation the mean spin is given by the length and the orientation of the cone, while the fluctuations are represented by the disc at the end. These unavoidable fluctuations are also reflected in the Heisenberg uncertainty relation

$$\Delta s_y \Delta s_z \geq \frac{1}{2} |\langle s_x \rangle| \quad (2.23)$$

which is a direct consequence of the non-vanishing commutator given in Eq. (2.19). In the next section we will see, that in the Bloch sphere representation, it becomes apparent that these fluctuations cause the shot noise discussed in section 2.2.1.

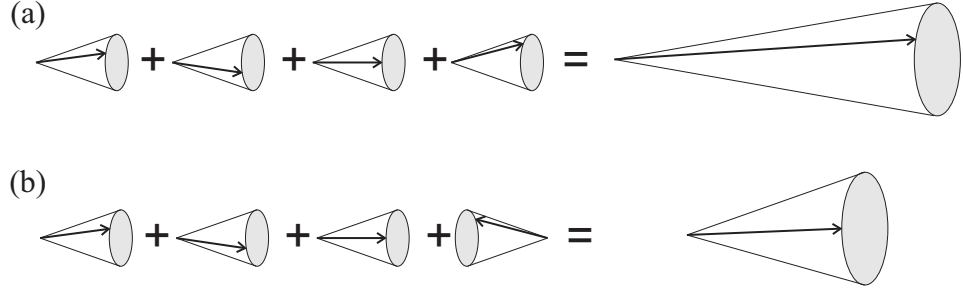


Figure 2.5.: **Formation of the collective spin.** (a) All particles are in the same pure state. Thus, the individual pseudo spins are polarized in the same direction. Such a pure symmetric state has the maximum collective spin length $J_{\max} = N/2$. (b) Distinguishable particles can have spin states that are not symmetric under particle exchange, which results in a reduced length of the collective spin as shown in this example.

2.3.2. The multi-particle Bloch sphere

For an ensemble of N particles a collective spin can be obtained by adding up the individual spins.

$$\mathbf{J} = \sum_{i=1}^N \mathbf{s}^{(i)}, \quad (2.24)$$

where $\mathbf{s}^{(i)}$ denotes the spin operator of the i th particle. Obviously, the collective operators again obey the commutation relations for angular momentum operators

$$[J_k, J_\ell] = i \epsilon_{k\ell m} J_m, \quad (2.25)$$

resulting in the uncertainty relations

$$\Delta J_k \Delta J_\ell \geq \frac{1}{2} |\langle J_m \rangle|. \quad (2.26)$$

It is straightforward to show that pure spin states which are symmetric with respect to particle exchange are spin $J_{\max} = N/2$ states (see Appendix A.1). A simple example of a not fully symmetric state with reduced spin length $J < N/2$ is shown in Fig. 2.5b. Here and in the following we approximate the spin length $|\mathbf{J}| = \sqrt{J(J+1)} \approx J$ which causes only small deviations in the case of large particle numbers considered in this work. In the symmetric case, the collective spin operators can be written in the form [57, 58].

$$J_x = \frac{1}{2}(a^\dagger b + b^\dagger a) \quad (2.27)$$

$$J_y = \frac{1}{2i}(a^\dagger b - b^\dagger a) \quad (2.28)$$

$$J_z = \frac{1}{2}(a^\dagger a - b^\dagger b), \quad (2.29)$$

where a and b are the bosonic annihilation operators for a spin up and a spin down particle respectively.

As a first important example for a symmetric state on this generalized Bloch sphere, let us consider a collection of particles, each being in the $s_x^{(i)}$ eigenstate with $\langle s_x^{(i)} \rangle = 1/2$. Hence, the expectation value of the collective spin of this so-called coherent spin state is pointing in x -direction $\langle J_x \rangle = \sum_i \langle s_x^{(i)} \rangle = N/2 = J$. Again, the total spin has to be depicted as a cone as shown in figure 2.5, since its length $|\mathbf{J}| = \sqrt{\mathbf{J}^2} = \sqrt{J(J+1)}$ is larger than its x -component. The fluctuations in the components J_y and J_z represented by the circle at the end of the cone originate from the fluctuations of the individual spins. The radius of this circle $\sqrt{\mathbf{J}^2 - \langle J_x^2 \rangle} = \sqrt{J} = \sqrt{N/2}$ is connected with shot-noise fluctuations in the following way: For uncorrelated particles we have $\Delta J_y = \Delta J_z$ and thus

$$(\Delta J_y)^2 + (\Delta J_z)^2 = J_y^2 + J_z^2 = (\mathbf{J})^2 - J_x^2 = J(J+1) - J^2 = J \quad (2.30)$$

$$\Rightarrow \Delta(N_\uparrow - N_\downarrow) = 2\Delta J_z = \sqrt{2J} = \sqrt{N} \quad (2.31)$$

Not only shot noise but also the Heisenberg limit is captured in the Bloch sphere representation as we will see now.

2.3.3. The Heisenberg uncertainty for phase and particle number difference

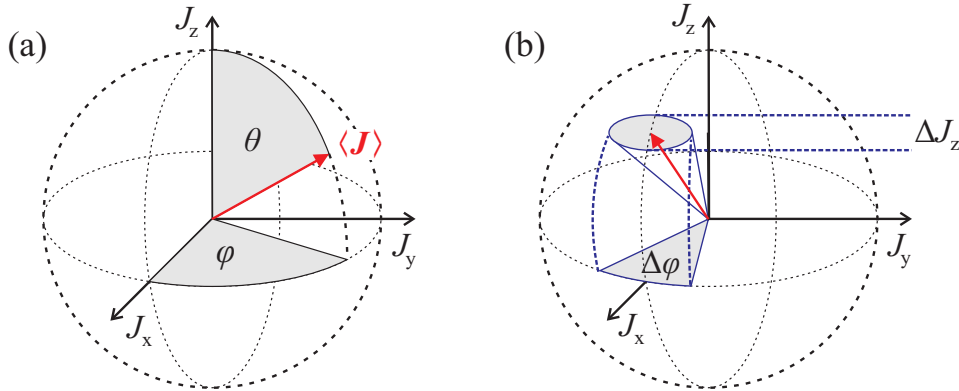


Figure 2.6.: **A multi-particle state on the generalized Bloch sphere.** (a) The expectation value of the collective spin $\langle \mathbf{J} \rangle$ can be depicted on a sphere with radius $J \leq N/2$. (b) The quantum fluctuations of collective spin states are depicted as an ellipse around its mean value. These unavoidable fluctuations are in close connection to fluctuations in the phase and number difference.

The Heisenberg uncertainty relation between phase and number difference that was used to derive the Heisenberg limit of phase sensitivity can be derived from the uncertainty relations of the collective spin operators (2.26). For this purpose, we define the

2. Entanglement and interferometry

angle θ and the phase difference $\varphi = \varphi_\uparrow - \varphi_\downarrow$ for an arbitrary spin state in analogy to Eq. (2.21).

$$\langle \mathbf{J} \rangle = \begin{pmatrix} \langle J_x \rangle \\ \langle J_y \rangle \\ \langle J_z \rangle \end{pmatrix} = r \begin{pmatrix} \sin \theta \cos \varphi \\ \sin \theta \sin \varphi \\ \cos \theta \end{pmatrix} \quad (2.32)$$

with $r = \sqrt{\langle \mathbf{J} \rangle^2} < |J|$ as shown in Fig. 2.6. Without loss of generality we can choose the coordinates such that $\langle J_y \rangle = 0$. Hence, we can write

$$\langle J_x \rangle = r \sin \theta \quad (2.33)$$

$$\Delta J_y \approx r \sin \theta \Delta(\varphi_\uparrow - \varphi_\downarrow) \quad (2.34)$$

Using this and that $J_z = \frac{1}{2}(N_\uparrow - N_\downarrow)$ by definition, we can get the desired number-phase uncertainty relation from the uncertainty relations (2.26).

$$\Delta J_y \Delta J_z \geq \frac{1}{2} |\langle J_x \rangle| \quad (2.35)$$

$$\Rightarrow r \sin \theta \Delta(\varphi_\uparrow - \varphi_\downarrow) \frac{1}{2} \Delta(N_\uparrow - N_\downarrow) \geq \frac{1}{2} r \sin \theta \quad (2.36)$$

$$\Leftrightarrow \Delta(\varphi_\uparrow - \varphi_\downarrow) \Delta(N_\uparrow - N_\downarrow) \geq 1, \quad (2.37)$$

For a high interferometric phase sensitivity it is beneficial to reduce the fluctuations ΔJ_z at the expense of ΔJ_y as we will see in section 2.4. In the picture used here, this corresponds to reduced fluctuations of the number difference at the expense of larger fluctuations of the phase difference. After the first beam splitter of the interferometer, the low fluctuations of the number difference are converted into low fluctuations of the phase difference. This enables a precise measurement of the phase shift ϕ between the two beam splitters of the interferometer.

2.3.4. The interferometer sequence in the Bloch sphere representation

Not only the spin states, but also typical state manipulation can be represented on the Bloch sphere. To understand the action of an interferometer sequence on a given input state, we need to know the effect of a beam splitter and a phase shift in the Bloch sphere representation.

A beam splitter transfers a particle in one of the two spin states to a superposition

$$|\uparrow\rangle \rightarrow \cos(\theta/2) |\uparrow\rangle - i \sin(\theta/2) |\downarrow\rangle \quad (2.38)$$

$$|\downarrow\rangle \rightarrow -i \sin(\theta/2) |\uparrow\rangle + \cos(\theta/2) |\downarrow\rangle \quad (2.39)$$

and in this basis the corresponding operator $R(\theta)$ can be written as

$$R_\theta = \begin{pmatrix} \cos(\theta/2) & -i \sin(\theta/2) \\ -i \sin(\theta/2) & \cos(\theta/2) \end{pmatrix}. \quad (2.40)$$

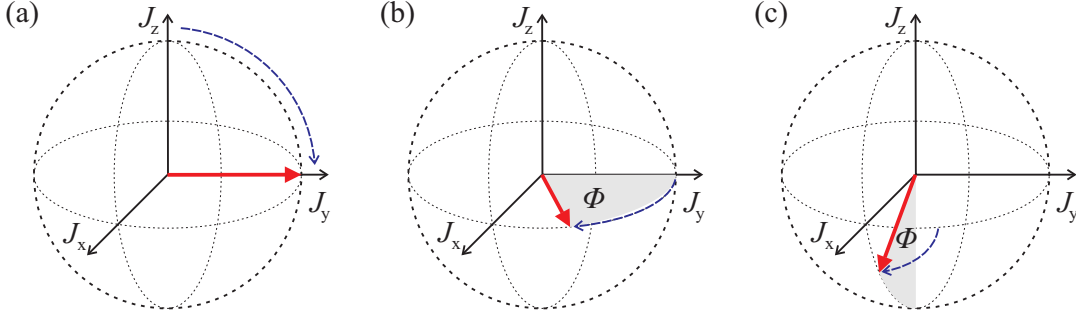


Figure 2.7.: **Interferometer sequence on the Bloch sphere.** (a) The first beam splitter rotates the collective spin by $\pi/2$ around the x -axis. (b) During an evolution time the state picks up a phase difference ϕ which corresponds to a rotation of the collective spin around the z -axis. (c) The second beam splitter is again a $\pi/2$ rotation about the x -axis. In total the collective spin experienced a rotation of ϕ around the y -axis.

The complex i is necessary to obtain a unitary operator $R_\theta^\dagger R_\theta = 1$ and a balanced 50:50 beam splitter is obtained for $\theta = \pi/2$. It is easy to see that this corresponds to a rotation of the single particle spin $\mathbf{s}^{(i)}$ around the x -axis $R_\theta = \exp(-i\theta s_x^{(i)})$ [57].

$$\mathbf{s}^{(i)} = \begin{pmatrix} s_x^{(i)} \\ s_y^{(i)} \\ s_z^{(i)} \end{pmatrix} \rightarrow \begin{pmatrix} 1 & 0 & 0 \\ 0 & \cos \theta & -\sin \theta \\ 0 & \sin \theta & \cos \theta \end{pmatrix} \begin{pmatrix} s_x^{(i)} \\ s_y^{(i)} \\ s_z^{(i)} \end{pmatrix} \quad (2.41)$$

For multiple particles, each spin is rotated in the same way $R_\theta^{\otimes N} = R_\theta \otimes R_\theta \otimes \dots \otimes R_\theta$. Since the collective spin is just the sum of the individual spins $R_\theta^{\otimes N} = \exp(-i\theta J_x)$.

$$\mathbf{J} = \begin{pmatrix} J_x \\ J_y \\ J_z \end{pmatrix} \rightarrow \begin{pmatrix} 1 & 0 & 0 \\ 0 & \cos \theta & -\sin \theta \\ 0 & \sin \theta & \cos \theta \end{pmatrix} \begin{pmatrix} J_x \\ J_y \\ J_z \end{pmatrix} \quad (2.42)$$

A relative phase shift φ of the two states is described up to a global phase by

$$|\uparrow\rangle \rightarrow e^{i\varphi/2} |\uparrow\rangle \quad (2.43)$$

$$|\downarrow\rangle \rightarrow e^{-i\varphi/2} |\downarrow\rangle \quad (2.44)$$

with the corresponding operator

$$R_\varphi = \begin{pmatrix} e^{i\varphi/2} & 0 \\ 0 & e^{-i\varphi/2} \end{pmatrix}. \quad (2.45)$$

It is easy to see that this corresponds to a rotation of the individual spins around the z -direction and for the collective spin we thus get

$$\mathbf{J} = \begin{pmatrix} J_x \\ J_y \\ J_z \end{pmatrix} \rightarrow \begin{pmatrix} \cos \varphi & -\sin \varphi & 0 \\ \sin \varphi & \cos \varphi & 0 \\ 0 & 0 & 1 \end{pmatrix} \begin{pmatrix} J_x \\ J_y \\ J_z \end{pmatrix}. \quad (2.46)$$

2. Entanglement and interferometry

We can hence represent the action of an interferometer sequence as depicted in Fig. 2.7. The action of the full interferometer sequence on the collective spin is obtained from a multiplication of the matrices $\exp(-i \frac{\pi}{2} J_x)$ for the beam splitters and the matrix for the phase shift $\exp(-i \theta J_z)$.

$$U = e^{-i \frac{\pi}{2} J_x} e^{-i \theta J_z} e^{-i \frac{\pi}{2} J_x} = \begin{pmatrix} \cos \phi & 0 & \sin \phi \\ 0 & -1 & 0 \\ \sin \phi & 0 & -\cos \phi \end{pmatrix} \quad (2.47)$$

This corresponds to a rotation around the y -axis by the phase shift ϕ and spatial inversions. The spatial inversions are of minor importance for the understanding the interferometer sequence and are often neglected. After the interferometer sequence we measure $\langle J_z \rangle_{\text{out}} = -\frac{N}{2} \cos \phi$ for an input state with a collective spin pointing z -direction $\langle J_z \rangle_{\text{in}} = \frac{N}{2}$. Hence, for a coherent spin state with an initial expectation value $\langle J_z \rangle = \frac{N}{2}$ the particle number difference given by $\langle J_z \rangle$ after the interferometer sequence can be used to estimate the phase as explained in section 2.2.1. However, other input states can be beneficial for the estimation precision as we will see now.

2.4. Spin squeezing and entanglement

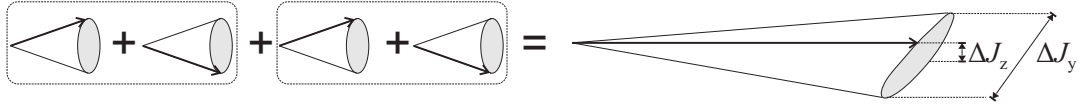


Figure 2.8.: **Collective spin of a spin-squeezed state.** In a spin-squeezed state, correlations between the individual spins lead to reduced fluctuations in the number difference ΔJ_z at the expense of increased fluctuations in ΔJ_y as schematically shown here [59]. The collective spin can hence be depicted as an elliptical cone [57].

As explained in section 2.2.2, entangled states can be used to improve the sensitivity of interferometers. Most commonly so-called spin-squeezed states are used for this purpose, which will be introduced in this section. In the limit of large particle numbers, spin squeezing turns out to imply quadrature squeezing, which is most commonly used in optics [60].

2.4.1. Interferometric gain and the spin-squeezing parameter

In a standard interferometer, the measured mean number of particles at the output port in terms of J_z is used to estimate the phase shift ϕ . From the Bloch sphere representation of the interferometer sequence presented in the last section we see that the expectation value of this output signal is

$$\langle J_z \rangle_{\text{out}} = \sin \phi \langle J_x \rangle \approx \phi \langle J_x \rangle \quad (2.48)$$

for an input state with $\langle J_y \rangle = \langle J_z \rangle = 0$. Error propagation thus leads to a phase estimation sensitivity of

$$\Delta\phi_{\text{est}} = \frac{\Delta J_z}{|\partial \langle J_z \rangle / \partial \phi|} = \frac{\Delta J_z}{\langle J_x \rangle}. \quad (2.49)$$

For a coherent state this leads to the shot-noise limit of sensitivity $\Delta\phi_{\text{est}} = 1/\sqrt{N}$. Hence, the so-called spin-squeezing parameter [61]

$$\xi = \sqrt{N} \frac{\Delta J_z}{\langle J_x \rangle} \quad (2.50)$$

identifies states with enhanced interferometric sensitivity $\Delta\phi_{\text{est}} = \xi/\sqrt{N} < 1/\sqrt{N}$, the so-called spin-squeezed states, by $\xi < 1$. These are the only useful entangled states for phase estimation by measuring the mean particle numbers at the output of an interferometer. However, other quantities can be used for phase estimation beyond shot noise using other classes of entangled states. A realization of such an unconventional quantum-enhanced interferometer will be presented in chapter 5.

2.4.2. The spin-squeezing parameter as an entanglement witness

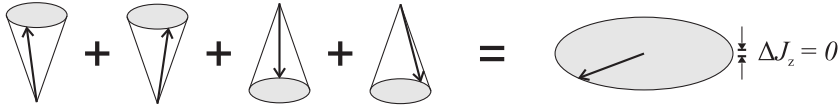


Figure 2.9.: **Separable state with sub-shot-noise number fluctuations.** An easy example of a separable, not fully symmetric state with vanishing fluctuations in ΔJ_z is depicted here: Two particles are prepared in a spin up state $|\uparrow\rangle$ and two in a spin down state $|\downarrow\rangle$. The spin length is largely reduced to $|J| = \sqrt{N}/2$. Such a state can only be prepared for distinguishable particles.

From the definition (2.50) it is easy to see that a necessary condition for spin-squeezing is sub-shot-noise fluctuations in the particle number difference of the state $\Delta J_z < \sqrt{N}/2$. The reduced uncertainty may stem from correlations between the individual spins due to entanglement as illustrated in Fig. 2.8. Indeed, for symmetric states, it is easy to show that sub-shot-noise fluctuations are sufficient to prove entanglement [62] (see appendix A.2). On the other hand, it is easy to find examples for separable, not fully symmetric states with sub-shot-noise fluctuations as shown in fig 2.9.

The other important quantity for spin squeezing is the length of its mean $\langle J_x \rangle$. For a reduced mean value $\langle J_x \rangle < \frac{N}{2}$ the amplitude of the signal at the output port of an interferometer decreases.

$$\langle J_z \rangle_{\text{out}} = \sin \phi \langle J_x \rangle \approx \phi \langle J_x \rangle \quad (2.51)$$

In other words, the mean spin in x -direction $\langle J_x \rangle$ gives the contrast of the interferometer. The maximum value $\langle J_x \rangle = N/2$ is only achievable for pure symmetric states. In this

2. Entanglement and interferometry

sense, the length of the mean spin $\langle J_x \rangle$ is also a measure of the symmetry of the state. It can be shown that all spin-squeezed states are entangled [63] (see appendix A.2), since they need to show both, sub-shot-noise fluctuations and a large mean spin.

Due to the Heisenberg uncertainty (2.26) this is only possible at the cost of increased fluctuations in ΔJ_y . Hence, the quantum fluctuations of a spin-squeezed state have to be depicted by an ellipse rather than a circle as shown in figure 2.8.

2.5. The phase sum and the total number of particles

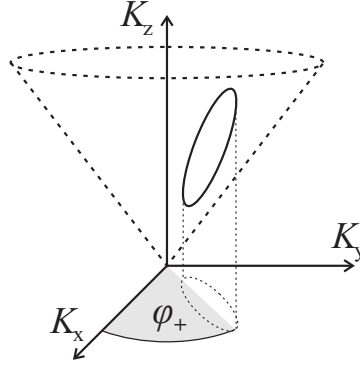


Figure 2.10.: **Representation of number and phase sum on a cone.** A state in the (K_x, K_y, K_z) space can be depicted on the surface of a cone [57]. The angle with respect to the x -axis gives the phase sum and the projection on the z -axis gives $\langle K_z \rangle = \frac{1}{2}(N + 1)$

If we have a third state $|0\rangle$ besides the two states $|\uparrow\rangle$ and $|\downarrow\rangle$, a general pure one-particle state can be written in the form

$$|\psi\rangle = |a|e^{i\varphi_\uparrow} |\uparrow\rangle + |b|e^{i\varphi_\downarrow} |\downarrow\rangle + |c|e^{i\varphi_0} |0\rangle. \quad (2.52)$$

This can be brought into the form

$$|\psi\rangle = \sqrt{1 - |c|^2} e^{i\varphi_+/2} (e^{i\varphi/2} \cos(\theta/2) |\uparrow\rangle + e^{-i\varphi/2} \cos(\theta/2) |\downarrow\rangle) + |c| |0\rangle \quad (2.53)$$

if we choose $\varphi_0 = 0$. Compared to the case with only two states in Eq. (2.20), here the phase sum $\varphi_+ = \varphi_\uparrow + \varphi_\downarrow$ is important since the third state provides a reference phase. Additionally, the probability for the particle to be found in the $\{|\uparrow\rangle, |\downarrow\rangle\}$ subspace given by $1 - |c|^2$ can vary.

In the case of symmetric many-particle states, both the phase sum and the number of particles in the $\{|\uparrow\rangle, |\downarrow\rangle\}$ subspace can be described by the Hermitian operators [57]

$$K_x = \frac{1}{2}(a^\dagger b^\dagger + ab) \quad (2.54)$$

$$K_y = \frac{1}{2i}(a^\dagger b^\dagger - ab) \quad (2.55)$$

$$K_z = \frac{1}{2}(a^\dagger a + b b^\dagger). \quad (2.56)$$

2.5. The phase sum and the total number of particles

As before, the operators a and b are the annihilation operators for a particle in the state $|\uparrow\rangle$ or $|\downarrow\rangle$, respectively. Obviously, the operator $K_z = \frac{1}{2}(a^\dagger a + b^\dagger b + 1)$ measures the total number of particles $N = N_\uparrow + N_\downarrow$. If we calculate the expectation value of the vector \mathbf{K} for a coherent state $a|\alpha\rangle = \alpha|\alpha\rangle$ in both spin states $|\psi\rangle = |\alpha\rangle \otimes |\beta\rangle$ with $\alpha = |\alpha|e^{i\varphi_\uparrow}$, $\beta = |\beta|e^{i\varphi_\downarrow}$

$$\langle \mathbf{K} \rangle = \begin{pmatrix} \langle K_x \rangle \\ \langle K_y \rangle \\ \langle K_z \rangle \end{pmatrix} = \begin{pmatrix} |\alpha||\beta| \cos(\varphi_+) \\ -|\alpha||\beta| \sin(\varphi_+) \\ \frac{1}{2}(|\alpha|^2 + |\beta|^2 + 1) \end{pmatrix} \quad (2.57)$$

we see that the x - and y - components of this vector are useful to define the phase sum φ_+ .

The commutation relations for the operators are

$$\begin{aligned} [K_x, K_y] &= -iK_z \\ [K_y, K_z] &= iK_x \\ [K_z, K_x] &= iK_y \end{aligned} \quad (2.58)$$

and they thus have Heisenberg uncertainties

$$\Delta K_k \Delta K_\ell \geq \frac{1}{2} |\langle K_m \rangle| \quad (2.59)$$

similar to the collective spin operators (see Eq. (2.1)). Hence, we can derive a Heisenberg uncertainty between number and phase sum

$$\Delta(\varphi_\uparrow + \varphi_\downarrow) \Delta(N_\uparrow + N_\downarrow) \geq 1 \quad (2.60)$$

in almost the same way as we derived the Heisenberg uncertainty relation between number and phase difference in section 2.3.3.

It can be shown that all operators K_k commute with J_z . Furthermore, the operators have to fulfil

$$K_z^2 - K_x^2 - K_y^2 = J_z(J_z + 1). \quad (2.61)$$

For $J_z = 0$ the vector \mathbf{K} has thus to be on the surface of a cone as depicted in Fig. 2.10.

In summary, this shows that the phase sum $\varphi_+ = \varphi_\uparrow + \varphi_\downarrow$ and the total number of particles $N = N_\uparrow + N_\downarrow$ are a pair of conjugate variables. An other pair of conjugate variables is the phase difference $\varphi = \varphi_\uparrow - \varphi_\downarrow$ and the number difference $2J_z = N_\uparrow - N_\downarrow$ as we have seen in section 2.3.3. We will see in section 3.5 that the process of spin dynamics dynamically squeezes the number difference $2J_z$ and the phase sum, while the total number of particles and the phase difference are anti-squeezed.

3. Spin dynamics

In the last chapter we have seen that symmetric many-body states with sub-shot-noise fluctuations are entangled and can be used to improve the interferometric phase sensitivity beyond the shot-noise limit. In our experiments we use spin dynamics in a ^{87}Rb Bose-Einstein condensate (BEC) to create such ensembles. In this chapter the theory of spin-changing collisions will be introduced and in the next chapter we will present the experimental sequence for the creation of the ^{87}Rb BEC.

3.1. Spin-changing collisions

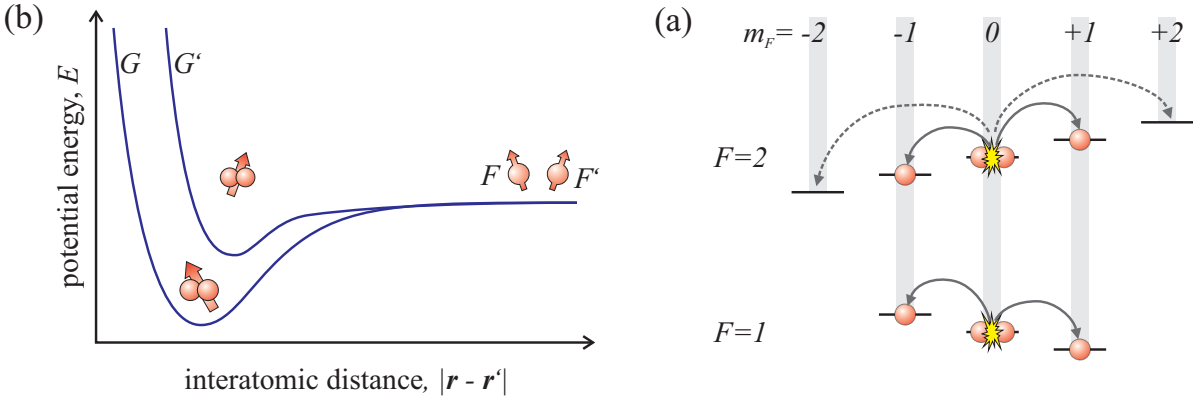


Figure 3.1.: **Origin of spin-changing collisions.** (a) At large interatomic distances $|\mathbf{r} - \mathbf{r}'|$, the internal state of ^{87}Rb atoms is well described by their hyperfine spins \mathbf{F} and \mathbf{F}' . During a collision at small interatomic distances $|\mathbf{r} - \mathbf{r}'|$, these hyperfine spins couple to a total spin $\mathbf{G} = \mathbf{F} + \mathbf{F}'$. The molecular potential depends on this total spin as well as the scattering lengths a_G . After a collision when the atoms are spatially well separated, their internal state can be described by two hyperfine spins $\tilde{\mathbf{F}}$ and $\tilde{\mathbf{F}}'$ again. These hyperfine spins might have changed compared to the initial hyperfine spins before the collision. If this is the case the collision is called a spin-changing collision. (b) ^{87}Rb atoms in the $m_F = 0$ level can collide and thereby be transferred to the $m_F = \pm 1$ Zeeman levels without changing the projection of the total spin $m_F + m_{F'}$. In $F = 2$, the spin-changing collisions from $m_F = 0$ to $m_F = \pm 2$ are also possible but much slower and can be neglected at short time scales.

3. Spin dynamics

The internal state of a ^{87}Rb atom at relatively low magnetic fields of several Gauss is best described by the hyperfine spin \mathbf{F} with length $\mathbf{F}^2 = F(F+1)$ and a projection on the magnetic field axis given by m_F . The hyperfine state of a ^{87}Rb atom $|F, m_F\rangle$ can be either in the $F = 2$ or the $F = 1$ manifold and the different projections $m_F = F, F-1, \dots, -F$ split up in several Zeeman levels in a magnetic field as shown in Fig. 3.1a. This description breaks down if two atoms approach each other during a collision. Interactions between the atoms lead to a coupling of the two hyperfine spins $|F, m_F\rangle$ and $|F', m'_F\rangle$. They form a total spin $\mathbf{G} = \mathbf{F} + \mathbf{F}'$ as depicted in Fig. 3.1b and their combined internal state is given by $|G, m_G\rangle$. After the collision the atoms fly apart and, eventually, their interaction becomes negligible. Thus, their internal states are again well described by the hyperfine spins \mathbf{F} . However, these quantities may have changed

$$|F, m_F\rangle |F', m'_F\rangle \rightarrow |\tilde{F}, \tilde{m}_F\rangle |\tilde{F}', \tilde{m}'_F\rangle. \quad (3.1)$$

Collisions involving a change of the hyperfine manifold $F = 2 \rightarrow \tilde{F} = 1$ release a large amount of energy and lead to a loss of atoms in the experiments. Such collisions will thus be treated together with other loss mechanisms. Here, we restrict our description to collisions within the same manifold $F = F' = \tilde{F} = \tilde{F}'$. At the ultra-low temperatures in the ^{87}Rb BEC only s -wave collisions are possible [64]. These collisions do not change the orbital angular momentum of an atom. For the conservation of the total angular momentum, the total spin projection $m_F + m'_F = \tilde{m}_F + \tilde{m}'_F$ has to be conserved by a spin-changing collision as well. Hence, if we start in the Zeeman levels $m_F = m'_F = 0$ only the collisions depicted in Fig. 3.1a are allowed.

In our experiments, we use these spin-changing collisions to transfer atoms from a ^{87}Rb condensate in $m_F = 0$ to the Zeeman levels $m_F = \pm 1$. As we will see in section 3.3, the coupling from $m_F = m'_F = 0$ to $\tilde{m}_F = -\tilde{m}'_F = \pm 2$ in the $F = 2$ manifold is more than two orders of magnitude smaller and can be neglected at the time scales of our experiments. This process has a strong analogy to parametric amplification in optics and produces entangled atoms in the output modes.

3.2. Analogy to parametric down conversion

The most commonly used tool in quantum optics for the creation of entangled photons is spontaneous parametric down conversion [65]. In this process, a strong pump beam with frequency ν_p enters a nonlinear crystal. The nonlinearity leads to the creation of the so-called signal and idler beams at frequencies ν_s and ν_i such that energy conservation $\nu_p = \nu_s + \nu_i$ is fulfilled. The signal and idler beams are highly entangled and can be used for Bell tests, quantum teleportation and many other applications in quantum information [65]. In the degenerate case $\nu_s = \nu_i = \nu_p/2$, the process can be used to create squeezed light [66], which has been successfully used to perform interferometry beyond the shot-noise limit [67].

Spin dynamics in cold atoms is analogous to optical parametric down conversion and thus offers exciting perspectives for the creation of non-classical entangled states of atoms. A condensate of ^{87}Rb atoms in the $m_F = 0$ state can be seen as the analogue of

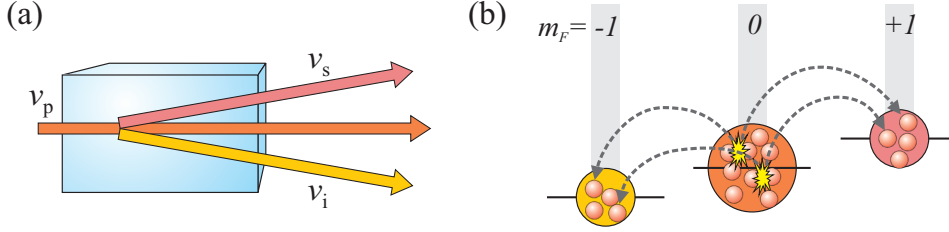


Figure 3.2.: **Analogy to parametric down conversion.** (a) The process of parametric down conversion is started by shining a strong pump beam at a frequency ν_p into a nonlinear crystal. The nonlinearity enables the conversion of photons from the pump beam into entangled photons in the so-called signal and idler beams with frequencies ν_s and ν_i . (b) Spin-changing collisions can be seen as an analogue in atom optics. The BEC in $m_F = 0$ acts as a strong pump. The nonlinear spin-changing collisions populate the modes $m_F = \pm 1$ which are the analogue to the signal and idler beams.

the pump beam in optics. The nonlinearity is intrinsic to the spin-changing collisions. The atoms that have been transferred to the $m_F = \pm 1$ levels are highly entangled and correspond to the photons in the signal and idler beam.

In the same way as in the optical case, the amplification of the output modes can be triggered by a classical seed or vacuum fluctuations [31]. While the vacuum fluctuations in optics correspond to fluctuations of the electromagnetic field, the vacuum fluctuations in the case of spin dynamics are the unavoidable fluctuations in the spin orientation discussed in section 2.3.3.

In the next section, we will see that spin-changing collisions can be described formally by the same Hamiltonian as parametric down conversion on short time scales.

3.3. Theoretical description

At cold temperatures, a collision can be described by the 2-particle interaction operator

$$\tilde{U} = \delta(\mathbf{r} - \mathbf{r}')g_G \quad \text{with} \quad g_G = \frac{4\pi a_G}{m} \quad (3.2)$$

for a given total spin G . Here, \mathbf{r} and \mathbf{r}' are the positions of the atoms and a_G is the scattering length. Since the molecular potential depends on the total spin G a different scattering length a_G can be measured for every possible value of G . The group of E.Tiemann at the Leibniz Universität Hannover yielding calculated these scattering lengths from a complex molecular potential analysis.

$$\begin{aligned} F = 1 & \quad a_0 = 101.6(2)a_B, \quad a_2 = 100.3(2)a_B \\ F = 2 & \quad a_0 = 87.9(2)a_B, \quad a_2 = 91.2(2)a_B, \quad a_4 = 99.0(2)a_B \end{aligned} \quad (3.3)$$

3. Spin dynamics

in units of the Bohr radius a_B . To express the operator for all possible collisions [68]

$$\tilde{U} = \delta(\mathbf{r} - \mathbf{r}')U \quad \text{with} \quad U = \sum_G g_G \sum_{m_G=-G}^G |G, m_G\rangle \langle G, m_G| \quad (3.4)$$

in terms of the atomic internal states $|F, m_F\rangle |F', m'_F\rangle$ we need to expand U by using the Clebsch-Gordan coefficients $\langle G, m_G | F, m_F\rangle |F', m'_F\rangle$. This enables us to calculate the matrix elements

$$U_{\tilde{m}_F, \tilde{m}'_F, m_F, m'_F} = \langle \tilde{F}, \tilde{m}_F | \langle \tilde{F}', \tilde{m}'_F | U | F, m_F\rangle | F', m'_F\rangle \quad (3.5)$$

describing the spin-changing collision of Eq. (3.1).

In the experiments, we start with all atoms in the $m_F = 0$ level. Since only a small fraction of atoms will be transferred to the $m_F = \pm 1$ levels at short time scales, we can neglect collisions that do not involve atoms in $m_F = 0$. Due to symmetry arguments, several of the remaining matrix elements have the same value and we end up with only three different terms [69]

- $U_0 = U_{0,0,0,0}$ describes the collision of two atoms in $m_F = 0$ without spin change.
- $U_1 = U_{\pm 1, \mp 1, 0, 0} = U_{0,0,\pm 1, \mp 1}$ describes the collision of two atoms in $m_F = 0$ undergoing a spin change to $m_F = \pm 1$ and the inverse process.
- $U_{10} = U_{\pm 1, 0, \pm 1, 0} = U_{\pm 1, 0, 0, \pm 1} = \dots$ describes the collision of one atom in $m_F = 0$ and the other one in $m_F = \pm 1$. This parameter can be shown to be $2U_{1,0} = U_0 + U_1$.

An evaluation of Eq.(3.5) yields

$$\begin{aligned} F = 1 \quad U_0 &= \frac{g_0 + 2g_2}{3} = 779.051 \frac{\text{Hz}}{10^{14} \text{ cm}^{-3}} \\ U_1 &= \frac{g_2 - g_0}{3} = -3.351 \frac{\text{Hz}}{10^{14} \text{ cm}^{-3}} \\ F = 2 \quad U_0 &= \frac{7g_0 + 10g_2 + 18g_4}{35} = 731.241 \frac{\text{Hz}}{10^{14} \text{ cm}^{-3}} \\ U_1 &= \frac{-7g_0 - 5g_2 + 12g_4}{35} = 25.787 \frac{\text{Hz}}{10^{14} \text{ cm}^{-3}} \end{aligned} \quad (3.6)$$

For typical densities in a BEC in the range of $n = 10^{14} \text{ cm}^{-3}$, this leads to time scales $t \sim \frac{1}{nU_1}$ of several tens of milliseconds for the spin-changing collisions. The matrix element $U_2 = U_{\pm 2, \mp 2, 0, 0} = U_{\pm 2, \mp 2, 0, 0}$ describing collisions of two atoms in $m_F = 0$ undergoing a spin change to $m_F = \pm 2$

$$U_2 = \frac{7g_0 - 10g_2 + 3g_4}{35} = 6.629 \cdot 10^{-2} \frac{\text{Hz}}{10^{14} \text{ cm}^{-3}} \quad (3.7)$$

is found to be more than two orders of magnitude smaller than U_1 . A population of the levels $m_F = \pm 2$ can thus be neglected at the relevant experimental time scales.

Let us now focus on the description of the spin-changing collisions, which transfer atoms from $m_F = 0$ to $m_F = \pm 1$. In second quantisation, the corresponding operator can be written in the form

$$H_1 = i2U_1 \left(C^* a_0^\dagger a_0^\dagger a_{+1} a_{-1} - C a_{+1}^\dagger a_{-1}^\dagger a_0 a_0 \right). \quad (3.8)$$

Here, the bosonic annihilation operators a_{m_F} remove one particle in the corresponding Zeeman level with the spatial wave function $\phi_{m_F}(\mathbf{r})$. C is the overlap integral of these spatial wave functions

$$C = i \int \phi_{+1}^*(\mathbf{r}) \phi_{-1}^*(\mathbf{r}) \phi_0(\mathbf{r}) \phi_0(\mathbf{r}) d\mathbf{r}. \quad (3.9)$$

This operator has the same form as the nonlinear part of the Hamiltonian for parametric down conversion [70], showing the strong analogy between these processes.

For a large initial condensate, we can make use of the parametric approximation $a_0 \approx \sqrt{N_0}$ yielding

$$H_1 \approx i \left(\Omega^* a_{+1} a_{-1} - \Omega a_{+1}^\dagger a_{-1}^\dagger \right) \quad \text{with} \quad \Omega = 2CN_0 U_1. \quad (3.10)$$

If this was the only part in the Hamiltonian, the corresponding time evolution operator would be the two-mode squeezing operator [70]

$$U(t) = e^{-itH_1} = e^{t\Omega^* ab - t\Omega a^\dagger b^\dagger} = S(\xi) \quad (3.11)$$

with $\xi = t\Omega$, $a = a_{+1}$ and $b = a_{-1}$.

In the next section, we will add the missing part for the full Hamiltonian. We will see that there is a resonance condition that has to be fulfilled for an efficient transfer of atoms to the $m_F = \pm 1$ levels.

3.4. Spin dynamics resonances

In the last section, we focused on the part H_1 of the Hamilton operator describing the spin-changing collisions. To obtain the full Hamiltonian for the $m_F = \pm 1$ states, we have to consider the single particle Hamiltonian for these states in the absence of interactions. This can be split into one part for the external degrees of freedom and one for the internal degrees of freedom in the absence of spin-orbit coupling.

First, we have the operator H_{eff} for the external degrees of freedom, which can be written as

$$H_{\text{eff}} = -\frac{\hbar^2}{2m} \Delta + V_{\text{eff}}(\mathbf{r}), \quad (3.12)$$

in first quantization. It accounts for the kinetic and potential energy of an $m_F = \pm 1$ atom in an effective potential. The effective potential

$$V_{\text{eff}}(\mathbf{r}) = V_{\text{ext}}(\mathbf{r}) + (U_0 + U_1)n_0(\mathbf{r}) - \mu \quad (3.13)$$

3. Spin dynamics

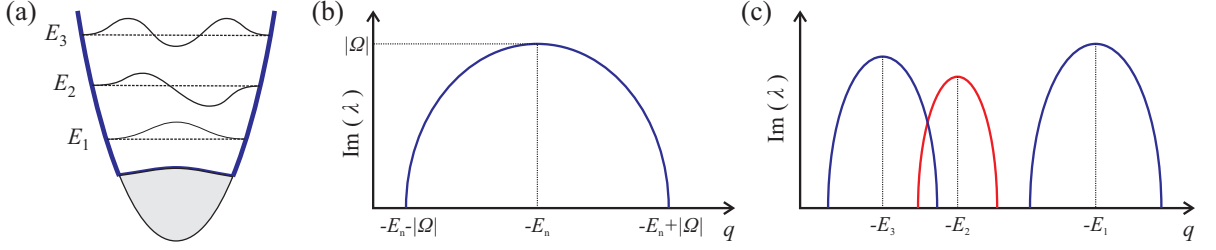


Figure 3.3.: **Effective potential and instability rates.** (a) The effective potential (blue line) for atoms in $m_F = \pm 1$ is a sum of the external confining potential (black parabola) and the repulsive mean-field interaction with the condensate in $m_F = 0$ (grey area). It supports several eigenenergies E_n (dashed horizontal lines) and corresponding eigenstates (black lines). (b) The instability rate $\text{Im}(\lambda)$ reaches its maximal value $|\Omega|$ if the change in the internal energy q cancels the change in external energy E_n . As a function of q , the instability rate is a half circle with radius $|\Omega|$ centred at E_n . (c) When all eigenstates of the effective potential are taken into account, the instability rate as a function of q shows a multi-resonant structure.

is the sum of the external confining potential $V_{\text{ext}}(\mathbf{r})$ and the mean field interaction with the condensate in $m_F = 0$, which has a particle density $n_0(\mathbf{r})$. The chemical potential μ is subtracted to set the zero energy point to the energy of an atom in the $m_F = 0$ condensate. A typical effective potential is sketched in Fig. 3.3a.

We parametrize the internal energy by the parameter $2q$, which denotes the excess internal energy that two atoms in the states $m_F = +1$ and $m_F = -1$ have compared to two atoms in the $m_F = 0$ state. This energy difference can be manipulated as we shall see in sections 4.2 and 5.3.

To express the Hamiltonian in second quantization, we choose the bosonic annihilation operators $a_{\pm 1}$ such that they correspond to particles in an eigenstate of the effective potential with energy E_n . We assume that atoms in $m_F = +1$ and $m_F = -1$ have the same spatial wave function. This approximation is justified by the fact that the integral (3.9) typically becomes very small if this is not the case. With this we arrive at

$$H = (E_n + q)(a_{+1}^\dagger a_{+1} + a_{-1}^\dagger a_{-1}) + i \left(\Omega^* a_{+1} a_{-1} - \Omega a_{+1}^\dagger a_{-1}^\dagger \right), \quad (3.14)$$

where we used Eq. (3.10) for the interaction part H_1 of the Hamiltonian.

Now, we can use the Hamiltonian to calculate the transfer of atoms from the $m_F = 0$ condensate to the $m_F = \pm 1$ states. Therefore, we use the time evolution of the bosonic operators in the Heisenberg picture.

$$i \frac{d}{dt} a_{+1} = [H, a_{+1}] = -(E_n + q)a_{+1} + i\Omega a_{-1}^\dagger \quad (3.15)$$

$$i \frac{d}{dt} a_{-1}^\dagger = [H, a_{-1}^\dagger] = (E_n + q)a_{-1}^\dagger + i\Omega^* a_{+1} \quad (3.16)$$

with $\hbar = 1$. This can be rewritten as

$$i \frac{d}{dt} \begin{pmatrix} x \\ y \end{pmatrix} = \begin{pmatrix} -E_n - q & i\Omega \\ i\Omega^* & E_n + q \end{pmatrix} \begin{pmatrix} x \\ y \end{pmatrix} \quad (3.17)$$

where a vector $(x, y)^\top$ corresponds to an operator $xa_{+1} + ya_{-1}^\dagger$ and for $(x, y)^\top = (1, 0)^\top$ and $(x, y)^\top = (0, 1)^\top$ we regain the above equations. If we find an eigenvector $(x_\lambda, y_\lambda)^\top$ with eigenvalue λ of the above matrix, we have a corresponding operator b with a simple time evolution

$$b(t) = x_\lambda a_{+1}(t) + y_\lambda a_{-1}^\dagger(t) = e^{-it\lambda} b(0). \quad (3.18)$$

which can be used to express the time evolution of the operators a_{+1} and a_{-1}^\dagger . The described technique is the so-called Bogolubov transformation [71]. To find the eigenvalues λ we have to solve the equation

$$(-E_n - q - \lambda)(E_n + q - \lambda) + |\Omega|^2 = 0, \quad (3.19)$$

yielding

$$\lambda = \pm \sqrt{(E_n + q)^2 - |\Omega|^2}. \quad (3.20)$$

These eigenvalues can be purely imaginary for

$$(E_n + q)^2 - |\Omega|^2 < 0 \quad (3.21)$$

leading to an exponential time dependence for the operators b_\pm corresponding to the eigenvectors

$$b_\pm(t) = e^{\mp it\lambda} b_\pm(0) = e^{\pm t \text{Im}(\lambda)} b_\pm(0). \quad (3.22)$$

Then, for sufficiently long times $t \gg \text{Im}(\lambda)$ and $\text{Im}(\lambda) > 0$ we can approximate $b_-(t) \approx 0$ and get

$$\langle N_{+1}(t) \rangle = \langle a_{+1}^\dagger(t) a_{+1}(t) \rangle \sim \langle b_+^\dagger(t) b_+(t) \rangle = e^{t^2 \text{Im} \lambda} \langle b_+^\dagger(0) b_+(0) \rangle \quad (3.23)$$

In this resonant regime, we thus expect an exponential growth of the population of atoms in the $m_F = \pm 1$ states.

Note that the positive imaginary part of Eq. (3.20) describes a half circle as a function of q centred at $-E_n$ as shown in Fig. 3.3b. Both, the width of the resonant regime and the maximum exponential growth rate $\text{Im}(\lambda)$ is thus given by $|\Omega|$. This can be seen as a consequence of the time-energy uncertainty principle. For the resonant case $E_n + q = 0$, the spin change conserves the energy, since the change in external energy E_n cancels with the change in internal energy q . If the time scale of the collision, given by $\sim \frac{1}{|\Omega|}$, is sufficiently short, energy conservation can be violated by at most $\pm |\Omega|$.

By tuning q we can reach the resonant case $q = -E_n$. In this case $H = H_1$ and the time evolution will be the two-mode squeezing operator as shown in Eq. (3.11). If q is not exactly tuned to resonance but has a detuning of $\delta = E_n + q$, we can split off the time evolution of the first part of the Hamiltonian (3.14) by changing to the interaction picture.

$$H(t) = i \left(\Omega^* a_{+1} a_{-1} e^{-i2\delta t} - \Omega a_{+1}^\dagger a_{-1}^\dagger e^{i2\delta t} \right) \quad (3.24)$$

3. Spin dynamics

Hence, the complex squeezing parameter $\xi \propto \Omega e^{i2\delta t}$ changes its angle in the complex plane with time. Since $S(-\xi) = S^{-1}(\xi)$ after a half-turn in the complex plane at $t = \frac{\pi}{2\delta}$ the squeezing counteracts the squeezing that has been achieved at the beginning of the time evolution. This leads to an oscillation of the population in the $m_F = \pm 1$ states as observed in Ref. [72]. For a large detuning $\delta \gg |\Omega|$ the amplitude of this oscillation becomes negligible and the system becomes stable in $m_F = 0$.

So far, we neglected all but one eigenmode of the effective potential, but obviously all of these eigenmodes can be populated by spin dynamics for the right tuning of q . The full Hamiltonian is thus a sum

$$H = \sum_n H^{(n)} \quad (3.25)$$

of Hamiltonians of the form (3.14) with the energies E_n of the corresponding eigenmodes and bosonic operators $a_{+1}^{\dagger(n)}$ and $a_{-1}^{\dagger(n)}$ creating particles in these eigenmodes. This leads to a rich resonance structure as depicted in Fig. 3.3c which depends on the form of the effective potential [30, 73]. In the regions of q where different resonances overlap, particles can be created in superpositions of eigenmodes of the effective potential. In section 5.3 and 6.2 we will see how we can experimentally tune the energy of the internal state to change q and thereby measure such a resonance structure.

3.5. Properties of the two-mode squeezed vacuum

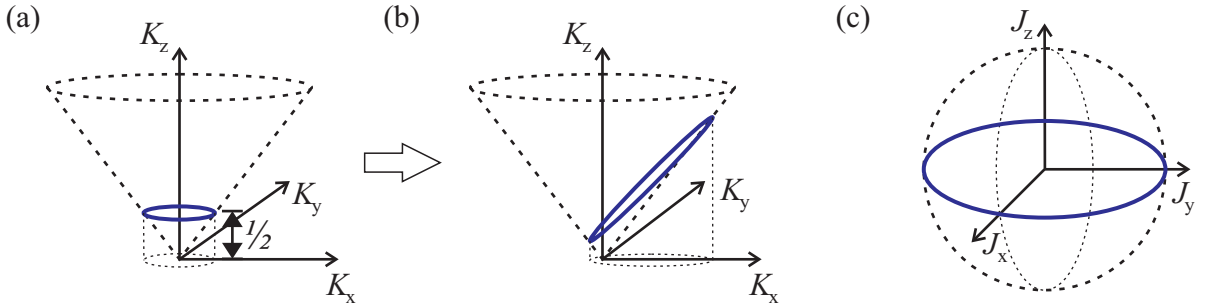


Figure 3.4.: **Representations of the two-mode squeezed vacuum.** (a) Representation of the vacuum state on the cone introduced in section 2.5 following Ref. [57]. This state evolves to the two-mode squeezed vacuum state shown in (b). The projection on the z -axis reflects its increased fluctuations in the total number of atoms and its orientation along the x -axis its well defined phase sum $\varphi_+ = \varphi_{\uparrow} + \varphi_{\downarrow}$. The two-mode squeezed vacuum is a superposition of twin-Fock states $|N_{\uparrow}, N_{\downarrow}\rangle$ with different total number of atoms $N = N_{\uparrow} + N_{\downarrow}$. These twin-Fock states can be represented as a ring around the equator of the generalized Bloch sphere (c). The vanishing width in z -direction reflects the states well defined number difference $2J_z = N_{\uparrow} - N_{\downarrow} = 0$. The collective spin can point in any direction in x - y -plane due to the completely undefined phase difference of the state.

3.5. Properties of the two-mode squeezed vacuum

In the last section, we saw that the operator for time evolution with spin dynamics tuned to a resonance is just the two-mode squeezing operator $S(\xi)$. Here, we choose the levels $m_F = \pm 1$ as spin up and down states of a pseudo spin- $\frac{1}{2}$ system and we can rename $a_{+1} = a$ and $a_{-1} = b$ to be consistent with the equations derived in chapter 2. Hence, if we start with no atoms in the $m_F = \pm 1$ levels we have a vacuum state in both levels $|N_\uparrow, N_\downarrow\rangle = |0, 0\rangle$ and after time evolution we get

$$|\psi(t)\rangle = S(\xi) |0, 0\rangle \quad \text{with} \quad \xi = \Omega t \quad (3.26)$$

the so-called two-mode squeezed vacuum. Here, we will summarize some of the properties of this highly entangled output state of resonant spin dynamics.

First, let us calculate the mean number $\langle N_+ + N_- \rangle = \langle a^\dagger a + b^\dagger b \rangle$ of atoms that are transferred to the $m_F = \pm 1$ levels. As detailed in the previous section we can find the time evolution of the bosonic operator $a(t)$ by diagonalizing Eq.(3.17) in the resonant case $E_n + q = 0$ yielding

$$b_+(t) = \frac{1}{2}(a(t) + b^\dagger(t)) = e^{|\Omega|t} b_+(0) \quad (3.27)$$

$$b_-(t) = \frac{1}{2}(a(t) - b^\dagger(t)) = e^{-|\Omega|t} b_-(0). \quad (3.28)$$

This can be solved for $a(t)$.

$$a(t) = b_+(t) + b_-(t) = \cosh(|\Omega|t)a + \sinh(|\Omega|t)b^\dagger \quad (3.29)$$

The time evolution of the number operator is thus

$$\begin{aligned} N_\uparrow(t) &= a^\dagger(t)a(t) \\ &= \cosh^2(|\Omega|t)a^\dagger a + \cosh(|\Omega|t)\sinh(|\Omega|t)[a^\dagger b^\dagger + ab] \\ &\quad + \sinh^2(|\Omega|t)bb^\dagger \end{aligned} \quad (3.30)$$

where we omitted to write the time dependence $A(t=0) = A$ for operators at $t=0$. If we start with the vacuum state, we have $\langle a^\dagger a \rangle = \langle b^\dagger b \rangle = \langle a^\dagger b^\dagger \rangle = \langle ab \rangle = 0$ and hence

$$\langle N_\uparrow(t) \rangle = \sinh^2(|\Omega|t) \quad (3.31)$$

Since the atoms are produced pairwise in the levels $m_F = \pm 1$ we get $\langle N_\uparrow(t) \rangle = \langle N_\downarrow(t) \rangle$.

It is instructive to use a second method to calculate this result for the mean number of atoms $\langle N_\uparrow(t) + N_\downarrow(t) \rangle$ by using the vector operator \mathbf{K} introduced in section 2.5. If we assume for simplicity that $\Omega = \Omega^*$ is real, then $H = 2\Omega K_y$ and the time evolution of the \mathbf{K} operator is

$$i \frac{d}{dt} \mathbf{K} = 2\Omega [K_y, \mathbf{K}] \quad (3.32)$$

Using the commutation relations for the components of \mathbf{K} from Eq. (2.58) one can find (see Appendix C and [57])

$$\mathbf{K}(t) = \begin{pmatrix} K_x(t) \\ K_y(t) \\ K_z(t) \end{pmatrix} = \begin{pmatrix} \cosh(2\Omega t) & 0 & \sinh(2\Omega t) \\ 0 & 1 & 0 \\ \sinh(2\Omega t) & 0 & \cosh(2\Omega t) \end{pmatrix} \begin{pmatrix} K_x \\ K_y \\ K_z \end{pmatrix} \quad (3.33)$$

3. Spin dynamics

If we start with the vacuum state, we have

$$\langle \mathbf{K}(t=0) \rangle = \frac{1}{2} \begin{pmatrix} 0 \\ 0 \\ 1 \end{pmatrix} \rightarrow \langle \mathbf{K}(t) \rangle = \frac{1}{2} \begin{pmatrix} \sinh(2\Omega t) \\ 0 \\ \cosh(2\Omega t) \end{pmatrix} \quad (3.34)$$

as depicted in Fig. 3.4a. By definition $K_z = \frac{1}{2}(N_\uparrow + N_\downarrow + 1)$ and hence,

$$\langle N(t) \rangle = \langle N_\uparrow(t) + N_\downarrow(t) \rangle = 2 \langle K_z \rangle - 1 = \cosh(2\Omega t) - 1 = 2 \sinh^2(\Omega t), \quad (3.35)$$

and we recover the exponential growth found in Eq. (3.31).

Not only the mean number of atoms but also its variance increases exponentially with time [70]

$$(\Delta N)^2 = \sinh^2(2|\Omega|t). \quad (3.36)$$

In the meanwhile, the fluctuations in K_y stay on the same level as depicted in figure 3.4b since $i \frac{d}{dt} K_y^2 = 2\Omega [K_y, K_y^2] = 0$. This means that the fluctuations of the phase sum $\varphi_+ = \varphi_\uparrow + \varphi_\downarrow$ are exponentially reduced.

$$(\Delta \varphi_+)^2 \approx \frac{(\Delta K_y)^2}{\langle K_z^2 \rangle} = \frac{1}{\langle (N+1)^2 \rangle} \approx \frac{1}{\langle N^2 \rangle} = \frac{1}{4 \sinh^2(|\Omega|t)} \quad (3.37)$$

In total, we have low fluctuations of the phase sum, which come at the expense of high fluctuations of the number of atoms, since these quantities are connected by the Heisenberg uncertainty of Eq. (2.60).

The other two quantities that are connected by a Heisenberg uncertainty given by Eq. (2.1) are the number difference $N_\uparrow - N_\downarrow = 2J_z$ and the phase difference $\varphi = \varphi_\uparrow - \varphi_\downarrow$. Initially, we have $\langle J_z \rangle = \Delta J_z = 0$ for the vacuum state. Since the Hamiltonian commutes with J_z , this does not change during the time evolution. Intuitively, as the atoms in $m_F = \pm 1$ have been transferred pairwise, the number of atoms in both states is always equal without any fluctuations. Hence, we can write the two mode squeezed vacuum state as a superposition of twin-Fock states $|N_\uparrow, N_\downarrow\rangle = |n, n\rangle$ having the same number of particles n in the up and down state yielding [70]

$$S(\Omega t) |0, 0\rangle = \frac{1}{\cosh(|\Omega|t)} \sum_{n=0}^{\infty} (-1)^n e^{in\theta} \tanh(|\Omega|t)^n |n, n\rangle \quad \text{with} \quad \Omega = |\Omega|e^{i\theta} \quad (3.38)$$

The well defined atom number difference $N_\uparrow - N_\downarrow = 0$ leads to a completely undefined phase difference. Projecting on a given total number of atoms N reduces the two-mode squeezed vacuum to a twin-Fock state that can be represented by a ring around the equator of a generalized Bloch sphere of radius $\mathbf{J}^2 = \frac{N}{2}(\frac{N}{2} + 1)$ as shown in Fig. 3.4c.

The properties of such a twin-Fock state will be further investigated in chapter 5, where we will demonstrate its usefulness for interferometry, and in chapter 6, where we will focus on the characterization of its entanglement.

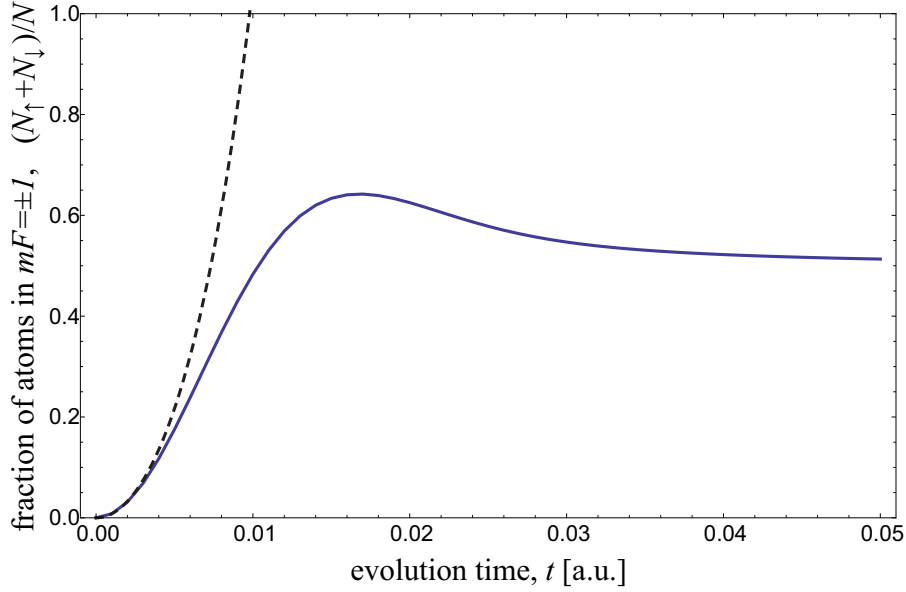


Figure 3.5.: **Exact time dependence of spin dynamics for a total of 1 000 atoms.**

The blue line is the fraction of atoms in the $m_F = \pm 1$ levels versus time calculated by the method from Ref. [68]. At short times it shows the exponential growth predicted using the parametric approximation (dashed line). For longer times however, it saturates on the level where $N_0 = N_\uparrow + N_\downarrow$.

3.6. Beyond the parametric approximation

In section 3.3, we made a couple of approximations that are only true for short time scales. For instance, there might be a non-negligible transfer to the states $m_F = \pm 2$ in $F = 2$ at longer evolution times. In both cases $F = 1$ and $F = 2$, the interaction of $m_F = \pm 1$ atoms with each other can no longer be neglected after a significant number of atoms has been transferred. Most importantly, we neglected the depletion of the condensate in $m_F = 0$ by approximating $a \approx \sqrt{N_0}$ to obtain Eq. (3.10).

Law, Pu and Bigelow pointed out that an exact solution in $F = 1$ can be gained if we assume that atoms in all the different Zeeman levels have the same spatial mode [68], but their method can be easily extended to different spatial modes. The basic idea is to expand the full interaction Hamiltonian including all possible spin-changing collisions in terms of the states $|N_\uparrow, N_0, N_\downarrow\rangle = |k, N - k, k\rangle$. These states form a basis for a sub-space of the full Hilbert space containing all states with a fixed total number of particles N and a projection of the collective spin $J_z = \frac{1}{2}(N_\uparrow - N_\downarrow) = 0$. Since the Hamiltonian commutes with both, N and J_z , the time evolution is restricted to this sub-space if we start in the state $|N_\uparrow, N_0, N_\downarrow\rangle = |0, N, 0\rangle$. It is hence sufficient to express and diagonalize the Hamiltonian in this sub-space to calculate the full time evolution which considerably speeds up the calculations and enables exact solutions for up to a few thousand atoms.

An example for such an exact calculation is given in Fig. 3.5 assuming perfect overlap of all involved spatial wave functions. Starting from the state $|N_\uparrow, N_0, N_\downarrow\rangle = |0, N, 0\rangle$ the

3. Spin dynamics

system stabilizes at $N_{\uparrow} + N_{\downarrow} = N_0$. This shows, that we expect the initially exponential growth to slow down and finally stop due to the depletion of the $m_F = 0$ condensate.

One flaw of this method is that the wave functions of the atoms in the different Zeeman levels are assumed to be constant in time. However, as the populations of the internal levels change, the interactions between the atoms will also change. For instance, the reduced density in the $m_F = 0$ condensate will change the shape of the effective potential seen by the atoms in $m_F = \pm 1$. Nonetheless, the predicted transfer rate agrees qualitatively with our measurements [30].

4. Preparation, manipulation and detection of a ^{87}Rb spinor condensate

In this chapter, the techniques for the observation of entangled states created by spin dynamics are described. These techniques provide the basis for the demonstration of interferometric sensitivity beyond the classical limit presented in chapter 5 and the proof of multi-particle entanglement described in chapter 6.

4.1. Preparation of the initial ^{87}Rb condensate

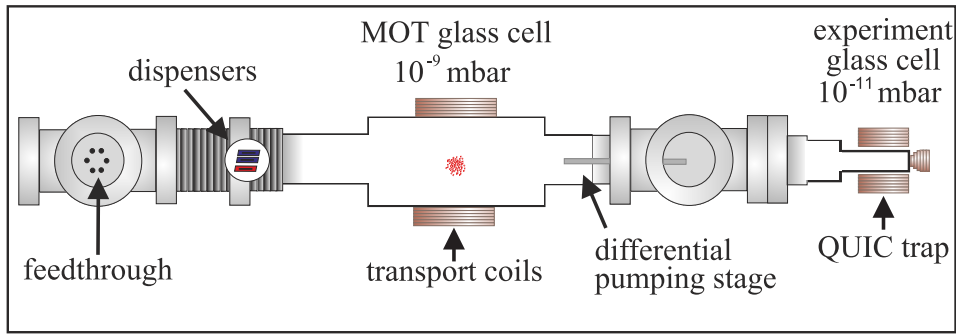


Figure 4.1.: **Experiment setup** [74]. In a glass cell at a pressure of 10^{-9} mbar, a MOT is loaded from the background gas. In the magnetic trap created by moveable transport coils, the atoms can be transferred into a QUIC trap in a second glass cell at a lower pressure of 10^{-11} mbar. After radio-frequency evaporation, the atoms are transferred into a crossed-beam dipole trap in the center of the cell.

As explained in chapter 3, the starting point for our experiments on spin dynamics is a BEC in the Zeeman level $m_F = 0$. The preparation of the BEC will be briefly presented here. For a more detailed description of the apparatus and the experimental sequence, please refer to the publications [75, 76] and the phd and diploma theses [69, 74, 77–80].

We start with a magneto-optical trap (MOT) of 10^9 ^{87}Rb atoms in a glass cell directly loaded from atoms in the background gas. As an atom source, we use dispensers which are heated up by applying a current of 4.3 A for 45 minutes every other week. Most of the atoms are deposited on the glass surface. To temporarily increase the number of

4. Preparation, manipulation and detection of a ^{87}Rb spinor condensate

^{87}Rb background atoms for efficient loading of the MOT, we shine ultraviolet (UV) light on the cell to desorb the atoms [75]. After 10 s of MOT loading, the UV light is switched off again, allowing for a lower pressure which is beneficial for the following steps.

After a short time of molasses cooling, we optically pump the atoms into the $|F, m_F\rangle = |2, 2\rangle$ level and trap them in a magnetic quadrupole field provided by two coils in anti-Helmholtz configuration. These coils are mounted on a translation stage allowing us to move the atoms within 1.3 s from the MOT glass cell into the experiment glass cell. The two glass cells are connected by a small tube, the so-called differential pumping stage, keeping up a pressure difference of two orders of magnitude. The ultra-high vacuum of 10^{-11} mbar in the experiment cell provides minimal losses and heating of the atomic ensemble from collisions with the background gas.

By ramping down the current in the transport coils and ramping up the currents of coils in the quadrupole-Ioffe configuration (QUIC) the atoms are transferred into a harmonic magnetic trap [81]. In this trap, the atoms are cooled close to quantum degeneracy by radio-frequency evaporation [82]. By adjusting the currents in the QUIC trap coils and the transport coils the atoms can be moved to the center of the glass cell [76]. Here, two horizontal laser beams at a wavelength of 1064 nm with waists of $50\text{ }\mu\text{m}$ and $30\text{ }\mu\text{m}$ and maximum powers of 700 mW and 200 mW, respectively, form a crossed-beam dipole trap [83]. The atoms are transferred into this dipole trap by ramping down the magnetic fields and ramping up the power in the beams of the dipole trap. Subsequently, the laser power is reduced to 35 mW and 15 mW within 0.6 s leading to further evaporative cooling [84] of the ensemble. Finally, the dipole trap power is increased again to reach the final desired trap frequencies in the range of 50 – 200 Hz.

In total, we can produce a BEC of 30 000 atoms with a negligible thermal fraction with these techniques. The techniques for the preparation of the internal state will be detailed in the following sections.

4.2. Manipulation of the energy levels via microwave dressing

The internal energy levels of a ^{87}Rb atom split up in a magnetic field as presented in Fig. 3.1. These levels can be manipulated by tuning the magnetic field, which will be discussed in detail in section 5.3, and by introducing a coupling between a Zeeman level $|e\rangle$ in the $F = 2$ manifold and a Zeeman level $|g\rangle$ in the $F = 1$ manifold. This coupling can be achieved by applying a microwave at a frequency ω close to the energy difference of the two levels $\omega_0 = E_e - E_g$. This so-called microwave dressing is used in many experiments with ultra-cold atoms [32, 85–87].

4.2. Manipulation of the energy levels via microwave dressing

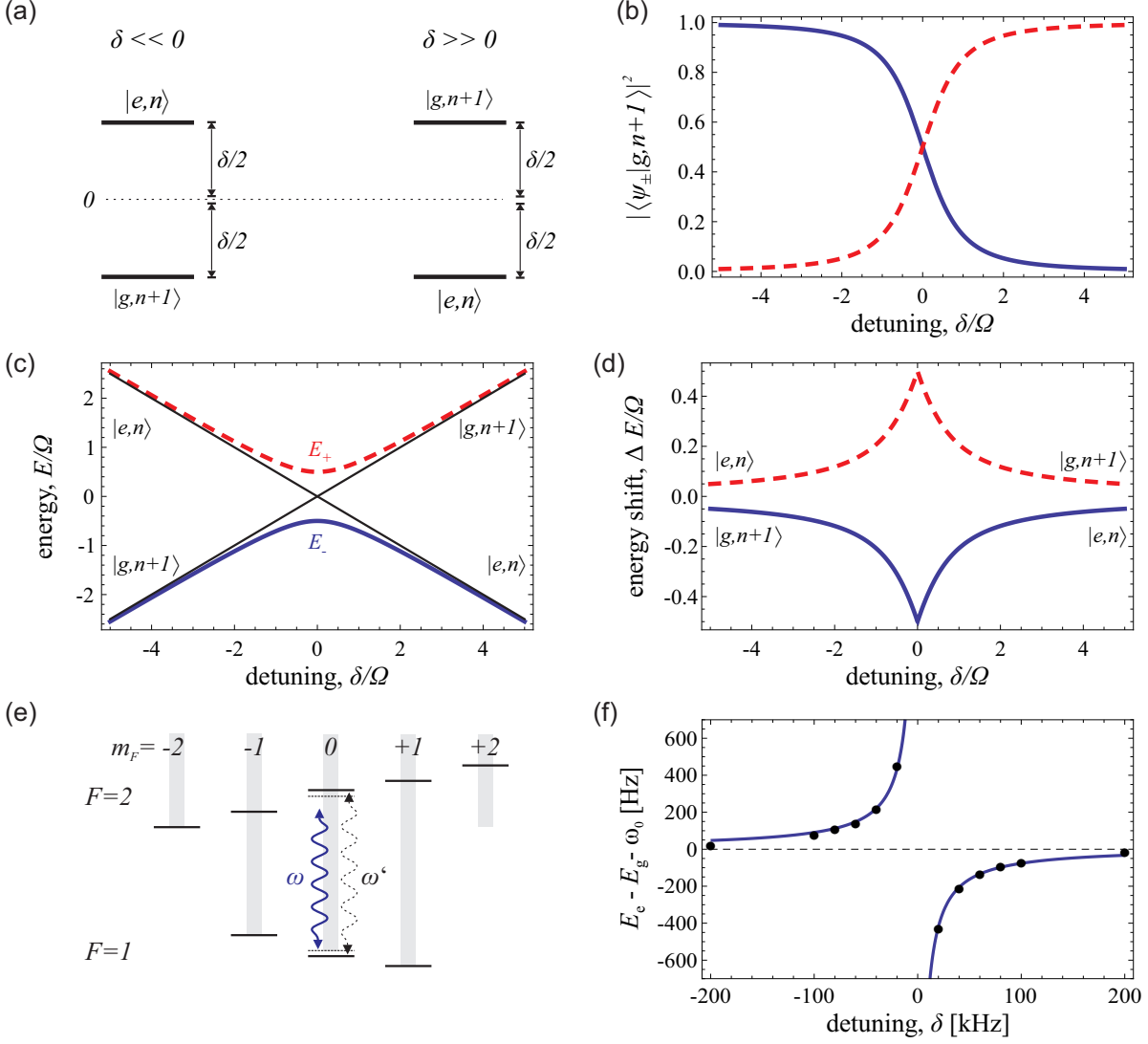


Figure 4.2.: **Manipulation of the internal state by microwave dressing.** (a) The bare states $|g, n+1\rangle$ and $|e, n\rangle$ have an energy difference of δ in the absence of coupling. (b) The dressed states $|\psi_{\pm}\rangle$ are the eigenstates of the Hamiltonian in the presence of microwave coupling and can be written as a superposition of the bare states. At $\delta = 0$ the dressed states $|\psi_{\pm}\rangle$ are in an even and odd superposition of the bare states, respectively. (c) The energy of the bare states is degenerate for $\delta = 0$ in the absence of coupling. The dressed states have an energy difference of Ω at this point, since the microwave coupling leads to an avoided crossing. (d) The difference of the energy of the bare states and the dressed states gives the energy shift of the internal levels of the atom. (e) As an experimental demonstration we dress the levels $F = 1, m_F = 0$ and $F = 2, m_F = 0$ with a strong microwave at a frequency ω and use a weak microwave at the frequency ω' to measure the shift of the energy difference $E_e - E_g$ with respect to the unperturbed energy difference given by ω_0 . (f) Such a measurement (black points) is in good agreement with the predicted shift (blue line).

4. Preparation, manipulation and detection of a ^{87}Rb spinor condensate

If there is no coupling between the atom and the microwave, the so called bare states $|g, n\rangle$ and $|e, n\rangle$ are the eigenstates of the system, where n is the number of microwave photons. If this microwave frequency is exactly matched $\omega = \omega_0$, the bare state $|\psi_g\rangle = |g, n+1\rangle$ has the same energy as the state $|\psi_e\rangle = |e, n\rangle$. If the microwave is detuned by $\delta = \omega - \omega_0$, they have an energy difference of δ . We choose the zero energy to be in between these levels such that the states have an energy of $\pm\delta/2$ as shown in Fig. 4.2a.

In the basis of these bare states, we can write the Hamiltonian of the effective two-level atom in the microwave field as [70]

$$H = \frac{1}{2} \begin{pmatrix} \delta & \Omega \\ \Omega & \delta \end{pmatrix} \quad (4.1)$$

where the resonant coupling $\Omega \propto \sqrt{n} \propto \sqrt{P}$ depends on the microwave power P . Due to this coupling the bare states are no longer energy eigenstates. The new eigenstates of the Hamiltonian are the so called dressed states

$$|\psi_+\rangle = \sin(\phi/2) |g, n+1\rangle + \cos(\phi/2) |e, n\rangle \quad (4.2)$$

$$|\psi_-\rangle = \cos(\phi/2) |g, n+1\rangle - \sin(\phi/2) |e, n\rangle \quad (4.3)$$

where $\phi = \tan^{-1} \left(\frac{\Omega}{\delta} \right)$. The corresponding energies are

$$E_{\pm} = \pm \frac{1}{2} \sqrt{\delta^2 + \Omega^2}. \quad (4.4)$$

The degeneracy of the bare states at $\delta = 0$ for no coupling $\Omega = 0$ is lifted and the energy difference of the dressed states at this point is Ω as shown in Fig. 4.2c. We are interested in the shift of the energy levels ΔE_g and ΔE_e of the atom shown in Fig. 4.2c. To obtain this shift, we subtract the energy of the corresponding bare states $\pm\delta/2$ to obtain

$$\Delta E_g = +\delta \frac{1}{2} \left(\sqrt{1 + \frac{\Omega^2}{\delta^2}} - 1 \right) \quad (4.5)$$

$$\Delta E_e = -\delta \frac{1}{2} \left(\sqrt{1 + \frac{\Omega^2}{\delta^2}} - 1 \right). \quad (4.6)$$

Note, that these energy shifts change sign as the detuning δ changes sign. For microwave frequencies ω smaller than the transition frequency ω_0 the detuning is negative $\delta < 0$ and the energy difference $E_e - E_g$ is increased by the microwave dressing, whereas for $\delta > 0$ the energy difference is reduced by the microwave dressing.

In the experiment, the dressing microwave is generated by the setup shown in the upper part of Fig. 4.3 starting with a signal generator (Marconi 2024), which is locked to a 10 MHz frequency reference of an ultrastable maser. The output frequency of about 2.275 GHz is then tripled by a frequency multiplier (mini circuits ZX90-3-812-S+) to the desired frequency of ~ 6.83 GHz in the range of the hyperfine splitting of ^{87}Rb . The power can be adjusted by a DC current applied to a frequency mixer (mini

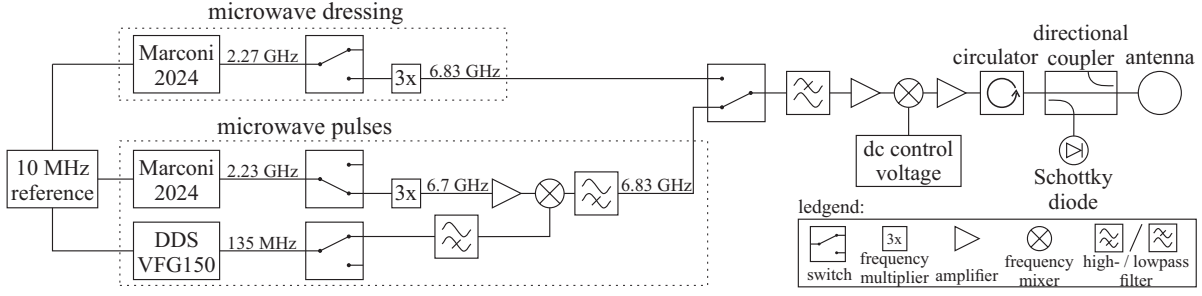


Figure 4.3.: **Microwave generation.** As a microwave source for the dressing of the internal states, we triple the frequency of a signal generator (Marconi 2024), which is locked to a 10 MHz reference. For the generation of microwave pulses, we start with the same procedure of tripling the frequency of a signal generator and subsequently mix the signal with ~ 135 MHz generated by a DDS. We use filters to select the side-band with the sum-frequency only from the mixed signal. Either of the two microwaves for dressing and pulses can be sent to a sequence of amplifiers by setting a microwave switch. Finally, a maximum power of 10 W is sent to a loop antenna close to the atoms.

circuits ZMX-8GLH) which is necessary for adiabatically ramping up and down the microwave power. These ramps make sure that the system stays in an eigenstate of the Hamiltonian [88, 89]. Subsequently, the microwave is amplified to a power of up to 7 W, which can be monitored by a Schottky diode (Herotek DHM124AA) after a 20 dB directional coupler (UMCC DC-E000-20s). Finally, this microwave is sent to an antenna placed at a distance of about 3 cm from the atomic cloud. We fabricate the antenna by bending the core of a coaxial cable (aircell5) to a single loop with a circumference of one wavelength.

With this microwave source at hand, we can manipulate the internal level structure according to Eq. (4.5). One way to verify the shift of the hyperfine energy levels is to probe the energy difference $E_e - E_g$ by shining in a second microwave at a frequency ω' . If this additional microwave is operated only at low power, the energy shift that it induces can be neglected. Nonetheless, it will transfer atoms to the excited state when it is tuned close to resonance $\omega' \approx E_e - E_g$ and can thereby be used to measure the energy difference as shown in Fig. 4.2f. The measured energy shift is in agreement with Eq. (4.5). A small systematic deviation can be explained by the influence of neighbouring levels. To account for the corresponding additional transitions, the presented two-level model can be extended to multiple levels.

4.3. Manipulation of the internal states via microwave pulses

The microwave can also be used to transfer atoms from one internal state to another as we will see now.

4. Preparation, manipulation and detection of a ^{87}Rb spinor condensate

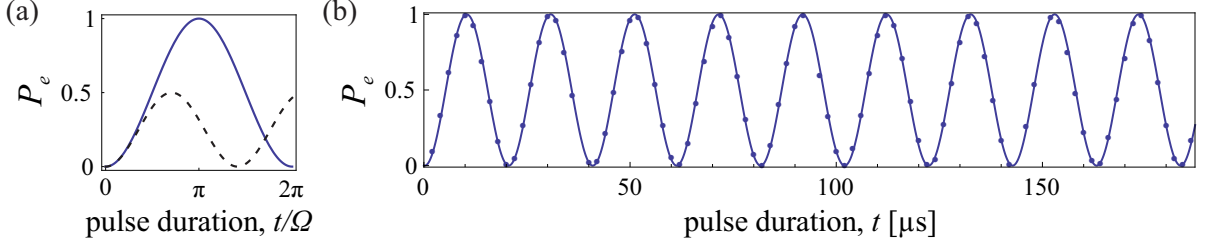


Figure 4.4.: **Rabi oscillation.** (a) Probability P_e to find the atom in the excited state $|e\rangle$ as a function of the pulse length t for $\delta = 0$ (solid blue line) and $\delta = \Omega$ (dashed black line) according to Eq. (4.12). (b) Experimentally observed Rabi oscillation between the hyperfine levels $|F, m_F\rangle = |2, 2\rangle$ and $|1, 1\rangle$.

From Eq. (4.2), we can express the bare states $|\psi_g\rangle = |g, n+1\rangle$ and $|\psi_e\rangle = |e, n\rangle$ in terms of the dressed states and thus easily calculate their time dependence.

$$\begin{aligned} |\psi_g(t)\rangle &= \sin(\phi/2) |\psi_+(t)\rangle + \cos(\phi/2) |\psi_-(t)\rangle \\ &= \sin(\phi/2) e^{-it\Omega/2} |\psi_+\rangle + \cos(\phi/2) e^{+it\Omega/2} |\psi_-\rangle \end{aligned} \quad (4.7)$$

$$\begin{aligned} |\psi_e(t)\rangle &= \cos(\phi/2) |\psi_+(t)\rangle - \sin(\phi/2) |\psi_-(t)\rangle \\ &= \cos(\phi/2) e^{-it\Omega/2} |\psi_+\rangle - \sin(\phi/2) e^{+it\Omega/2} |\psi_-\rangle \end{aligned} \quad (4.8)$$

For the resonant case $\delta = 0$, we have $\cos(\phi/2) = \sin(\phi/2) = \frac{1}{\sqrt{2}}$ and the above equation reduces to

$$|\psi_g(t)\rangle = \cos(t\Omega/2) |\psi_g\rangle - i \sin(t\Omega/2) |\psi_e\rangle \quad (4.9)$$

$$|\psi_e(t)\rangle = -i \sin(t\Omega/2) |\psi_g\rangle + \cos(t\Omega/2) |\psi_e\rangle. \quad (4.10)$$

If we define $|\psi_g\rangle = |\downarrow\rangle$ and $|\psi_e\rangle = |\uparrow\rangle$ as our pseudo-spin basis, this equation has exactly the form of the beam splitting process of Eq. (2.38) with $\theta = t\Omega$. Hence, a resonant microwave pulse can be used as a beam splitter.

If we shine a resonant microwave pulse for a time t on an atom in the ground state $|\psi_g\rangle$, the probability P_e to find it in the excited state $|\psi_e\rangle$ after the pulse is thus

$$P_e = |\langle\psi_e|\psi_g(t)\rangle|^2 = \sin^2(t\Omega/2) = \frac{1}{2}(1 - \cos(t\Omega)). \quad (4.11)$$

These so-called Rabi oscillations can be observed in the experiment as presented in Fig. 4.4. Hence, a pulse of length $t_\pi = \frac{\pi}{\Omega}$ transfers the atom to the excited state $|\psi_e\rangle$. Such π -pulses can be used for the preparation of the internal state.

For a non-zero detuning δ , this probability changes to

$$P_e = \frac{\Omega^2}{\Omega_R^2} \sin^2(t\Omega_R/2) \quad \text{with} \quad \Omega_R = \sqrt{\Omega^2 + \delta^2} \quad (4.12)$$

and a perfect transfer cannot be achieved (see Fig. 4.4a).

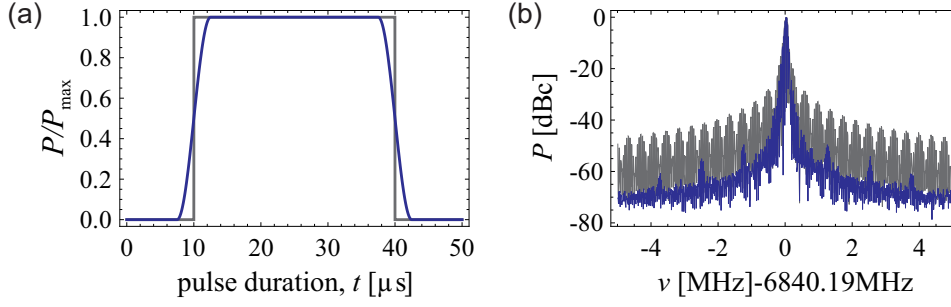


Figure 4.5.: **Microwave pulse in the time and frequency domain.** (a) Instead of using a rectangular pulse (grey line) we use sinusoidal ramps $\sin^2(t)$ for the pulse edges. (b) In the frequency domain this results in a narrower distribution. The spectral components for the rectangular pulse (grey line) and the pulse with sinusoidal edges (blue line) have been measured with a spectrum analyser (Advantest R3267) by continuously repeating the pulses. Peaks at multiples of approximately ± 1.3 MHz from the carrier are due to residual frequencies of the DDS (Toptica VFG150).

The setup of our microwave source for pulse generation is shown in the lower part of Fig. 4.3. Similarly to the source for microwave dressing described in the previous section, the frequency of a signal generator (Marconi 2024) at 2.235 GHz is tripled (mini circuits ZW90-3-812-S+) in a first step to obtain 6.705 GHz. This microwave is mixed (mini circuits ZMX-7GR) with a ~ 135 MHz signal provided by a direct digital synthesiser (DDS, Toptica VFG 150) and filtered to suppress the carrier by more than 30 dB and the lower side band by more than 10 dB. Finally, this signal can be sent to the same amplifiers and the same antenna as the dressing microwave by setting a switch (mini circuits ZYSWA-2-50DR).

Compared to the dressing microwave, the spectral purity of the signal is worse due to the DDS. For the long microwave irradiation times needed for the microwave dressing residual unwanted frequency components may be close to an atomic transition frequency and transfer a fraction of the atomic ensemble to the corresponding Zeeman level of the hyperfine structure. However, the DDS allows for a fast switching of frequencies enabling us to prepare an internal state by a series of pulses within a fraction of a millisecond. Additionally, we can shape the form of the pulses by quickly adjusting the output power of the DDS. This reduces the spectral width of the pulse [90] (see Fig. 4.5b), which can become large for shorter pulses leading to unwanted transitions. Moreover, smooth pulse shapes make the transition less vulnerable to frequency jitter due to an increased width of the central peak in the frequency domain. We use pulses with $5 \mu\text{s}$ long sinusoidal shaped edges as shown in Fig. 4.5a.

With microwave pulses, we can drive transitions of the internal states as shown in Fig. 4.4b. Fluctuations in the number of transferred atoms are caused by many technical effects:

- Fluctuations of the microwave power P

4. Preparation, manipulation and detection of a ^{87}Rb spinor condensate

- Fluctuations of the microwave polarization
- Fluctuations of the magnetic field
- Fluctuations of the microwave frequency ω
- Fluctuations of collisional shifts due to density fluctuations
- Fluctuations due to light-induced energy shifts

Fundamentally, the number of transferred atoms has to be subject to shot noise for an unentangled atomic ensemble. We estimate changes in the microwave frequency to be on the order of a few Hertz, a negligible effect compared to other noise sources. The first three effects are dominant and their effect can be calculated by a simple Monte-Carlo simulation. The results can be compared to measurements [91] to estimate the strength of the different contributions. It is difficult to distinguish changes in the polarization from power fluctuations since both result in deviations of the resonant Rabi frequency Ω . Such fluctuations can also be caused by mechanical vibrations of the antenna or objects that reflect the microwave back on the atoms. Both of these effects are estimated to lead to fluctuations below 0.2% in the number of transferred atoms for a $\frac{\pi}{2}$ microwave pulse.

The magnetic field stability is of particular importance for the reduction of fluctuations in the microwave transitions. We measure a standard deviation as low as $77(4) \mu\text{G}$ at a magnetic field of a few Gauss using a Ramsey sequence [92, 93]. These low fluctuations were achieved by actively stabilizing the magnetic field in a single direction. It is created by a pair of Helmholtz coils and measured with a flux gate sensor (Bartington Mag03) close to the atoms. For the stabilization, a feed-back loop adjusts the current through the coils which is provided by a car battery to avoid fluctuations caused by a 50 Hz power supply. A large fraction of the remaining changes in the magnetic field is actually caused by the 50 Hz power supplies of the surrounding electronics in the room. This can be further suppressed by operating the experiment synchronised to this frequency. Therefore, a phase locked loop delivers a synchronized 100 kHz frequency providing the time basis of the experimental control. This means that all experimental steps occur at a fixed phase of the 50 Hz supply frequency. Experimental steps which are highly sensitive to timing jitters like the length of the microwave pulses are controlled by the time basis of the DDS, which is stabilized to the ultra-stable maser.

4.4. High precision absorption detection

One of the most critical requirements to observe sub-shot-noise fluctuations is the precise counting of the atoms in the two pseudo spin states. For 10^4 atoms in the entangled states the shot noise is 100 atoms or 1% of the total number of atoms. Hence, we need an atom detection that enables us to count the number of atoms in individual states to a precision much better than 100 atoms. With the high precision absorption detection presented in this section we are able to estimate the number of atoms in a single state with a precision of 14 atoms.

4.4.1. Techniques for atom detection

Before we have a detailed look at high precision absorption detection, let us discuss the requirements we have on the atom detection system and compare some of the available techniques.

For optical detection schemes, the average number of detected photons n_{ph} per atom is of central importance. If we detect on average $n_{\text{ph}} = 100$ photons scattered by a single atom, this number will fluctuate with a standard deviation of at least $\Delta n_{\text{ph}} = \sqrt{n_{\text{ph}}} = 10$ photons due to the photon shot noise. However, since the fluctuations are an order of magnitude smaller than the mean number of photons, the detection of a single atom is feasible and has been demonstrated in a couple of experiments [94–96]. For $N = 10^4$ atoms, however, the situation is different, since it is usually not possible to assign the detected photons to the individual atoms. Hence, we detect a total number of photons of $N_{\text{ph}} = N \cdot n_{\text{ph}} = 10^6$ with a standard deviation of $\Delta N_{\text{ph}} = \sqrt{N n_{\text{ph}}} = 10^3$. To get the corresponding uncertainty in the estimated number of atoms ΔN_{est} , we have to divide by the number of photons per atom n_{ph} yielding

$$\Delta N_{\text{est}} = \frac{\sqrt{N n_{\text{ph}}}}{n_{\text{ph}}} = \sqrt{\frac{N}{n_{\text{ph}}}} = 10. \quad (4.13)$$

From this equation, it is clear, that it becomes increasingly difficult to realize a detection system with single-atom precision $\Delta N_{\text{est}} \leq 1$ for large ensembles, since this requires at least a detection of $n_{\text{ph}} = N$ scattered photons per atom.

From the above discussion we see that for an optical detection technique we need to collect as many scattered photons as possible. The most commonly used methods are absorption and fluorescence detection. Absorption detection relies on the measurement of the reduced intensity in a light beam due to photons that are scattered, whereas fluorescence detection directly counts the scattered photons. Absorption detection has the advantage that ideally all scattered photons are detectable as a loss in the intensity of the imaging beam, while fluorescence detection only collects a fraction of these photons due to a limited solid angle covered by the imaging optics. On the other hand, longer illumination times are possible for fluorescence detection leading to an increased number of photons. Both techniques have been used to image up to 10^3 atoms achieving a standard deviation of 2.6 atoms [97] in the case of absorption imaging and 8(3) atoms [87] for fluorescence imaging.

The illumination time in fluorescence imaging can be extended by trapping the atoms in a MOT. In reference [98], single-atom resolution at a total number of $N = 1080$ atoms in a MOT was demonstrated with an illumination time of 100 ms. However, this technique is not suitable for counting atoms in two different states produced in a single experimental run. Since this is crucial for observing sub-shot-noise fluctuations, it would be necessary to extend this very promising concept and trap atoms state selectively in different MOTs.

A completely different concept of atom detection is to ionize the atoms with an electron beam and detect the atoms with a channeltron as demonstrated in Refs. [99, 100].

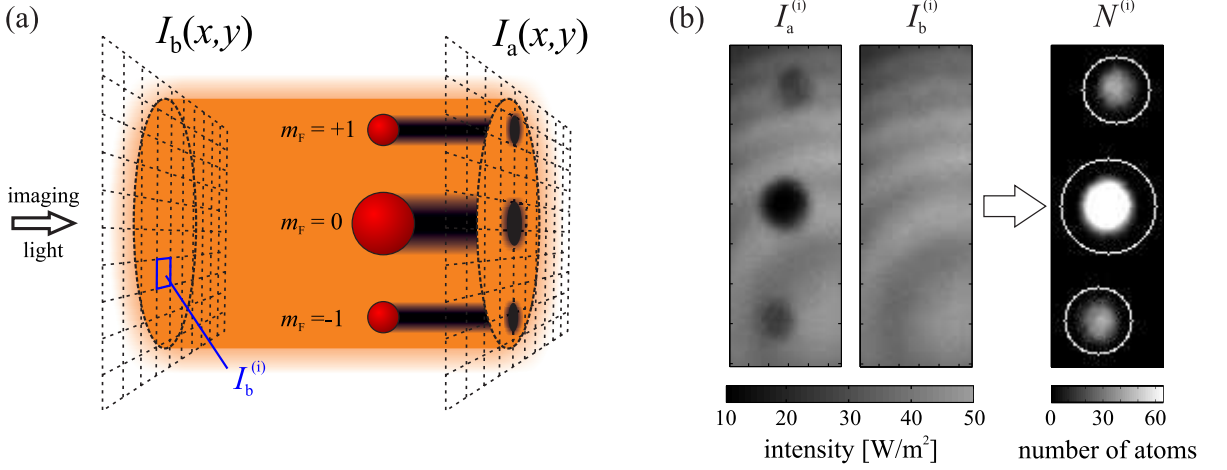


Figure 4.6.: **Absorption imaging.** (a) The schematic illustration shows the basic principle of absorption imaging. The intensity $I_b(x,y)$ of an incoming resonant laser beam is recorded on a CCD camera yielding measurements $I_b^{(i)}$ on the individual pixels. In the presence of atoms, light is scattered and the reduced intensity $I_a(x,y)$ can be measured giving $I_a^{(i)}$. The different Zeeman components were separated by an inhomogeneous magnetic field. (b) Typical absorption images. The recorded intensities $I_a^{(i)}$ and $I_b^{(i)}$ can be used to estimate a number of atoms $N^{(i)}$ corresponding to each pixel. The white circles around the clouds indicate the areas containing the relevant pixels for the summation $N_{\text{est}} = \sum_i N^{(i)}$. For the estimation of the number of atoms in the levels $m_f = \pm 1$ these areas have a diameter of 33 pixels.

However, the single atom detection efficiency of about 15% leads to a large uncertainty of $\Delta N_{\text{est}} = \sqrt{0.15(1 - 0.15)N}/0.15$ on the order of 75 atoms for a total number of 1000 atoms due to shot-noise.

In summary, optical detection schemes are to date the most promising methods for a precise measurement of the number of atoms and the best results for several 100 atoms have been achieved by absorption imaging [97].

4.4.2. Calculating the number of atoms from an absorption signal

The principle of absorption detection is schematically shown in Fig. 4.6a. A resonant light beam passes through an atomic ensemble and scattering leads to a reduction of the light intensity. The intensity $I_a(x,y)$ in the plane of the atoms is imaged on a CCD camera. Each pixel on the camera measures the mean intensity $I_a^{(i)}$ of the corresponding square region in the object plane. As a reference for the unperturbed intensities of the laser beam $I_b^{(i)}$, a second measurement in the absence of atoms is performed. Our goal is to estimate the number of atoms $N^{(i)}$ in the region corresponding to pixel number (i) from a comparison of the measured intensities $I_a^{(i)}$ and $I_b^{(i)}$.

The scattering rate γ of a single atom leading to a reduced intensity $I_a(x,y)$ compared

to $I_b(x, y)$ is given by [101]

$$\gamma = \frac{\Gamma}{2} \frac{I/I_s}{1 + I/I_s + 4(\delta/\Gamma)^2} \quad (4.14)$$

where Γ is the natural decay rate, δ is the detuning of the incoming laser of intensity I and I_s is the saturation intensity. Hence, the intensity reduces as the laser passes through the atoms in z -direction as

$$\frac{dI}{dz} = n(\mathbf{r})\sigma_0 \frac{I}{1 + I/I_s + 4(\delta/\Gamma)^2} \quad (4.15)$$

where $n(\mathbf{r})$ is the atomic density and $\sigma_0 = \frac{\hbar\omega\Gamma}{2I_s}$ is the resonant scattering cross section. This can be solved for the atomic density, yielding

$$\begin{aligned} \sigma_0 n(r) &= \frac{1}{I} \frac{dI}{dz} \left[1 + 4 \left(\frac{\delta}{\Gamma} \right)^2 \right] + \frac{1}{I_s} \frac{dI}{dz} \\ &= \frac{d \ln(I)}{dz} \left[1 + 4 \left(\frac{\delta}{\Gamma} \right)^2 \right] + \frac{1}{I_s} \frac{dI}{dz}. \end{aligned} \quad (4.16)$$

This can be easily integrated along the z -direction over the width of the cloud to obtain [102]

$$\sigma_0 n_c = \ln \left(\frac{I_b}{I_a} \right) \left[1 + 4 \left(\frac{\delta}{\Gamma} \right)^2 \right] + \frac{I_b - I_a}{I_s}, \quad (4.17)$$

where $n_c(x, y) = \int n(x, y, z) dz$ is the column density. We assumed that the intensity of the beam is $I_b(x, y)$ before and $I_a(x, y)$ after passing through the atomic cloud.

With the camera, we measure the mean intensities $I_k^{(i)} = \int_{(x,y) \in A_{\text{px}}^{(i)}} I_k(x, y)$ with $k = a, b$ in the areas $A_{\text{px}}^{(i)}$ corresponding to the individual pixel. If the intensities $I_a(x, y)$ and $I_b(x, y)$ are almost constant in these areas we can approximate

$$\int_{(x,y) \in A_{\text{px}}^{(i)}} \ln \left(\frac{I_b(x, y)}{I_a(x, y)} \right) dx dy \approx A_{\text{px}}^{(i)} \ln \left(\frac{I_b^{(i)}}{I_a^{(i)}} \right). \quad (4.18)$$

Finally, we approximate that the atom column density $n_c(x, y) \approx n_c^{(i)}$ is almost constant in the areas $A_{\text{px}}^{(i)}$ and can thus express the number of atoms $N^{(i)}$ in the corresponding column as

$$N^{(i)} = \int_{(x,y) \in A_{\text{px}}^{(i)}} n_c(x, y) dx dy \approx A_{\text{px}} n_c^{(i)}. \quad (4.19)$$

With these approximations, we can use the mean intensities recorded by the camera to estimate the number of atoms

$$N^{(i)} = \frac{A_{\text{px}}}{\sigma_0} \left(\ln \left(\frac{I_b^{(i)}}{I_a^{(i)}} \right) \left[1 + 4 \left(\frac{\delta}{\Gamma} \right)^2 \right] + \frac{I_b^{(i)} - I_a^{(i)}}{I_s} \right) \quad (4.20)$$

in each column.

4. Preparation, manipulation and detection of a ^{87}Rb spinor condensate

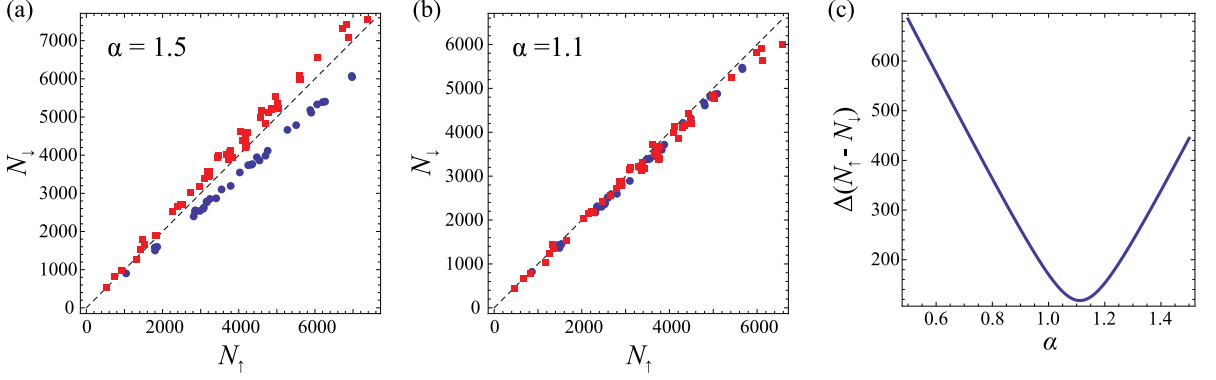


Figure 4.7.: **Calibration of the effective saturation intensity.** (a) Measurement of the number of atoms in the $m_F = \pm 1$ Zeeman levels after spin dynamics in the presence of a strong intensity gradient in the imaging beam. Between the measurement corresponding to the blue points and the measurement corresponding to the red squares the intensity gradient was reversed. The estimated number difference $N_\uparrow - N_\downarrow$ depends on this intensity gradient if we use an incorrect effective saturation intensity αI_s . (b) Only for the correct effective saturation intensity at $\alpha = 1.1$ the estimated number of atoms is independent of the intensity and the number difference is close to zero. (c) The correction factor α can be found by minimizing the fluctuations in the number difference.

4.4.3. Calibration of the absolute number of atoms

In the last section we derived a formula to calculate a number of atoms corresponding to each pixel. If an atomic cloud is imaged on a region of the CCD camera we can sum up the estimated number of atoms $N^{(i)}$ of the corresponding pixels to get a total number of atoms $N_{\text{est}} = \sum_i N^{(i)}$. After releasing the atoms from the trap we apply a strong magnetic field gradient. This gradient splits the ensemble in different clouds depending on their internal state, enabling us to count the atoms in the different levels separately. However, we need to carefully calibrate our imaging system to correctly estimate the number of atoms as will be described here.

First, in order to compute Eq. (4.20) we need to calibrate the intensity I recorded by the CCD camera. If the intensity calibration is incorrect (and assuming a linear error) we might estimate an intensity I rather than the true value βI . Such a calibration is carried out by measuring the gain of the camera, i.e. the number of counts per detected photon, and its quantum efficiency η , the fraction of detected photons. This procedure is described in appendix D.

Second, we need to know the exact value of the saturation intensity. For ideal σ^+ -polarized light, we expect $I_s = 16.69 \text{ W/m}^2$. However, residual components of the other polarizations and deviations from the ideal two-level system may lead to a true value of $\alpha' I_s$. Note, that the resonant scattering cross section $\sigma_0 \propto 1/I_s$ is also effected by a non-ideal saturation intensity $\sigma_0 \rightarrow \sigma_0/\alpha'$.

If we ignored both, the correction for the intensity βI and for the non-ideal saturation intensity $\alpha' I_s$ and assume $\delta = 0$, we would estimate a number of atoms

$$N_{\text{ideal}}^{(i)} = \frac{A_{\text{px}}}{\sigma_0} \left(\ln \left(\frac{I_b^{(i)}}{I_a^{(i)}} \right) + \frac{I_b^{(i)} - I_a^{(i)}}{I_s} \right) \quad (4.21)$$

rather than the true value

$$N_{\text{true}}^{(i)} = \frac{A_{\text{px}}}{\sigma_0} \left(\alpha \ln \left(\frac{I_b^{(i)}}{I_a^{(i)}} \right) + \beta \frac{I_b^{(i)} - I_a^{(i)}}{I_s} \right). \quad (4.22)$$

Here, the factor $\alpha \approx \alpha'(1 + 4(\delta/\Gamma)^2)$ also accounts for a possible detuning from resonance. Such a detuning is unavoidable since the atoms are accelerated during the imaging leading to a time dependent Doppler shift on the order of 1 MHz for an illumination time of 90 μs .

We are able to measure the saturation intensity α with a technique very similar to the one described in Ref. [102]. The central idea is to exploit that for a fixed number of atoms $N^{(i)}$ the linear second term of Eq.(4.22) increases and finally becomes equal to $N^{(i)}$, while the logarithmic term decreases and finally vanishes. The sum of both terms, however, is always equal to the number of atoms $N^{(i)}$ if α and β are correct. Hence, assuming that the intensity calibration is correct ($\beta = 1$), the estimated number of atoms is only independent of the illumination intensity if we compute it with the correct effective saturation intensity αI_s . To verify this, we measure the number of atoms N_{\uparrow} and N_{\downarrow} in the clouds corresponding to the $m_F = \pm 1$ levels that were populated by spin-dynamics and should ideally be equal. We use the strong intensity gradient off center from the Gaussian imaging beam to illuminate the two clouds with different intensities. After a series of measurements with fluctuating atom numbers in $m_F = \pm 1$ we invert the gradient. For the correct value of the effective saturation intensity αI_s , the fluctuations in the atom number difference $\Delta(N_{\uparrow} - N_{\downarrow})$ are minimized. We measure a correction factor of $\alpha = 1.1$ for the effective saturation intensity which compares well to results achieved in other groups by similar techniques [29]. Spin-dynamics is not necessary for our calibration method. Instead, a $\pi/2$ -microwave pulse could be used and one might look for minimized fluctuations in the fraction $N_{\uparrow}/N_{\downarrow}$ to account for small deviations from the ideal 50/50 splitting ratio.

The nonlinear part of Eq.(4.22) causes further complications. If the intensities $I_a(x, y)$ and $I_b(x, y)$ are strongly varying over the areas $A_{\text{px}}^{(i)}$ corresponding to the individual pixels we can no longer use the approximation Eq.(4.18) which was crucial for obtaining the formula Eq. (4.20) for the estimation of the number of atoms. This can lead to a nonlinear dependence of the estimated number of atoms N_{est} on the real number of atoms N as shown in Fig. 4.8c. Potentially, this can lead to underestimated fluctuations in the particle number $\Delta N_{\text{est}} < \Delta N$ and the measurement of sub-shot-noise fluctuations although the fluctuation are in fact above shot noise. The pixel area should thus be small compared to the cloud.

A similar effect can be observed if the estimated atom column densities $n_c(x, y)$ are no longer constant during the imaging time, which we assumed without mentioning in

4. Preparation, manipulation and detection of a ^{87}Rb spinor condensate

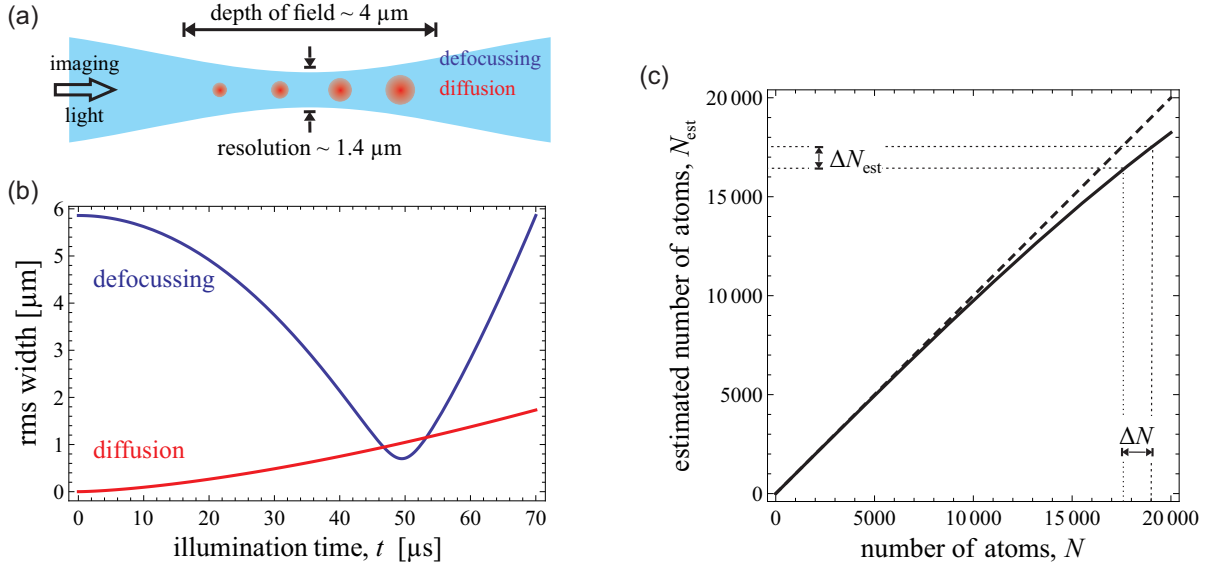


Figure 4.8.: **Blurring effects lead to a nonlinear number estimation.** (a) Two effects lead to a blurring of the image of the atomic cloud [97]. First, the scattered photons lead to recoil heating and a diffusion of the cloud by $w_{\text{rms}} = \frac{2}{3}v_{\text{rec}}\sqrt{\gamma}t^{\frac{3}{2}}$ [97, 103]. Second, the atomic cloud is pushed out of focus by the imaging beam. This reduces the resolution of the imaging system according to $w_0\sqrt{1 + (\frac{z}{z_R})^2}$, where z is the position relative to the focus, $z_R \approx 4 \mu\text{m}$ is the Rayleigh range and $w_0 \approx 0.7 \mu\text{m}$ is the ideal resolution of our detection system according to the Rayleigh criterion. (b) An estimation of both blurring effects at a given illumination time t and an intensity $I_b = 3I_s$ is shown here assuming a diffraction limited imaging system. For the actual blurring of the image in the experiment an integration of these effects over time has to be done and astigmatism of the imaging optics have to be considered. We assume that the starting and end position of the atomic cloud are at equal distance from the focal plane. (c) Example for a nonlinear estimation of the number of particles (solid line) deviating from the true value (dashed line). For our detection system, simulations show that this effect is negligible. At 5 000 atoms in a single cloud (corresponding to a total number of 10 000 atoms in our experiments) the estimated number of atoms is 0.1% below the true value and fluctuations are underestimated by less than 0.5%.

the discussion so far. This can be caused by two effects [97, 104] as depicted in Fig. 4.8a. First, the atom ensemble seems to expand since the imaging light beam pushes it out of the focal plane. Second, the scattering of photons leads to recoil heating and an expansion of the cloud. Neither of the two effects should increase the initial cloud radius significantly to avoid a nonlinear estimation of the number of atoms.

We can experimentally check for a nonlinearity in the estimation of the number of

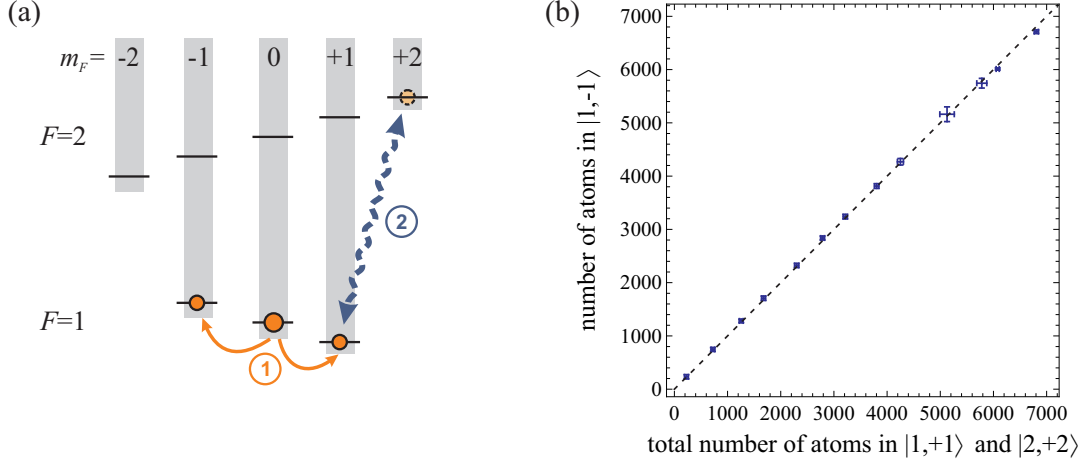


Figure 4.9.: **Experimental test of the linearity** (a) We verify the linearity of our absorption detection by the following procedure: First, spin dynamics is used to produce an equal population in the states $|F, m_F\rangle = |1, -1\rangle$ and $|1, +1\rangle$. Then, about one half of the atoms in $|1, +1\rangle$ is transferred to $|2, +2\rangle$ by a microwave pulse. Finally, we measure the number of atoms in these 3 states with absorption imaging. (b) Ideally, the total number of atoms in $|1, +1\rangle$ and $|2, +2\rangle$ is equal to the number of atoms in $|1, -1\rangle$ as indicated by the dashed line. A nonlinearity in the detection would lead to a stronger underestimation of the number of atoms in $|1, -1\rangle$ due to the higher density. Hence, our measurements (blue points with error bars) exclude a relevant nonlinearity of our detection system.

atoms by splitting up one of the output modes after spin dynamics into two clouds with a $\frac{\pi}{2}$ -pulse as shown in Fig. 4.9a. The sum of the number of atoms in these two clouds can be compared with the number of atoms in the other output mode. Ideally, these should be the same. However, if the imperfections of the detection system lead to a nonlinear error in the number estimation we expect a behaviour similar to the one shown in fig 4.8c when plotting these numbers against each other. A nonlinearity can be suppressed by decreasing the influence of the logarithmic term in Eq. (4.20). This term tends to zero for high intensities and low column densities which can be achieved by long expansion times. Experimentally we do not observe a significant nonlinear deviation for our imaging parameters up to $N = 7\,000$ atoms in a single cloud as shown in Fig. 4.9b.

As an independent check of the atom number calibration, we can measure the \sqrt{N} scaling of shot-noise. This is carried out by measuring the population N_{\uparrow} and N_{\downarrow} of two states after a $\frac{\pi}{2}$ -pulse for a varying total number of atoms $N = N_{\uparrow} + N_{\downarrow}$. In the following, each measurement of sub-shot-noise fluctuations is complemented by such a shot-noise measurement to prove the correct calibration of the imaging system.

4. Preparation, manipulation and detection of a ^{87}Rb spinor condensate

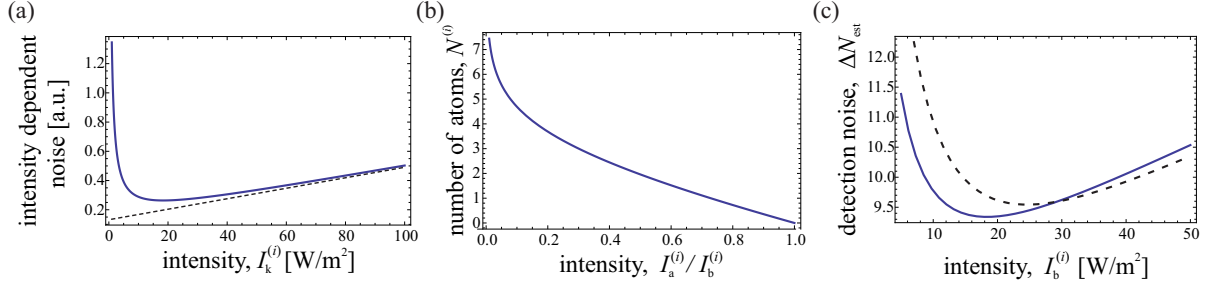


Figure 4.10.: **Intensity dependence of the photo-electron shot noise.** (a) The intensity dependent terms of Eq. (4.26) (blue line) are minimized for $I_k^{(i)} = I_s$. At high intensities the slope is given by the increasing shot noise $\propto \sqrt{I_k^{(i)}}$ (dashed black line). (b) Estimated atom number $N^{(i)}$ as a function of the relative intensity $I_a^{(i)}/I_b^{(i)}$. At low relative intensities, small intensity fluctuations translate to large fluctuations in the estimated number of atoms. (c) At $N = 0$, the minimal detection noise caused by photo-electric shot noise is achieved for $I_b^{(i)} = I_a^{(i)} = \alpha I_s$ (blue line). For a larger number of atoms $N = 10\,000$, the minimum is shifted to higher intensities since $I_b^{(i)} > I_a^{(i)}$ (dashed black line).

4.4.4. Photo-electron shot noise - the fundamental limit

For a precise estimation of the number of atoms, we need to minimize the fluctuations ΔN_{est} . For absorption imaging these fluctuations can be traced back to fluctuations of the intensities $\Delta I_a^{(i)}$ and $\Delta I_b^{(i)}$. Error propagation applied to Eq. (4.22) leads to

$$\Delta N^{(i)} = A_{\text{px}}^{(i)} \sqrt{\left(\Delta I_a^{(i)} \frac{\partial n_c^{(i)}}{\partial I_a^{(i)}} \right)^2 + \left(\Delta I_b^{(i)} \frac{\partial n_c^{(i)}}{\partial I_b^{(i)}} \right)^2} \quad (4.23)$$

where $n_c^{(i)}$ is the estimated column density corresponding to the i th pixel based on the measurements $I_a^{(i)}$ and $I_b^{(i)}$.

Besides technical noise sources, there is a fundamental unavoidable reason for the fluctuations $\Delta I_a^{(i)}$ and $\Delta I_b^{(i)}$: The $N_{\text{ph}}^{(i)}$ photons incident on a camera pixel are converted into $N_{\text{el}}^{(i)} = \eta N_{\text{ph}}^{(i)}$ electrons with a quantum efficiency η . The number of electrons can be measured and used to estimate the corresponding intensity

$$I^{(i)} = \frac{N_{\text{el}}^{(i)} h\nu}{\eta t A_{\text{px}}^{(i)}} \quad (4.24)$$

with the illumination time t . These electrons are subject to shot-noise fluctuations $\Delta N_{\text{el}} = \sqrt{N_{\text{el}}}$, leading to an uncertainty in the estimated intensity

$$\Delta I^{(i)} = \sqrt{N_{\text{el}}^{(i)}} \frac{h\nu}{\eta t A_{\text{px}}^{(i)}} = \sqrt{\frac{I^{(i)} \eta t A_{\text{px}}^{(i)}}{h\nu}} \frac{h\nu}{\eta t A_{\text{px}}^{(i)}} = \sqrt{I^{(i)}} \sqrt{\frac{h\nu}{\eta t A_{\text{px}}^{(i)}}}. \quad (4.25)$$

If we combine this with Eq. (4.23), we get

$$\Delta N^{(i)} = \sqrt{\frac{A_{\text{px}}^{(i)} h\nu}{\eta t}} \sqrt{\left(\sqrt{I_a^{(i)}} \frac{\partial n_c^{(i)}}{\partial I_a^{(i)}} \right)^2 + \left(\sqrt{I_b^{(i)}} \frac{\partial n_c^{(i)}}{\partial I_b^{(i)}} \right)^2} \quad (4.26)$$

for a photo-electron shot-noise limited absorption detection. If we want to calculate the number of atoms $N_{\text{est}} = \sum_i N^{(i)}$ in an atomic cloud, we have to take the sum over all relevant pixels. Since the photo-electron noise contributions of the pixels are independent, this leads to fluctuations in the estimated number of atoms according to

$$\Delta N_{\text{est}} = \sqrt{\sum_i (\Delta N^{(i)})^2}. \quad (4.27)$$

From Eq.(4.26), we can see the importance of several parameters. Not surprisingly, a large quantum efficiency η and a long illumination time t lead to a better estimation of the number of atoms, since more scattered photons are detected. The constraint on the illumination time is set by the blurring effects discussed in the last section. At a first glance, a small area in the object plane $A_{\text{px}}^{(i)}$ by increasing the magnification of the imaging system seems to be beneficial. Notice, however, that although the noise on a single pixel is reduced this is compensated by the increased number of pixels that we need to consider to cover the relevant region which leads to increased fluctuations ΔN_{est} according to Eq. (4.27). Confining the atoms to a smaller region $A = \sum_i A_{\text{px}}^{(i)}$, however, turns out to be beneficial. Again, the amount by which we can compress the cloud to a smaller region by a shorter expansion time or a delta kick [105, 106] is limited by the blurring effects for a given illumination time.

It is instructive to expand the intensity dependent parts of Eq. (4.26) under the square root using Eq. (4.17)

$$\left(\sqrt{I_k^{(i)}} \frac{\partial n_c^{(i)}}{\partial I_k^{(i)}} \right)^2 = \frac{1}{\sigma_0^2} \left(\frac{\alpha}{\sqrt{I_k^{(i)}}} + \frac{\sqrt{I_k^{(i)}}}{I_s} \right)^2, \quad (4.28)$$

which have the same form for $k = a$ and $k = b$. In the limit of low intensities $I_k^{(i)} \ll I_s$ almost all the light is scattered out of the imaging beam. Small intensity fluctuations thus translate to large fluctuations in the estimated number of atoms in this limit (see Fig. 4.10b). On the other hand, for high intensities $I_k^{(i)} \gg I_s$, the number of scattered photons does not increase with the intensity due to a saturation of the atomic transition.

The photon shot noise, however, is still increasing with $\sqrt{I_k^{(i)}}$ and the estimation of the number of atoms becomes worse. In between these two limits, the above equation has a minimum at $I_k^{(i)} = \alpha I_s$ as shown in Fig. 4.10a. Hence, we want both, $I_a^{(i)}$ and $I_b^{(i)}$, to be close to the effective saturation intensity αI_s .

This is confirmed by simulations shown in Fig. 4.10c. For these simulations we assume a Gaussian shaped atomic cloud with a root mean square radius of $25 \mu\text{m}$, an illumination

4. Preparation, manipulation and detection of a ^{87}Rb spinor condensate

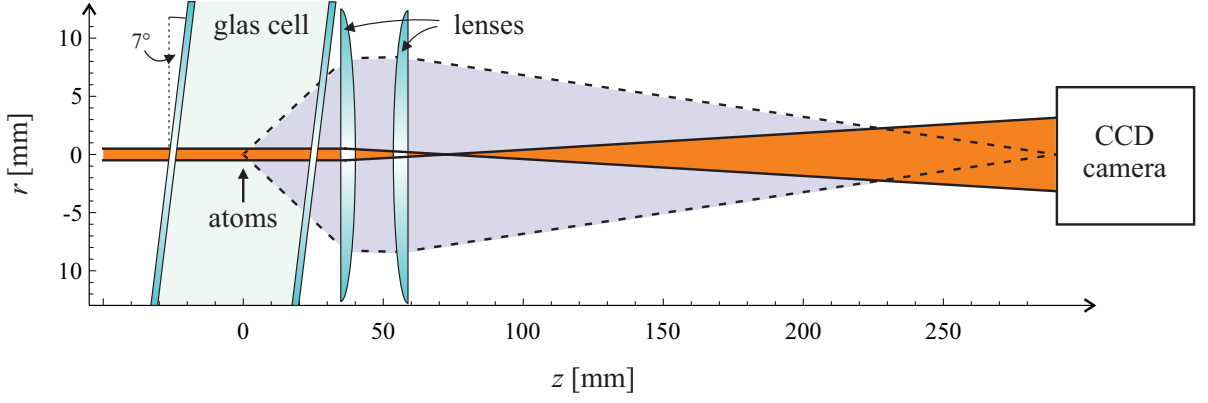


Figure 4.11.: **Schematic of the absorption imaging setup.** A resonant laser beam (orange area) illuminates the atoms. It passes through the vacuum glass cell at an angle of 7 degrees. Two lenses image the absorption signal of the atoms (grey area with dashed lines) on a CCD camera.

time of $70 \mu\text{s}$ and a quantum efficiency of 98%. We calculate the corresponding intensities $I_a^{(i)}$ and assume a constant intensity $I_b^{(i)}$. Optionally, the absorption image given by $I_a^{(i)}$ can be blurred with a Gaussian filter to account for the blurring effects described in the last section giving results as shown in Fig. 4.8c. We can use Eq. (4.26) to calculate the ideal photo-electron shot noise limited fluctuations on each pixel $\Delta N^{(i)}$. Finally, we use Eq. (4.27) to calculate a minimal detection noise of $\Delta N_{\text{est}} \approx 10$ atoms for our imaging parameters and our imaging intensity of $I_b^{(i)} \approx 40 \frac{\text{W}}{\text{m}^2}$. This intensity is slightly above the intensity for minimal detection noise at $N = 10\,000$. However, higher intensities reduce the nonlinearity of the detection system. The detection noise is almost independent on the number of atoms and ranges from $\Delta N_{\text{est}} = 10.6$ to 9.3 atoms in the interval from 0 to 10 000 atoms in a single cloud.

For the measurement of sub-shot-noise fluctuations of the output state of the spin dynamics described in chapter 3, we need to measure the number of atoms in the two $m_F = \pm 1$ levels. The photon shot noise limited fluctuations in the number difference thus increases by a factor of $\sqrt{2}$ to 14 atoms. This corresponds to a noise of 7 atoms in terms of ΔJ_z .

4.4.5. The setup for the high-precision absorption detection

Besides the fundamental photo-electron shot noise, there are technical noise sources leading to fluctuations in the intensities $\Delta I^{(i)}$, causing an increased uncertainty in the estimated number of atoms ΔN_{est} . The main problem arises from the diffraction of the coherent imaging beam due to dust particles or small imperfections of the imaging optics. This leads to small fringe structures that are sensitive to smallest mechanical vibrations (see Fig. 4.6b). Our setup for high-precision absorption imaging is designed to suppress these noise sources as will be described in this section.

The resonant imaging light is coupled out of a polarization maintaining single-mode fi-

bre (fibre: Schäfter + Kirchhoff PMC-780-5,4-NA011-3APC-300-P; fibre coupler: Schäfter + Kirchhoff 60FC-4-A4,5-02) resulting in a collimated laser beam with a waist of 0.4 mm. A small beam waist reduces etaloning effects due to a reduced overlap of the reflected and the unreflected beams. It also minimizes the chance to illuminate dust particles or defects in regions that are not essential for obtaining an absorption image. The polarization of the imaging beam is purified by a polarizing beam splitter and it is directed to the atoms by two mirrors. A 0th-order quarter wave plate is used to obtain σ_+ -polarization. The imaging beam enters the glass cell at an angle of 7 degrees to the surface normal to reduce etaloning effects and illuminates the atoms. At a distance of 36.5 mm from the atoms, an aspheric lens (Newport KPA16AR.16) with a focal length $f = 37.5$ mm and a achromatic lens (Qioptiq G322353525) with $f = 200$ mm image the intensity distribution on a CCD camera (princeton instruments pixis 1024.BR eXcelon) with a quantum efficiency of $\eta = 0.98$. This leads to a magnification factor of 6.2 such that the $13 \mu\text{m}$ edge length of the CCD pixels correspond to $2.1 \mu\text{m}$ in the object plane. The whole setup is mounted as rigid as possible to avoid mechanical vibrations.

We illuminate the atoms for $70 \mu\text{s}$ at an intensity of about $40 \frac{\text{W}}{\text{m}^2}$. The camera is operated in the so-called kinetic mode, which enables us to move the image pixels $I_a^{(i)}$ within less than 5 ms in a region covered by a razor blade to shield it from stray light. A second resonant laser beam coming from above pushes the atoms out of the imaging region. Then, the reference image $I_b^{(i)}$ is recorded and again quickly moved behind the stray light protection. Finally, an image with no light present is taken to estimate the amount of stray light and dark counts. It is beneficial to take these images with a minimal time delay such that the fringe patterns have not changed significantly.

By analyzing more than 800 images without atoms, we extract a detection noise of 22.3(5) atoms in the atom number difference. If we quadratically subtract the photo-electron shot noise contribution of 14 atoms (see last section) we can estimate to have technical noise on the order of 17 atoms left.

The photo-electron shot noise contribution of the beam image $I_b^{(i)}$ can be reduced by averaging several images of the imaging beam intensity. In the ideal case, we would expect that the photo-electron shot noise of the beam image is suppressed by a factor $\frac{1}{\sqrt{m}}$ in such an averaged image, where m is the number of individual images. However, since the interference fringe structures change in time, the individual images can in general have very different intensity distributions and a simple average reference image leads in our case to increased detection noise. Reference [107] introduced a simple method to calculate an optimal reference image

$$I_{\text{opt}}^{(i)} = \sum_j c_j I_{b,j}^{(i)} \quad (4.29)$$

as a superposition of a set of reference images $\{I_{b,j}^{(i)}\}$ such that that the least squares difference

$$\sum_{i \notin A} \left(I_a^{(i)} - I_{\text{opt}}^{(i)} \right)^2 \quad (4.30)$$

is minimized outside of the region A occupied by the atomic clouds. In order to find

4. Preparation, manipulation and detection of a ^{87}Rb spinor condensate

the local minimum of the above equation, the partial derivatives with respect to the coefficients c_j is set to zero yielding

$$\sum_j c_j M_{k,j} = \sum_{i \notin A} I_{b,j}^{(i)} I_a^{(i)}. \quad (4.31)$$

Here the matrix

$$M_{k,j} = \sum_{i \notin A} I_{b,k}^{(i)} I_{b,j}^{(i)} \quad (4.32)$$

contains the overlap of the different reference images and can be calculated once before analyzing a set of absorption images. The linear equation system Eq. (4.31) can be solved to find the coefficients c_j and thereby the optimal reference image.

With this method, we can reduce the detection noise from 22.3(5) atoms to 19.7(5) atoms using linear combinations of 500 reference images as optimal reference images.

4.4.6. Estimation of the detection noise

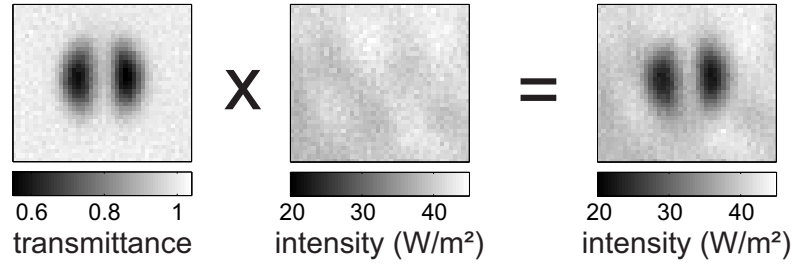


Figure 4.12.: **Creation of an artificial absorption image.** The optical transmittance of an idealized atomic cloud $1 - a^{(i)}$ is calculated from an average of many experimental absorption images. A typical detection image without atoms is multiplied by the optical transmittance to gain a synthetic absorption image with adjustable number of atoms.

It was shown in section 4.4.4 that the photo-electron shot noise contribution to the detection noise is almost independent of the total number of atoms. Intensity fluctuations caused by other noise sources should lead to a detection noise which increases with the number of particles since the estimation of the number of atoms becomes more sensitive to these fluctuations at higher densities (see Fig. 4.10b).

The estimation of these increased fluctuations for larger ensembles cannot be measured directly since one needs to distinguish between real fluctuations in the number of atoms and fluctuations in its estimation. We synthesize artificial absorption images that mimic a constant number of atoms without shot to shot fluctuations to avoid this problem. These artificial images are obtained by the following procedure: First, we calculate the average absorption $a^{(i)} = 1 - \frac{I_a^{(i)}}{I_b^{(i)}}$ on the pixels from over 100 absorption images

containing more than 1 000 atoms. We can mimic the absorption of a cloud by reducing the intensity $I_a^{(i)}$ of an image without atoms according to

$$\tilde{I}_a^{(i)} = (1 - x a^{(i)}) I_a^{(i)}. \quad (4.33)$$

With the parameter x we can adjust the strength of the artificial absorption. If we apply Eq.(4.22) to the artificial absorption image $\tilde{I}_a^{(i)}$, there will be slight deviations in the estimated density leading to fluctuations of the number of atoms from shot to shot. These fluctuations for the synthetic absorption images are an estimation of the fluctuations of the real absorption images of a perfect noiseless atomic state. The photo-electron shot noise of the absorption image is underestimated by this method since we reduce it by a factor of $1 - x a^{(i)}$ while the shot-noise fluctuations would be reduced by $\sqrt{1 - x a^{(i)}}$ for a real absorption of this fraction of photons. Nonetheless, this estimation is in qualitative agreement with the slightly increased noise at larger numbers of atoms observed in the experiment (see section 6.3).

5. The twin-Fock interferometer

In chapter 3, we have seen that we can use spin dynamics to create a two-mode squeezed vacuum state which is a superposition of twin-Fock states with an identical number of atoms in the two spin states $m_F = \pm 1$. In this chapter, we will present an experiment proving the usefulness of these states for interferometry beyond the classical limit.

Since the measurements discussed in this chapter, the experimental setup has been improved. In particular, the detection noise has been reduced by a factor of two. The apparatus used for the experiments presented here is described in greater detail in Ref. [91].

5.1. Beyond spin squeezing

In section 2.4 we have seen that spin-squeezed states are useful for overcoming the shot-noise limit in a standard interferometer. However, spin-squeezed states are only a small class in the larger class of all possible entangled states. This raises the question if there are other entangled or only classically correlated states that are useful for quantum-enhanced interferometry. This would imply that we cannot use the mean number of particles at the output port of the interferometer to estimate the phase since such a phase estimation can only be improved by spin-squeezed states (see section 2.4).

A. Smerzi and L. Pezzé found the following way to decide whether a state is useful for interferometry or not and proved that entanglement is a key ingredient [108]. The phase sensitivity is fundamentally limited by the Cramer-Rao bound [109]

$$\Delta\phi_{\text{est}} \geq \frac{1}{\sqrt{F_Q}} \quad (5.1)$$

where F_Q is the so-called quantum Fisher information which depends on the input state of the interferometer. Hence, the parameter

$$\chi^2 = \frac{N}{F_Q} \quad (5.2)$$

gives the achievable quantum-enhanced sensitivity compared to shot noise:

$$\Delta\phi_{\text{est}} \geq \frac{\chi}{\sqrt{N}}. \quad (5.3)$$

Since the Fisher information is bound by $F_Q < N^2$, the Heisenberg limit cannot be surpassed. Furthermore, they proved that states fulfilling $\chi^2 < 1$ are entangled.

In summary, states with a Fisher information $F_Q > N$ provide entanglement which is useful for sub-shot-noise interferometry. For a comparison with the spin-squeezing

5. The twin-Fock interferometer

parameter ξ , it can be shown that $\chi \leq \xi$ [110]. There are entangled states $\chi < 1$, that do not belong to the class of spin-squeezed states $\xi \geq 1$, but are useful for quantum-enhanced interferometry. In the following, we will show that the twin-Fock state is an example for such a state.

5.2. The principle of the twin-Fock interferometer

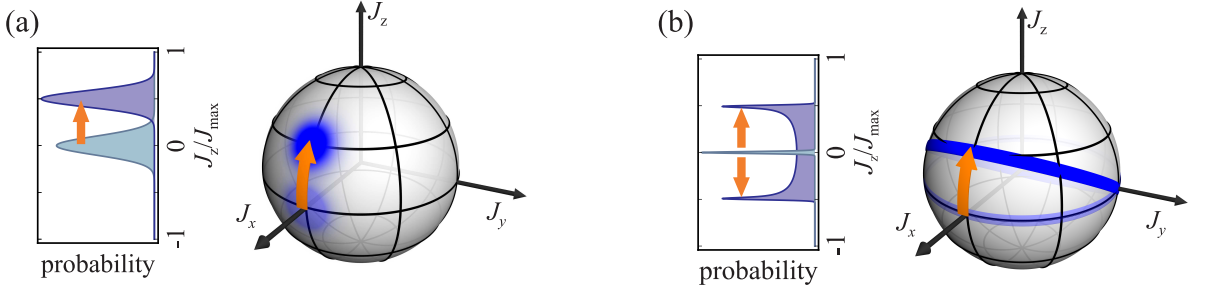


Figure 5.1.: **A classical interferometer compared with the twin-Fock interferometer.** On the generalized Bloch sphere an interferometer acts as a rotation around the y -axis by an angle ϕ given by the phase shift. The recorded difference of the number of particles at the two output ports $2J_z = N_{\uparrow} - N_{\downarrow}$ corresponds to a projection of the turned state on the z -axis. (a) The classical interferometer is operated with uncorrelated particles in a spin coherent state yielding a binomial distribution. The mean of this distribution $\langle J_z \rangle$ can be used to estimate the phase ϕ . (b) When operated with a twin-Fock state, the mean population imbalance always vanishes independent on the turning angle. However, the width of the distribution is highly sensitive to the turning angle and can be used for phase estimation close to the Heisenberg limit.

In section 3.5, we have seen that a twin-Fock state $|\frac{N}{2}, \frac{N}{2}\rangle$ with the same number of particles in the two modes of the pseudo spin basis can be represented as ring around the equator of the generalized Bloch sphere as shown in Fig. 5.1b. The vanishing width along J_z reflects its well defined difference in the number of particles in the two states $2J_z = N_{\uparrow} - N_{\downarrow} = 0$. The phase, on the other hand, is completely undefined as the mean collective spin vanishes $(\langle J_x \rangle, \langle J_y \rangle, \langle J_z \rangle)^T = (0, 0, 0)^T$ and makes it impossible to define an angle φ with respect to the x -axis. At a first glance, it seems unlikely that such a state with a completely undefined phase can be used for a precise phase estimation. However, as we have seen in section 2.3.4 the first beamsplitter of an interferometer acts as a $\frac{\pi}{2}$ rotation around the x -axis, turning the ring upright and thereby converts the well defined difference in the number of particles into a precisely defined phase. The fluctuations in the population difference, on the other hand, are greatly increased.

As discussed in section 2.3.4, the interferometer sequence acts as a rotation of ϕ around the y -axis on the collective spin. At the end of the interferometer sequence,

the population difference in the two modes can be measured which corresponds to a projection on J_z . For a spin coherent state, such a measurement yields a Gaussian distribution whose mean value can be used for the estimation of the phase (see Fig. 5.1a and section 2.2.1). For a spin-squeezed input state, we expect a similar result with a narrower distribution improving the estimation of the mean population imbalance.

For a twin-Fock state, however, the mean of the resulting distribution does not depend on the phase shift ϕ experienced in the interferometer. The mean of the collective spin $\langle J_x \rangle = \langle J_y \rangle = \langle J_z \rangle = 0$ always vanishes independent on the turning angle on the generalized Bloch sphere. This shows that the twin-Fock state is not useful for standard phase estimation. It does thus not belong to the class of spin-squeezed states and it can be shown that $\xi = 1$ for the ideal twin-Fock state [111]. As mentioned in the previous section, such a state can still be useful for quantum-enhanced interferometry with a phase estimation which is not extracted from the mean of the distribution. In the case of the twin-Fock interferometer, the shape of the distribution at the output of the interferometer depends on the phase shift ϕ . Holland and Burnett showed that the twin-Fock state can indeed be used for phase estimation close to the Heisenberg limit [58, 112]. The width of the distribution is particularly well suited for estimating the turning angle (see Fig. 5.1b).

So far, such a twin-Fock interferometer has only been realized with up to four photons [113, 114] and two ions [115]. In the following, we will describe how we could create a state close to a perfect twin-Fock state consisting of up to 10 000 ^{87}Rb atoms and prove its usefulness for interferometry.

5.3. Experimental creation of twin-Fock states

With spin dynamics we can create a superposition of twin-Fock states with a varying total number of particles as shown in section 3.5. To this end, we prepare a Bose-Einstein condensate of about 28 000 ^{87}Rb atoms in the Zeeman level $m_F = 0$ in the $F = 2$ manifold. In order to fulfil the resonance condition for spin dynamics (see section 3.3) we have to tune the energy of the involved internal and external states to achieve energy conservation.

For the special case of $J = \frac{1}{2}$, which is valid for ^{87}Rb atoms in the $5^2S_{1/2}$ ground state, the energy splitting $\Delta E(F, m_F, B)$ of the different Zeeman hyperfine states $|F, m_F\rangle$ in a magnetic field B can be analytically expressed by the Breit-Rabi formula [116].

$$\Delta E(F = I \pm \frac{1}{2}, m_F, B) = \frac{-\Delta E_0}{4(I + \frac{1}{2})} + m_F g_I \mu_I B \pm \frac{\Delta E_0}{2} \sqrt{1 + \frac{4m_F}{2I + 1} \alpha B + (\alpha B)^2} \quad (5.4)$$

Here, $\alpha = \frac{g_J \mu_B - g_I \mu_I}{\Delta E_0}$ and μ_B is the Bohr magneton. For ^{87}Rb the nuclear spin is $I = \frac{3}{2}$ and the product of its Landé g -factor g_I and its magnetic moment μ_I is $g_I \mu_I = -9.951414 \cdot 10^{-4} \mu_B$. Hence, for ^{87}Rb the Breit-Rabi formula reads

$$\Delta E(F = \frac{3}{2} \pm \frac{1}{2}, m_F, B) = \frac{-\Delta E_0}{8} + m_F g_I \mu_I B \pm \frac{\Delta E_0}{2} \sqrt{1 + m_F \alpha B + (\alpha B)^2}. \quad (5.5)$$

5. The twin-Fock interferometer

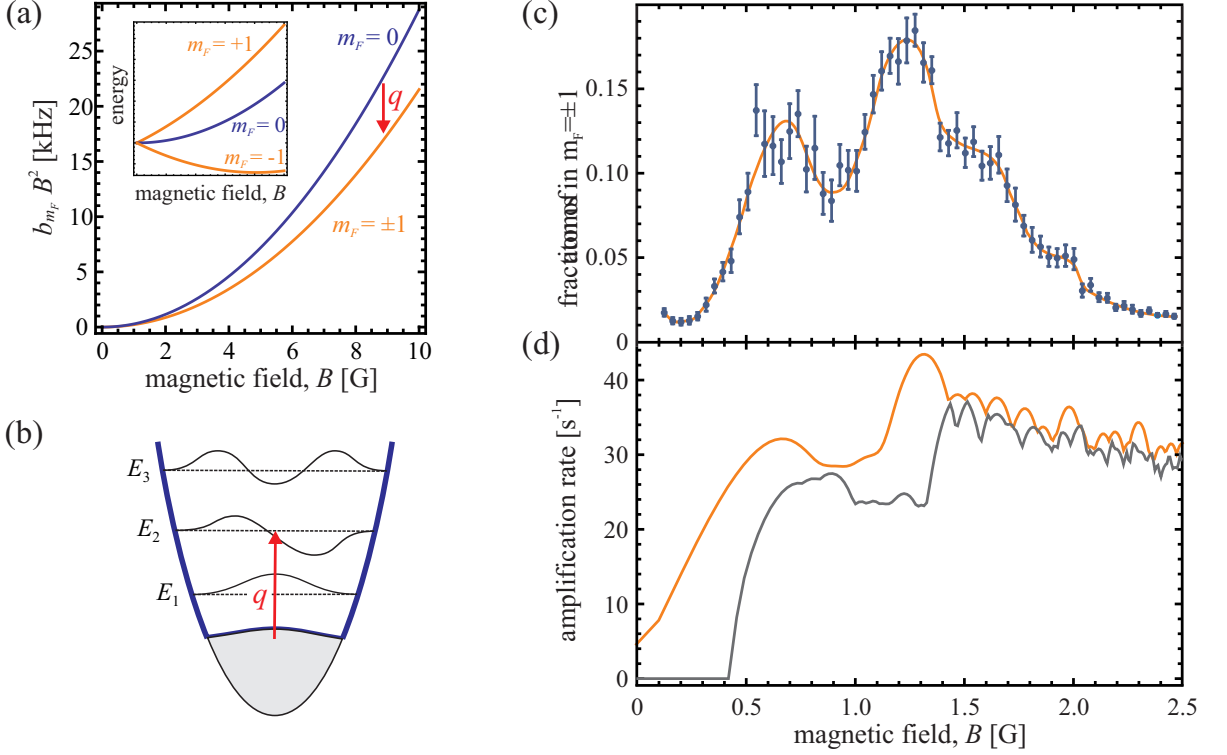


Figure 5.2.: **Spin dynamics resonances.** (a) At low magnetic fields B , the splitting of the Zeeman levels can be approximated by a linear and a quadratic term. In the inset we reduced the linear contribution by a factor of 200 to make the quadratic contribution in $F = 2$ visible. In the calculation of the internal energy change, the linear parts of the Zeeman shifts cancel. The remaining quadratic term $b_{m_F} B^2$ is larger for the $m_F = 0$ level and the internal energy is thus reduced. (b) If the released internal energy is close to the energy needed to populate an eigenstate of the effective potential for the $m_F = \pm 1$ atoms, a resonance occurs. (c) Hence, the fraction of atoms transferred to $m_F = \pm 1$ after an evolution time of 18 ms depends on the magnetic field. (d) The position of the experimentally observed resonances are given by the maxima of the numerically calculated amplification rate $\text{Im}(E)$. The orange line shows the highest amplification rate for a given magnetic field and the grey line corresponds to the mode with the second largest amplification rate.

The Landé factor of the fine structure spin is equal to the Landé g -factor of the electron $g_J = g_e = 2.0023$. The splitting ΔE_0 of the two hyperfine manifolds $F = \frac{3}{2} + \frac{1}{2} = 2$ and $F = \frac{3}{2} - \frac{1}{2} = 1$ at $B = 0$ is $\Delta E = 9.83468$ GHz.

At small magnetic fields, this energy shift $\Delta E(F = 2, m_F, B)$ can be approximated by a linear and a quadratic contribution.

$$\Delta E(F = 2, m_F, B) \approx c + a m_F B - b_{m_F} B^2 \quad (5.6)$$

The linear contribution is

$$a = g_I \mu_I + \frac{\Delta E_0 \alpha}{4} = 700 \frac{\text{kHz}}{\text{G}} \quad (5.7)$$

and the quadratic contribution is

$$b_{m_F} = \frac{\Delta E_0 \alpha^2}{4} \left(1 - \frac{m_F^2}{4}\right) = 288 \frac{\text{Hz}}{\text{G}^2} - m_F^2 72 \frac{\text{Hz}}{\text{G}^2} \quad (5.8)$$

for the different Zeeman levels in the $F = 2$ manifold. For $F = 1$ we find the same values with a negative sign. If we calculate the difference $2q$ of the internal energy of two atoms before and after a spin-changing collision from $m_F = 0$ to $m_F = \pm 1$ or $m_F = \pm 2$ in $F = 2$

$$2q = 2\Delta E(2, 0, B) - (\Delta E(2, m_F, B) + \Delta E(2, -m_F, B)) = -2m_F^2 \cdot 72 \frac{\text{Hz}}{\text{G}^2} B^2, \quad (5.9)$$

we see that we have lost some internal energy. This can be compensated by the increased external energy E_n of the populated eigenmode of the effective potential such that $E_n + 2q = 0$. By tuning the magnetic field, we can thus observe multiple spin dynamics resonances as shown in Fig. 5.2c. These resonances correspond to eigenmodes of the effective potential. This is confirmed by the characteristic density profiles observed on the different resonances [30, 73].

When we tune the magnetic field to the resonance at 1.23 G, we observe an initial exponential increase of the number of particles in the $m_F = \pm 1$ levels. After a spin dynamics time of about 15 ms, the population of these states does not increase exponentially any longer and starts to saturate as shown in Fig. 5.3a. This can be partially explained by a depletion of the $m_F = 0$ condensate as explained in section 3.6.

In summary, we create a twin-Fock state by tuning the magnetic field to the resonance condition for spin-changing collisions. We populate the $m_F = \pm 1$ states with up to 10 000 atoms within a spin dynamics time of 15 ms.

5.4. Measurement of sub-shot-noise number fluctuations

A first indication that the state produced by spin dynamics is entangled and useful for enhanced interferometric sensitivity are fluctuations below shot noise in the population difference $\Delta J_z < \frac{1}{2}\sqrt{N}$. The result of such a measurement is shown in Fig. 5.3b. The recorded fluctuations are limited by the detection noise of $\Delta N_{\text{est}} \approx \sqrt{2} \cdot 20(1)$ atoms which is almost independent of the total number of atoms. In the interval from $N = N_{\uparrow} + N_{\downarrow} = 7\,700$ to 9 000 atoms in the $m_F = \pm 1$ levels we achieve a number squeezing of $\frac{(\Delta(N_{\uparrow} - N_{\downarrow}))^2}{N_{\uparrow} + N_{\downarrow}} = -6.9(9)$ dB. Since this result is only limited by our detection noise, we expect the true amount of number squeezing to be much better. To confirm that we have a correct calibration of the number of atoms we record the fluctuations of a spin coherent state prepared by microwave pulses. These fluctuations are well described by the combination of the atomic shot noise and our detection noise.

5. The twin-Fock interferometer

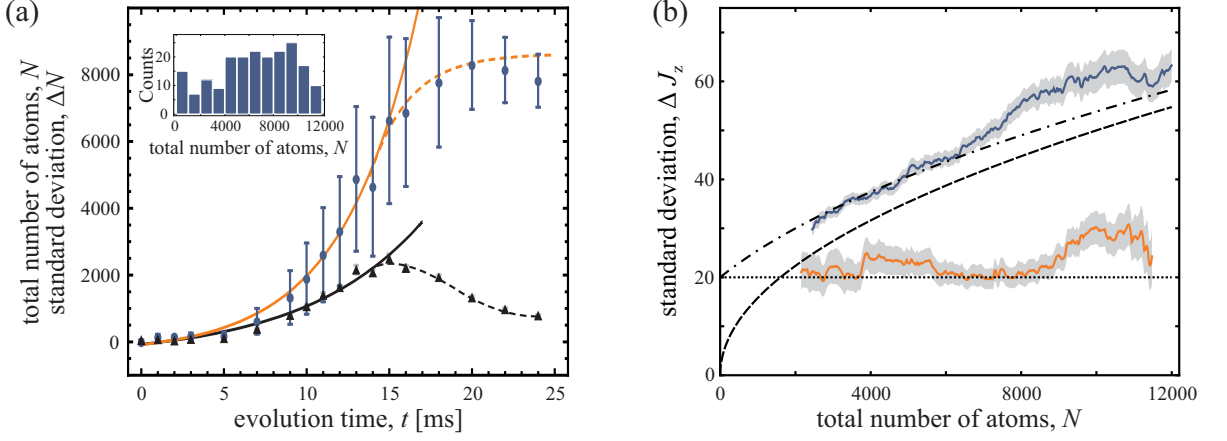


Figure 5.3.: **Time evolution and fluctuations of the produced state.** (a) Initially, the total number of atoms in the levels $m_F = \pm 1$ (blue points) as well as its fluctuations (black triangles) grow exponentially with time. After 15 ms, however, the population in $m_F = \pm 1$ ceases to grow exponentially and later, a saturation sets in. The inset shows a typical distribution of the total number of atoms in the $m_f = \pm 1$ levels after 15 ms evolution time. (b) For this evolution time, we record fluctuations of the population difference ΔJ_z (orange line) below shot noise (dashed black line). These fluctuations are mainly limited by our detection noise (dotted black line). To confirm the calibration of the absolute number of atoms, we measure the fluctuations of a spin coherent state (blue line) which is in reasonable agreement with the combination of shot noise and detection noise (dash-dotted black line). The individual data points are obtained from calculating the mean total number of atoms $\langle N \rangle$ and the standard deviation in the population imbalance ΔJ_z of post-selected ensembles with $N \in [x - 1\,000, x + 1\,000]$.

5.5. Estimation of the sensitivity gain

For an estimation of the usefulness of the state as a resource for quantum-enhanced interferometry, we need to turn the state on the generalized Bloch sphere by an angle θ and thereby mimic the effect of an interferometer with a phase shift of $\phi = \theta$. A proof of enhanced sensitivity is carried out by estimating this defined turning angle with a precision beyond shot noise.

We can realize this rotation by coupling the states with the help of microwave transitions. A two-photon transition is needed for a direct coupling of the $m_F = \pm 1$ levels. A two-photon transition with a reasonable detuning to the intermediate state is comparably slow and thus very sensitive to magnetic field fluctuations. Instead, we first transfer the atoms from $|F, m_F\rangle = |2, -1\rangle$ to $|1, 0\rangle$ with a microwave π -pulse. Thereby, we switch to a new pseudo spin basis formed by the levels $|\downarrow\rangle = |1, 0\rangle$ and $|\uparrow\rangle = |2, +1\rangle$ which can be easily coupled with microwave pulses. This transfer pulse shifts the phase of the atoms in the $|\downarrow\rangle$ level. However, the phase difference is completely undefined and

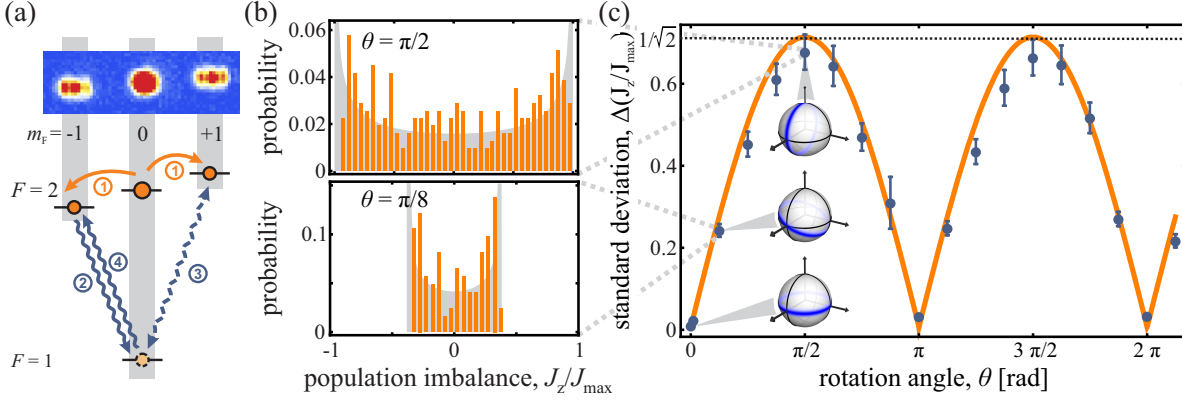


Figure 5.4.: **Turning the state on the generalized Bloch sphere** (a) The collective spin can be rotated on the generalized Bloch sphere by a microwave coupling pulse. For this purpose, we first transfer the atoms from $|F, m_F\rangle = |2, -1\rangle$ to $|1, 0\rangle$ with a π -pulse (2) after spin dynamics (1). This enables us to apply a coupling pulse (3) between the levels $|1, 0\rangle$ and $|2, +1\rangle$. Finally, we transfer the atoms in $|1, 0\rangle$ to $|2, -1\rangle$ (4) for the spatial separation by a strong magnetic field gradient. (b) The measured probability distributions of the normalized population imbalance $\frac{J_z}{J_{\max}}$ have a characteristic shape (orange) which is in reasonable agreement with the calculation (grey shaded area). (c) The measured standard deviations of these distributions (blue points) depend on the turning angle θ and are close to the ideal signal (orange line).

such phase shifts thus don't corrupt the ideal twin-Fock state. If a fraction of the atoms is not transferred, on the other hand, the number squeezing can be reduced. For an investigation of this effect, we transfer the atoms back to the $|2, -1\rangle$ level. This enables us to separate the atoms by applying a strong magnetic field gradient as explained in section 4.4.3. After these two transfer pulses, we are still able to detect number squeezing which is not significantly deteriorated.

If we introduce a pulse which couples the $|1, 0\rangle$ and the $|2, +1\rangle$ levels in between these transfer pulses, we are able to turn the state on the generalized Bloch sphere. By changing the duration of the coupling pulse, we can change the turning angle θ and observe the resulting distribution of the population difference as shown in Fig. 5.4b. Especially for a rotation angle of $\theta = \frac{\pi}{2}$ this distribution has an intriguing shape. Ideally, the probability to find all atoms in $m_F = +1$ and the probability to find all atoms in $m_F = -1$ are highest while an equal partition is very unlikely.

We aim to use the width of these distributions $(\Delta J_z)^2 = J_z^2$ as a signal to estimate the turning angle θ . In Fig. 5.4c, we plot this width measured in terms of the standard deviation of the normalized population imbalance $\Delta\left(\frac{J_z}{J_{\max}}\right)$ for all realizations with a total number of 3 000 to 8 000 atoms. Here, $J_{\max} = \frac{N}{2}$ is the maximal achievable collective spin length. In agreement with calculations, the Bloch sphere picture suggests that this

5. The twin-Fock interferometer

width is given by

$$\langle J_z^2 \rangle \approx \frac{1}{2} \langle J_{\text{eff}}^2 \rangle \sin \theta. \quad (5.10)$$

as obtained from a projection of the rotated ring on the z -axis. Here, the so-called effective spin length $\langle J_{\text{eff}} \rangle = \langle J_x^2 + J_y^2 \rangle$ is the radius of the ring on the generalized Bloch sphere and is connected to the contrast of the interferometer. For the normalized signal, we obtain

$$\Delta \left(\frac{J_z}{J_{\text{max}}} \right) = \alpha |\sin \theta| \quad \text{with} \quad \alpha = \sqrt{\frac{J_{\text{eff}}}{2J_{\text{max}}}} \quad (5.11)$$

In the experiment, we achieve a value of $\alpha = 0.67(4)$ which is close to the optimum $\alpha = \frac{1}{\sqrt{2}} \approx 0.71$.

For a small deviation δJ_z^2 from the mean width $\langle J_z^2 \rangle$, we can assume a linear dependence of the estimated turning angle θ_{est} on this deviation

$$\theta_{\text{est}} = \theta_0 + \delta J_z^2 \frac{\partial \theta}{\partial \langle J_z^2 \rangle}, \quad (5.12)$$

where θ_0 is the result of a phase estimation if $\langle J_z^2 \rangle$ is measured. Hence, the sensitivity for the estimation of θ can be written as

$$\Delta \theta_{\text{est}} = \frac{\Delta(J_z^2)}{\left(\frac{\partial \langle J_z^2 \rangle}{\partial \theta} \right)}. \quad (5.13)$$

In order to compute this value, we need to know the width $\langle J_z^2 \rangle$ and its fluctuations $\Delta(J_z^2) = \langle J_z^4 \rangle - \langle J_z^2 \rangle^2$ as a function of the turning angle θ . At small rotation angles, this can be estimated from a quadratic fit of the form $a + b\theta^2$ to the experimental data as shown in Fig. 5.5a and b. This accounts for the leading terms of the ideal signal in the presence of detection noise. With a bootstrap method, we can estimate the error of the fitted curve. Finally, we can combine the results to estimate the sensitivity. At an angle of 0.018 rad, the sensitivity is $-1.61_{-1.1}^{+0.98}$ dB below the shot-noise limit. Moreover, it is well below the limit set by the combination of shot-noise and our detection noise, which cannot be beaten by any classical state measured with our detection system. This proves that the created state is useful for phase estimation beyond the shot-noise limit. According to Eq. (5.3), we can deduce a Fisher information of $F \geq 1.45_{-0.29}^{+0.42} \langle N \rangle$, proving that the state is entangled.

5.6. Sensitivity limit set by the detection noise

The main limitation of the presented phase sensitivity beyond the shot-noise level is our detection noise. In the meanwhile, we improved our absorption detection and achieve a detection noise as low as 11 atoms in terms of ΔJ_z (see section 4.4.5). According to Fig. 5.6a, this would enable us to achieve a sensitivity gain of almost $\frac{(\Delta \theta_{\text{est}})^2}{(\Delta \theta_{\text{sn}})^2} \approx -8$ dB which corresponds to a variance six times smaller than the shot-noise limit $(\Delta \theta_{\text{sn}})^2 = \frac{1}{N}$.

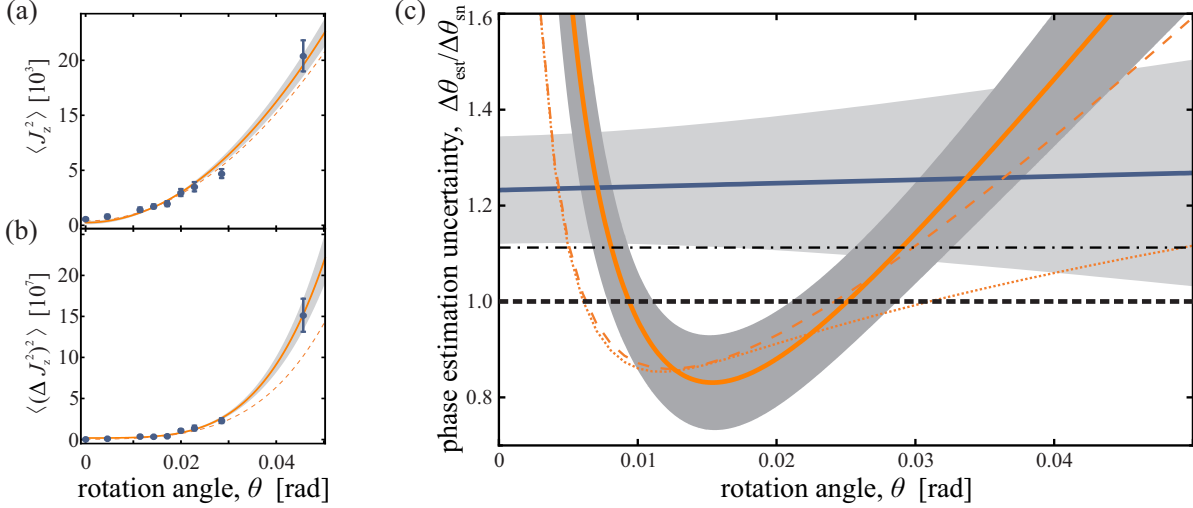


Figure 5.5.: **Measurement of the phase sensitivity.** (a) In order to measure the phase estimation sensitivity $\Delta\phi_{\text{est}} = \Delta\theta_{\text{est}}$, we record the width $\langle J_z^2 \rangle$ for a total number of atoms between 6400 and 7600 (blue points) and apply a quadratic fit (orange line). With a bootstrap method, we can estimate the uncertainty of this fit (grey shaded area) which is in reasonable agreement with the ideal signal including our detection noise (dashed orange line). (b) Additionally, we have to do the same estimation for the error of the measured width. (c) With error propagation, we can extract the phase estimation sensitivity (orange line) and its error (grey area) from the fitted curves. The result is below the shot-noise limit (dashed black line) and well below the limit set by the combination of shot noise and our detection noise (dash-dotted black line). All phase estimations obtained from measurements with uncorrelated particles and our detection capabilities (blue line) are constrained to sensitivities above this limit. The measured phase sensitivity of the twin-Fock state is in reasonable agreement with the prediction including our detection noise (dashed orange line). In principle, it is possible to improve the sensitivity for larger rotation angles with a Bayesian analysis and to saturate the Cramer-Rao bound (dotted orange line).

Theoretically, a detection with single-atom resolution allows for a phase sensitivity close to the Heisenberg limit. Moreover, it would be possible to resolve the peculiar structure of the probability distribution of the number of atoms after a coupling pulse shown in Fig. 5.6b. For a symmetric mixing of the two modes of a twin-Fock state with a $\frac{\pi}{2}$ -pulse, only even or only odd numbers of atoms occur in the output modes depending on the parity of $\frac{N}{2}$. This can be seen as a generalized version of the Hong-Ou-Mandel bunching effect [117].

This effect leads to a strong dependence of the parity on the turning angle close to multiples of $\theta = \frac{\pi}{2}$. Indeed, it has been shown that a detection of the parity of the number of atoms in one output port only is sufficient to achieve Heisenberg scaling [54].

5. The twin-Fock interferometer

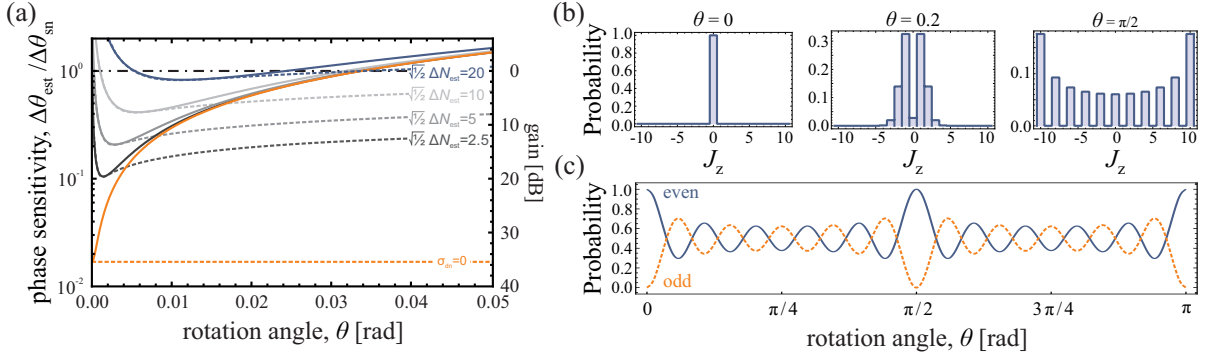


Figure 5.6.: **Sensitivity limits set by the detection noise and the ideal atomic distributions.** (a) Phase sensitivities for different levels of Gaussian detection noise and a total number of 7 000 atoms. The dashed lines are the Cramer-Rao bounds and the solid lines are the achieved sensitivities using J_z^2 for the estimation. (b) Ideal probability distributions of a twin-Fock state with a total number of 20 atoms for different turning angles. (c) Probability to find an even (solid blue line) or odd (dashed orange line) number of atoms at an output port. The calculation assumes an twin-Fock input state containing 20 atoms.

At small total numbers of atoms, it is even possible to achieve a sensitivity beyond the Heisenberg limit $\Delta\theta_{\text{est}} < \frac{1}{\langle N \rangle}$ if the two-mode squeezed vacuum is used as input state. This is possible due to the strongly fluctuating total number of atoms $\Delta N \gg \sqrt{N}$ [53].

6. Multi-particle entanglement in a spinor Bose-Einstein condensate

In the last section, a phase sensitivity beyond the shot-noise limit has been demonstrated for the state produced by spin-dynamics. This proves that the state contains entanglement, but in a rather indirect measurement.

In this chapter, we will establish a direct prove and a further quantification of the entanglement. Since the state describes up to 10 000 atoms, it is particularly interesting to ask if it contains more than pairwise entanglement. We show how we are able to apply new theoretical tools developed in cooperation with the group of Géza Tóth to characterize the experimentally created state. We measure a generalized spin-squeezing parameter of $-11.4(5)$ dB, the best result reported for any atomic system, and prove genuine 28-particle entanglement.

6.1. Entanglement detection based on measurements of the collective spin

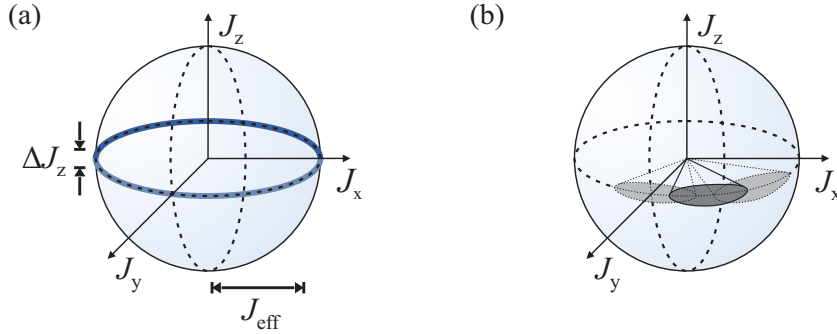


Figure 6.1.: **Generalized spin squeezing.** (a) The generalized spin-squeezing parameter compares the fluctuations of the population imbalance ΔJ_z with the spin length J_{eff} in the x - y -plane. It is optimal to detect a twin-Fock state, which has vanishing fluctuations $\Delta J_z = 0$ and a maximal radius $J_{\text{eff}} \approx J_{\text{max}}$. (b) Phase noise leads to a stretching of a spin-squeezed state along the equator of the generalized Bloch sphere. It can be described as an incoherent mixture of spin-squeezed states with different orientations in the x - y -plane. Since this does not effect the spin length, the generalized spin-squeezing parameter is robust against this type of noise.

6. Multi-particle entanglement in a spinor Bose-Einstein condensate

In systems containing only a few, but individually addressable particles, entanglement is commonly confirmed by the full reconstruction of the underlying density matrix. In the case of ions [7], photons [118, 119], superconducting qubits [10, 11], nitrogen-vacancy centers in diamond [12] and many other well controllable systems, this so-called full state tomography [120] is a standard technique. However, the required number of measurements as well as the dimension of the density matrix scale exponentially with the number of particles. At about 40 particles, more than one terabyte is needed to store the density matrix on a computer. For about 20 particles, about one million measurements need to be performed and the calculation of the density matrix from the measurement results cannot be performed in a reasonable time. Obviously, such a tomography for our state describing up to 10 000 atoms is not feasible. Moreover, full state tomography requires the ability to manipulate the individual spins to enable measurements in different bases. This is not only a technical challenge, but fundamentally impossible for our system since the atoms in the BEC are indistinguishable.

Hence, we are limited to detect entanglement by measuring the components of the collective spin of the ensemble. Most prominently, this can be achieved by measuring a spin-squeezing parameter smaller than one (see Ref. 45, section 2.4 and appendix B).

$$\xi^2 = N \frac{(\Delta J_z)^2}{\langle J_x \rangle^2 + \langle J_y \rangle^2} < 1 \quad (6.1)$$

For states with an undefined orientation of the collective spin in the x - y -plane $\langle J_x \rangle = \langle J_y \rangle = 0$, this parameter is useless due to the vanishing denominator. In this case, even for $\Delta J_z = 0$ and a perfect detection the spin-squeezing parameter is at best $\xi = 1$ and no entanglement can be detected with the spin-squeezing criterion [111].

Simultaneous eigenstates of \mathbf{J}^2 and J_z are called Dicke states [121]. Even though they are not detected by the spin-squeezing criterion they are known to be highly entangled and useful for applications in quantum information such as open-destination teleportation and $1 \rightarrow (N - 1)$ telecloning [122]. They are optimal for metrology [112, 123–125] as has been demonstrated in the last chapter for the twin-Fock state which is a special Dicke state with $\langle J_z \rangle = 0$.

The concept of entanglement detection based on the measurement of the collective spin has been extended from spin-squeezed states to more general entangled states. In Ref. [126] a set of inequalities for separable states was introduced

$$\langle J_x^2 \rangle + \langle J_y^2 \rangle + \langle J_z^2 \rangle \leq J_{\max}(J_{\max} + 1) \quad (6.2)$$

$$(\Delta J_x)^2 + (\Delta J_y)^2 + (\Delta J_z)^2 \geq J_{\max} \quad (6.3)$$

$$\langle J_k^2 \rangle + \langle J_\ell^2 \rangle - J_{\max} \leq (N - 1)(\Delta J_m)^2 \quad (6.4)$$

$$(N - 1)[(\Delta J_k)^2 + (\Delta J_\ell)^2] \geq \langle J_m^2 \rangle + J_{\max}(J_{\max} - 1) \quad (6.5)$$

with $J_{\max} = \frac{N}{2}$. The indices k, ℓ and m take all possible permutations of x, y and z . A violation of any of these inequalities provides a proof of entanglement. Moreover, these equations are optimal in the sense that they detect all entangled states that can be detected based on the measurement of the mean value $\langle J_k \rangle$ and the fluctuations ΔJ_k .

at large numbers of particles. Only if higher moments ($\langle J_k^3 \rangle, \langle J_k^4 \rangle, \dots$) are considered as well, more entangled states may be detected by a measurement of the collective spin.

The first inequality states that the collective spin length is bound by J_{\max} and cannot be violated. The second inequality is maximally violated by the completely anti-symmetric state with $\mathbf{J}^2 = 0$ and can be used to detect entanglement in the vicinity of this highly entangled many-body singlet state. Combining Ineq. (6.3) and (6.4), we can regain the spin-squeezing condition (6.1). Moreover, it is possible to gain a generalized spin-squeezing parameter [127] from Ineq. (6.4)

$$\xi_{\text{gen}}^2 = (N - 1) \frac{(\Delta J_z)^2}{\langle J_{\text{eff}}^2 \rangle - J_{\max}}. \quad (6.6)$$

The entanglement condition $\xi_{\text{gen}} < 1$ is ideally suited to detect the entanglement close to Dicke states. It compares the sub-shot-noise fluctuations ΔJ_z with the effective spin length $J_{\text{eff}}^2 = J_x^2 + J_y^2$ in the x - y -plane. The effective spin length reaches its maximum $\langle J_{\text{eff}}^2 \rangle = J_{\max}(J_{\max} + 1) \approx J_{\max}^2$ for the ideal twin-Fock state. In the Bloch-sphere picture, it corresponds to the radius of the ring around the equator representing the twin-Fock state. We have seen in the last chapter that it is related to the contrast of the twin-Fock interferometer. A maximal spin length $\mathbf{J}^2 = J_{\max}(J_{\max} + 1)$ is achieved for pure spin states that are fully symmetric under particle exchange (see appendix A.1). For symmetric states, sub-shot-noise fluctuations directly imply full N -particle entanglement (see appendix A.2). In this sense, a large effective spin length tests the symmetry of the state and excludes the possibility that the sub-shot-noise fluctuations are caused by classical correlations as in the example of Fig. 2.9.

The generalized spin-squeezing parameter is also valuable for the detection of entanglement in the case of a spin-squeezed state. If the state is strongly polarized along one axis $\langle J_x \rangle \approx J_{\max}$, the effective spin length can be approximated

$$\langle J_{\text{eff}}^2 \rangle = \langle J_x^2 \rangle + \langle J_y^2 \rangle \approx \langle J_x \rangle^2 + \langle J_y \rangle^2 \quad (6.7)$$

and the two parameters become hence comparable $\xi \approx \xi_{\text{gen}}$ for a large number of particles. If the created state is a incoherent mixture of spin-squeezed states polarized in different directions in the x - y -plane as shown in Fig. 6.1b, the mean collective spin $\langle J_x \rangle^2 + \langle J_y \rangle^2$ will be reduced, while the effective spin length is unchanged. The generalized spin-squeezing parameter is thus robust against uncontrolled phase shifts and useful for the detection of entanglement of spin-squeezed states in the presence of phase noise.

As a first step, we will characterize the state created by spin-dynamics in terms of the generalized spin-squeezing parameter.

6.2. Spin dynamics in $F=1$

For the creation of twin-Fock states, we use spin dynamics in the $F = 1$ manifold of ^{87}Rb . Compared to spin dynamics in $F = 2$ described in section 5.3, this has the advantage of

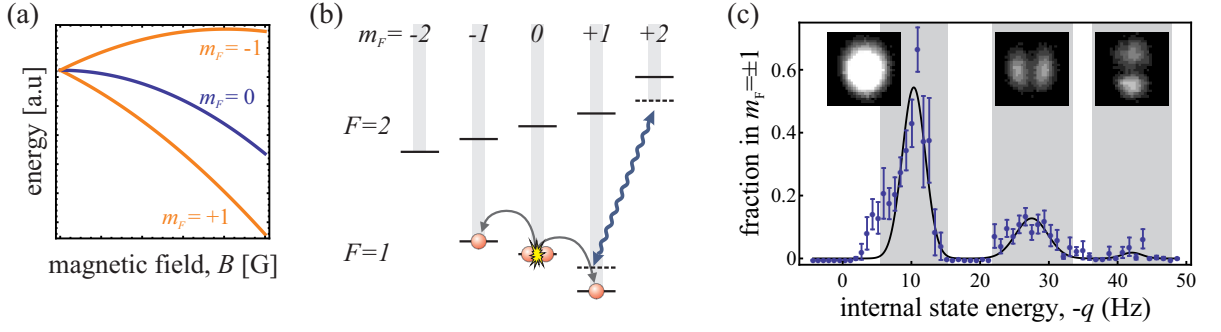


Figure 6.2.: **Spin dynamics in $F = 1$.** (a) Splitting of the Zeeman levels in $F = 1$ with a reduced linear contribution by a factor of 200 to make the quadratic contribution apparent. Due to the quadratic part, the internal energy of a pair of atoms increases during a spin-changing collision from $m_F = 0$ to $m_F = \pm 1$. (b) The internal energy of the $m_F = +1$ Zeeman level can be reduced by a dressing on the transition between $|F, m_F\rangle = |1, +1\rangle$ and $|2, +2\rangle$ with a red-detuned microwave. The change in the internal energy q can be tuned by adjusting the microwave detuning. (c) This enables us to observe well resolved spin dynamics resonances in $F = 1$ for an evolution time of 280 ms. The averaged density profiles reflect the shape of the eigenmodes of the effective potential seen by the atoms with $m_F = \pm 1$.

avoiding collisions changing the hyperfine state from $F = 2$ to $F = 1$ (see section 3.3), the strongest loss mechanism in $F = 2$. If a mean of $\langle N_{\text{loss}} \rangle$ particles is lost from a Fock state with an initially well defined number of particles N , we expect to observe fluctuations $\Delta N = \sqrt{\langle N_{\text{loss}} \rangle}$. Hence, any loss contributes to increased fluctuations in the population imbalance ΔJ_z . Besides the reduced losses during spin dynamics in $F = 1$, there are other technical and conceptional differences that we discuss in the following.

As mentioned in section 5.3, the quadratic contribution of the Zeeman shift in $F = 1$ has the opposite sign compared to $F = 2$. Consequently, the internal energy increases during a spin-changing collision from $m_F = 0$ to $m_F = \pm 1$. For typical densities in our experiments, even the energy of the ground state of the effective potential seen by the atoms in $m_F = \pm 1$ is above the energy of a particle in the $m_F = 0$ condensate. Hence, internal and external energy increase in case of a spin-changing collision. The energy conservation required for a spin dynamics resonance can thus not be fulfilled by tuning the magnetic field and a Bose-Einstein condensate in $m_F = 0$ is stable. To initiate spin dynamics, we manipulate the internal level structure with the help of microwave dressing as described in section 4.2. At a magnetic field of $B = 2.6$ G, we use a microwave which is red detuned to the $|F, m_f\rangle = |1, 1\rangle \rightarrow |2, 2\rangle$ transition to reduce the energy of the $|1, 1\rangle$ level. Thereby, the change of the internal energy q can be tuned by adjusting the microwave detuning. In the range of $\delta \in [-750, -650]$ kHz, we observe spin dynamics resonances as shown in Fig. 6.2c.

Compared to spin dynamics in $F = 2$ (see Fig. 5.2c), the resonances are well resolved and do not overlap although all experimental parameters are comparable. The reason is

the 7.7 times smaller matrix element U_1 in the interaction Hamiltonian describing the spin-changing collisions (see section 3.3). This leads to a reduced width $\Omega \propto N_0 U_1$ of the spin dynamics resonances.

On the other hand, this leads to a longer evolution time $t \sim \frac{1}{\Omega}$ for the transfer of a considerable fraction of atoms into the $m_F = \pm 1$ levels. For the following experiments we tune the microwave to the resonance of the first excited mode of the effective potential at $q \approx -28$ Hz and employ an evolution time of 240 ms.

6.3. Estimation of the generalized spin-squeezing parameter

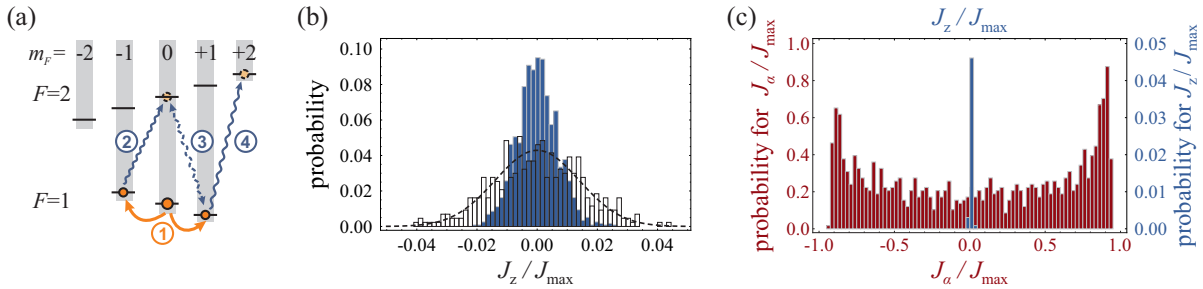


Figure 6.3.: **Measurement of the sub-shot-noise fluctuations and the effective spin length.** (a) After populating the $|F, m_F\rangle = |1, \pm 1\rangle$ levels with spin dynamics (1), we transfer the atoms from $|1, -1\rangle$ to $|2, 0\rangle$ with a microwave π pulse (2). This enables us to couple the level $|2, 0\rangle$ and $|1, +1\rangle$ with a $\frac{\pi}{2}$ -pulse and thereby turn the state on the generalized Bloch sphere (3). Finally, we transfer the atoms from $|1, +1\rangle$ to $|2, +2\rangle$ (4). This last step is necessary for the separation via a strong magnetic field gradient enabling the state-selective detection. (b) Without a coupling pulse (3), we measure the fluctuations in J_z . The resulting distribution (blue) in an interval $N \in [3000, 7000]$ is much narrower than the fluctuations of a coherent state (open bars) in the same interval which we prepare with a microwave $\frac{\pi}{2}$ -pulse. Ideally, the coherent state fluctuations are given by shot noise (dashed line). We corrected for a small offset between the center of the distributions. (c) With the $\frac{\pi}{2}$ coupling pulse, the measured distribution of the population imbalance (red bars) is much wider than the initial sub-shot-noise distribution (blue bars) indicating a large effective spin length J_{eff} .

For the estimation of the generalized spin-squeezing parameter, we have to measure the reduced fluctuations in the population imbalance ΔJ_z and the effective spin length in the x - y plane. The measurement of the population imbalance can be realized by counting the atoms in the two levels $|\uparrow\rangle$ and $|\downarrow\rangle$ and calculating the fluctuations of the difference $N_\uparrow - N_\downarrow$. For the measurement of $\langle J_{\text{eff}}^2 \rangle = \langle J_x^2 + J_y^2 \rangle$ we need to turn the state on the generalized Bloch sphere before the number measurement to resolve $\langle J_x^2 \rangle$ and

$\langle J_y^2 \rangle$ This can be realized by first transferring the atoms from $|F, m_F\rangle = |1, -1\rangle$ to $|2, 0\rangle$ with a microwave π -pulse and then coupling these atoms with the atoms in $|1, +1\rangle$ with a $\frac{\pi}{2}$ -pulse (see Fig.6.3a). Subsequently, we transfer the atoms from $|1, +1\rangle$ to $|2, +2\rangle$. This enables a state-selective estimation of the number of atoms by spatially separating the atoms in the different Zeeman states with a strong magnetic field gradient (see section 4.4.3).

If we measure J_x or J_y after the coupling pulse depends on the phase difference between the initial Bose-Einstein condensate and the microwave. For a given phase difference α , the number measurement after the coupling pulse correspond to a projection on $J_\alpha = \cos(\alpha)J_x + \sin(\alpha)J_y$. Intrinsically, the two phases are completely uncorrelated. Hence, we have to average over all possible phase differences α to calculate the expectation value corresponding to our measurements. For the recorded second moment, this corresponds to a measurement of the effective spin length J_{eff} .

$$\frac{1}{2\pi} \int_0^{2\pi} \langle J_\alpha^2 \rangle d\alpha = \left\langle \frac{1}{2}(J_x^2 + J_y^2) \right\rangle = \frac{1}{2} \langle J_{\text{eff}}^2 \rangle \quad (6.8)$$

We also need to know the error of the second moment measurement without assumptions on the form of the underlying distribution. The statistically correct estimation of this error is presented in appendix E. We use the same transfer pulses for the measurement of ΔJ_z , such that we can directly compare the sub-shot-noise fluctuations of the population imbalance with the large fluctuations expected for the measurement of J_{eff} (see Fig.6.3c).

Since we are interested in the pure atomic noise ΔJ_z , we subtract the independently measured detection noise that is independent of the number of atoms (see section 4.4.5). We measure a number squeezing of up to -12.4 ± 1.2 dB at a total number of 8 000 atoms. The fluctuations ΔJ_z are almost independent on the total number of atoms. A small trend of $\Delta J_z \sim 0.15 \sqrt{N}$ could be due to losses as explained in the last section. However, we do not observe significantly increased fluctuations for an additional hold time of up to 420 ms after spin dynamics, which excludes losses as a major noise source. Other noise sources that should increase with an additional holding time like residual radio frequencies can also be excluded. The trend has to be explained by noise in the transfer pulses and additional number dependent detection noise. Hence, our results are limited by our detection capabilities and not by the fluctuations of the prepared state.

The measured effective spin length $\langle J_{\text{eff}} \rangle$ is close to the optimal achievable value of J_{max} as shown in Fig.6.4b. It slowly decreases during an additional hold time. We thus conclude that a magnetic field gradient and elastic collisions are limiting the achievable spin length. elastic collisions can lead to a spontaneous change of the spatial wave function of an atom. Thereby, it becomes distinguishable by its spatial degree of freedom. This may lead to a spin state that is not completely symmetric with respect to particle exchange.

Both measurements can be combined to estimate a generalized spin-squeezing parameter as presented in Fig.6.4c. At a total number of 8 000 atoms, we achieve a generalized spin-squeezing parameter of $-11.4(5)$ dB [34]. It is reasonable to compare the new generalized parameter ξ_{gen} to the usual spin-squeezing parameter ξ as explained in

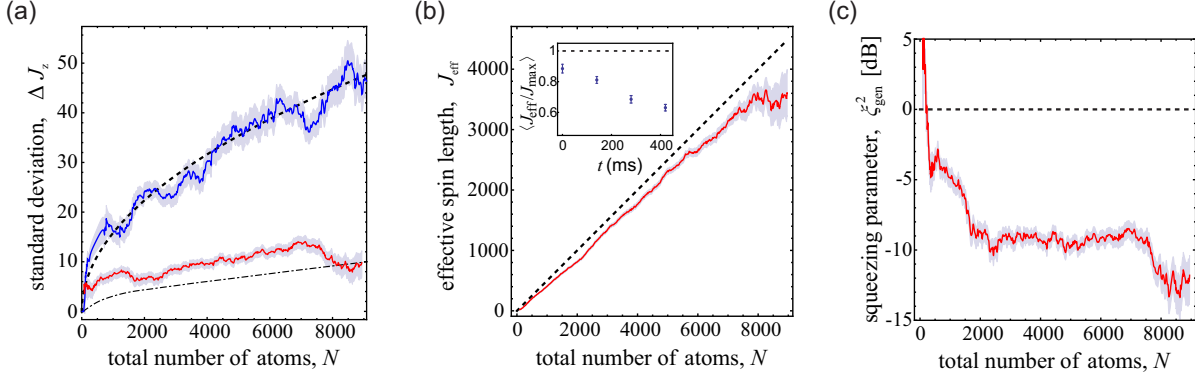


Figure 6.4.: **Generalized spin-squeezing parameter.** (a) The fluctuations of the population imbalance (red solid line) are well below shot noise (black dashed line). The independently measured detection noise has been subtracted to estimate the pure atomic noise. In the interval from $N = 7500$ to 8500 atoms, we reach a number squeezing of -12.4 ± 1.2 dB. The slightly increased fluctuations at larger numbers of atoms can be explained by a number dependent detection noise which can be estimated as explained in sec. 4.4.6 (black dash-dotted line). To confirm the calibration of the absolute number of atoms, we measure the shot-noise fluctuations of a coherent state created by a microwave $\pi/2$ -pulse (blue solid line). (b) The measured effective spin length J_{eff} (red line) almost reaches its maximally achievable value $J_{\text{max}} = N/2$ (dashed black line). If we introduce an additional hold time after spin dynamics, it slowly decreases as shown in the inset. (c) From these measurements, we can extract a generalized spin-squeezing parameter ξ_{gen} (red solid line). At a total number of 8000 atoms, we achieve a generalized spin squeezing of $11.4(5)$ dB. For all graphs, the individual data points are obtained from a post selected ensemble with a total number of atoms $N \in [x - 500, x + 500]$. The shaded areas correspond to a statistical uncertainty of one standard deviation.

section 6.1. Such a comparison shows that this measurement presents the highest spin squeezing measured in any atomic system to date.

6.4. Detection of multi-particle entanglement in spin-squeezed ensembles

In the last section, we have seen that we are able to detect the entanglement of the Dicke-like state created by spin dynamics with a generalized spin-squeezing parameter. Since the system contains up to 10 000 atoms, it might exhibit multi-particle entanglement and not only pairwise entanglement. Such multi-particle entanglement is best characterized by the entanglement depth [63] which is defined as the number of particles in the largest

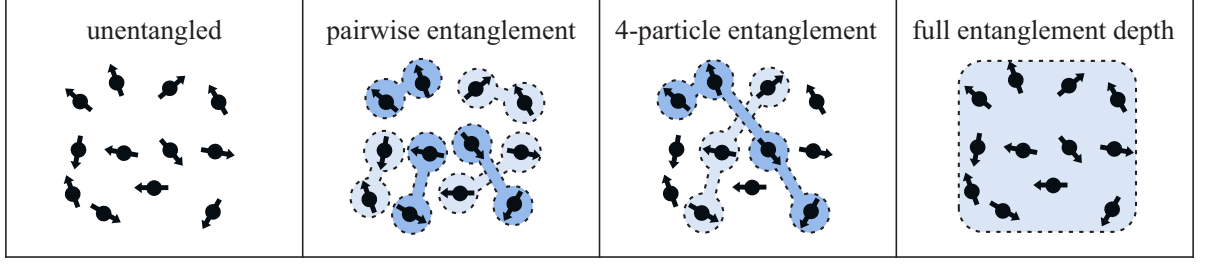


Figure 6.5.: **Multi-particle entanglement in an ensemble.** An ensemble of $N > 2$ particles may contain more than pairwise entanglement. The multi-particle entanglement is best characterized by the entanglement depth k defined as the number of particles in the largest non-separable subset. In the above examples, the entanglement depth ranges from $k = 1$ for the separable state over $k = 2$ for the pairwise entangled state to $k = 4$ for larger entangled subsets and finally to $k = N$ for full entanglement of the ensemble. Entanglement is indicated by the blue shaded areas connecting the individual spin- $\frac{1}{2}$ particles.

non-separable subset of a state (see Fig. 6.5).

In their seminal work, Sørensen and Mølmer described a method to detect multi-particle entanglement of spin-squeezed states by a measurement of the collective spin \mathbf{J} . In the following, we will briefly describe their method, which will be extended for the application to more general states and for a improved noise tolerance in the next section.

The starting point of the method by Sørensen and Mølmer is a numerical determination of pure states with minimal achievable fluctuations in the population imbalance ΔJ_z for a given mean spin component $\langle J_y \rangle$. For a single spin- $\frac{1}{2}$ particle with $\langle J_x \rangle = 0$, the component $\langle J_y \rangle$ determines the turning angle θ on the Bloch sphere. For $\theta = 0$, the state is located on the top of the Bloch sphere and we get $\langle J_y \rangle = 0$ and vanishing fluctuations in ΔJ_z . By increasing the turning angle θ , the projection $\langle J_y \rangle$ becomes larger and finally $\langle J_y \rangle = J$ for $\theta = \frac{\pi}{2}$. At this point, the fluctuations ΔJ_z are maximal since the state corresponds to a 50/50 superposition of $|\uparrow\rangle$ and $|\downarrow\rangle$.

If we investigate a system with a larger collective spin J , we can do more than just turning the state on the Bloch sphere to minimize the fluctuations ΔJ_z : We can entangle the individual spins \mathbf{s} that add up to the collective spin J and thereby squeeze these fluctuations. With an increasing number of particles, we can achieve larger multi-particle entanglement and more efficient squeezing in the following sense: We compare the normalized minimal achievable fluctuations $\frac{(\Delta J_z)^2}{J} = F_J(\frac{\langle J_y \rangle}{J})$ for a given normalized mean spin component $\frac{\langle J_y \rangle}{J}$. From a constraint optimization, the minimal fluctuations $F_J(\frac{\langle J_y \rangle}{J})$ can be calculated numerically and are shown in fig 6.6a. We find that $F_J(\frac{\langle J_y \rangle}{J}) < F_{J'}(\frac{\langle J_y \rangle}{J'})$ for $J > J'$.

Since these functions $F_J(\frac{\langle J_y \rangle}{J})$ are convex, a mixture of spin- J states can only have increased fluctuations. As a simple example, consider a mixture, where the spin- J state

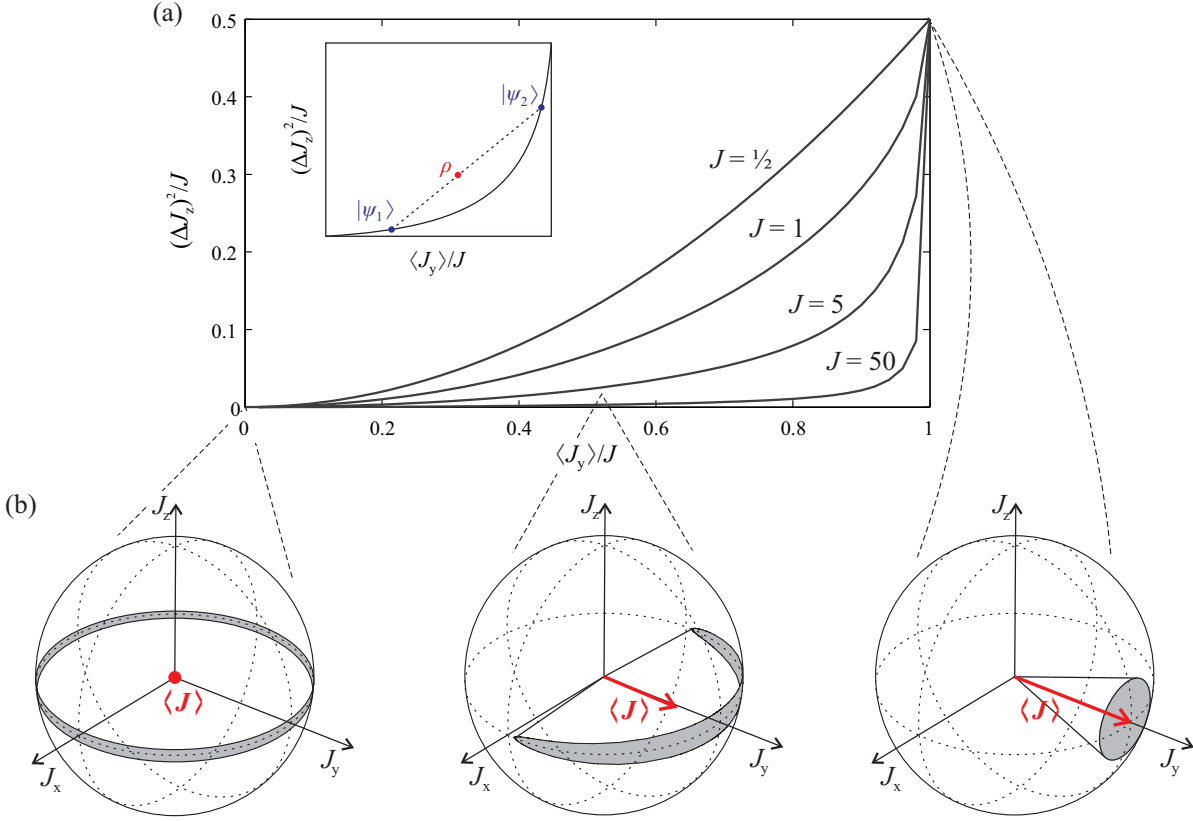


Figure 6.6.: **Relation between the length of the mean collective spin and sub-shot-noise fluctuations.** (a) Sørensen and Mølmer calculated minimal achievable fluctuations in the normalized population imbalance $\frac{(\Delta J_z)^2}{J} = F_J(\frac{\langle J_y \rangle}{J})$ as a function of the mean spin $\langle J_y \rangle$ for different spin lengths $J^2 = J(J+1)$ assuming pure states. Due to the convexity of these curves $F_J(\frac{\langle J_y \rangle}{J})$, any mixture of states with the same spin length J must exhibit increased fluctuations compared to these minimal achievable fluctuations as shown for a simple example in the inset. (b) For a fully polarized spin coherent state with $\langle J_y \rangle = J$ shown on the right, these fluctuations are given by shot noise $\frac{(\Delta J_z)^2}{J} = \frac{1}{2}$. For a spin-squeezed state shown in the middle, these fluctuations can be reduced at the expense of increased fluctuations in the phase difference. These phase fluctuations limit the achievable mean collective spin $\frac{\langle J_y \rangle}{J}$ in y direction. Finally, on the left side, we show a Dicke state with vanishing fluctuations in the population $\frac{(\Delta J_z)^2}{J} = 0$ and a vanishing mean collective spin $\frac{\langle J_y \rangle}{J} = 0$.

$|\psi_1\rangle$ is produced with a probability p_1 and the state $|\psi_2\rangle$ otherwise.

$$\rho = p_1 |\psi_1\rangle \langle \psi_1| + (1 - p_1) |\psi_2\rangle \langle \psi_2| \quad (6.9)$$

6. Multi-particle entanglement in a spinor Bose-Einstein condensate

The corresponding mean spin component $\frac{\langle J_y \rangle}{J}$

$$\frac{\langle J_y \rangle}{J} = p_1 \left\langle \frac{\langle J_y \rangle}{J} \right\rangle_1 + (1 - p_1) \left\langle \frac{\langle J_y \rangle}{J} \right\rangle_2 \quad (6.10)$$

and the fluctuations

$$\frac{(\Delta J_z)^2}{J} = p_1 \left\langle \frac{(\Delta J_z)^2}{J} \right\rangle_1 + (1 - p_1) \left\langle \frac{(\Delta J_z)^2}{J} \right\rangle_2 \quad (6.11)$$

describe points on a straight line *above* the curve $F_J(\frac{\langle J_y \rangle}{J})$ as shown in the inset of Fig. 6.6a. Here, $\langle \cdot \rangle_i$ denotes the expectation value corresponding to state i . Hence, the fluctuations are increased compared to the optimal spin- J state with the same mean spin component.

An ensemble of N particles may have several entangled subsets. If such a subset contains k spin- $\frac{1}{2}$ particles, its spin length is $j \leq \frac{k}{2}$. We assume for simplicity that N is a multiple of k . We can see from the above discussion that the fluctuations $(\Delta J_z)^2$ with a given $\frac{\langle J_y \rangle}{J}$ for an N particle state are minimized if the following conditions are met: Every non-separable subset of the full N -particle state has the maximal size k . These subsets are all in the same symmetric state $|\psi\rangle$ with $j^{(i)} = \frac{k}{2}$. This state minimizes the fluctuations $\frac{\Delta j_z^{(i)}}{j^{(i)}}$ for a mean spin component $\langle j_y^{(i)} \rangle = \frac{\langle J_y \rangle}{(\frac{N}{k})}$. The full N -particle state can be written as

$$|\Psi\rangle = |\psi\rangle^{\otimes \frac{N}{k}} \quad (6.12)$$

and its fluctuations in the population imbalance are given by the sum of the fluctuations of the non-separable subsets.

$$(\Delta J_z)^2 = \sum_{i=1}^{\frac{N}{k}} (\Delta j_z^{(i)})^2 = \sum_{i=1}^{\frac{N}{k}} j^{(i)} F_{j^{(i)}} \left(\frac{\langle J_y \rangle}{(\frac{N}{k}) j^{(i)}} \right) = \frac{N}{2} F_{\frac{k}{2}} \left(\frac{2 \langle J_y \rangle}{N} \right) \quad (6.13)$$

Hence, any state with the same mean spin component $\langle J_y \rangle$, but smaller fluctuations $(\Delta J_z)^2$, has to contain a non-separable subset of more than k particles. This means that it has at least an entanglement depth of $k + 1$.

So far, we have assumed that the state is oriented along the y -axis. However, the above discussion can be repeated for an arbitrary orientation of the mean collective spin in the x - y -plane. Hence, a more general form of the criterion can be formulated by using the length of the mean collective spin $\sqrt{\langle J_x \rangle^2 + \langle J_y \rangle^2}$ in the x - y plane.

$$(\Delta J_z)^2 \geq J_{\max} F_{\frac{k}{2}} \left(\frac{\sqrt{\langle J_x \rangle^2 + \langle J_y \rangle^2}}{J_{\max}} \right). \quad (6.14)$$

In summary, a measurement of sub-shot-noise fluctuations ΔJ_z and a large mean spin component $\langle J_y \rangle$ that violates the inequality (6.14) for a given k proves an entanglement

depth larger than $k+1$. Obviously, the inequalities (6.14) are increasingly rigid for larger k .

This criterion has been used in the group of M. Oberthaler in Heidelberg to proof an entanglement depth larger than 80 with a 3 standard deviations uncertainty level [13]. This, is the largest multi-particle entanglement that has been reported (see Fig. 6.8b).

6.5. A new criterion for multi-particle entanglement

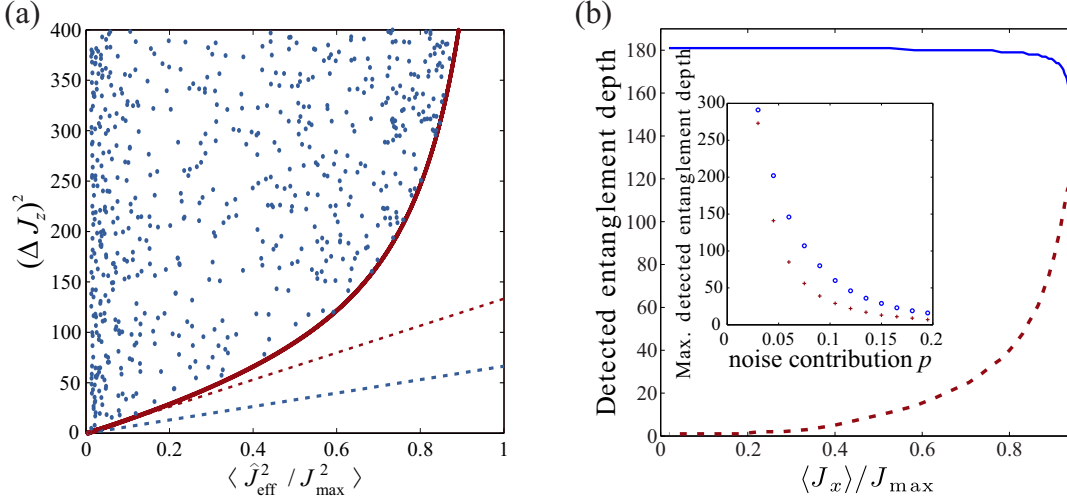


Figure 6.7.: **The new criterion for multi-particle entanglement.** (a) The red curve is the boundary of Eq. (6.20) for states with an entanglement depth not larger than $k = 28$ and a total number of $N = 8\,000$ atoms. Every state below this boundary contains at least 28-particle entanglement. As a cross check, the area above the boundary is filled up with points corresponding to random states with an entanglement depth of $k = 28$. From a tangent to the boundary we can gain a linear criterion (red dashed line) which detects more k -particle entangled states than the analytically derived criterion by Duan [128]. (b) The graphs show the entanglement depth detected by the new criterion (blue line) and the Sørensen-Mølmer criterion (red dashed line) for 4 000 spin- $\frac{1}{2}$ particles in a spin-squeezed state and a small noise contribution to account for imperfections. In this case the new criterion is superior even for a large mean spin component $\langle J_x \rangle$. The inset shows the maximally detected entanglement depth for any $\langle J_x \rangle$ as a function of the noise contribution. The blue dots correspond to the new criterion and the red crosses to the Sørensen-Mølmer criterion.

Just like in the case of the spin-squeezing parameter, the Sørensen-Mølmer criterion for multi-particle entanglement cannot be used for Dicke-like states since it relies on the detection of a large mean spin component $\langle J_y \rangle$ which is zero in the case of a Dicke state

6. Multi-particle entanglement in a spinor Bose-Einstein condensate

(see Fig. 6.6b). As we have seen in section 6.1, in the case of entanglement detection, this problem can be solved by introducing the generalized spin-squeezing parameter, which compares the sub-shot-noise fluctuations with the effective spin length in the x - y -plane $\langle J_{\text{eff}}^2 \rangle = \langle J_x^2 \rangle + \langle J_y^2 \rangle$ instead. They were able to extend this concept to the detection of multi-particle entanglement as we will briefly describe in the following.

Let us assume that we have a pure state with an entanglement depth of k . This can be written as

$$|\Psi\rangle = |\psi^{(1)}\rangle \otimes |\psi^{(2)}\rangle \otimes \dots \otimes |\psi^{(M)}\rangle \quad (6.15)$$

where M is the number of non-separable subsets described by the states $|\psi^{(i)}\rangle$. Each of these subsets has a spin $\mathbf{j}^{(i)}$ with a length of $j \leq \frac{k}{2}$. With these spin operators for the individual subsets, we can write the effective spin length as

$$\begin{aligned} \langle J_{\text{eff}}^2 \rangle &= \langle J_x^2 + J_y^2 \rangle = \sum_{m,\ell} \langle j_x^{(m)} j_x^{(\ell)} + j_y^{(m)} j_y^{(\ell)} \rangle \\ &= \sum_{m=\ell} \langle (j_x^{(m)})^2 + (j_y^{(m)})^2 \rangle + \sum_{m \neq \ell} (\langle j_x^{(m)} \rangle \langle j_x^{(\ell)} \rangle + \langle j_y^{(m)} \rangle \langle j_y^{(\ell)} \rangle) \\ &\leq \sum_m \langle (j_x^{(m)})^2 + (j_y^{(m)})^2 \rangle + \sum_{m,\ell} (\langle j_x^{(m)} \rangle \langle j_x^{(\ell)} \rangle + \langle j_y^{(m)} \rangle \langle j_y^{(\ell)} \rangle) \\ &= \sum_m \langle (j_x^{(m)})^2 + (j_y^{(m)})^2 \rangle + \langle J_x^{(m)} \rangle^2 + \langle J_y^{(m)} \rangle^2 \end{aligned} \quad (6.16)$$

Since the spin length of the individual subsets is $j \leq \frac{k}{2}$, we have

$$(j_x^{(m)})^2 + (j_y^{(m)})^2 \leq \frac{k}{2} \left(\frac{k}{2} + 1 \right) \quad (6.17)$$

and get

$$\langle J_{\text{eff}}^2 \rangle \leq M \frac{k}{2} \left(\frac{k}{2} + 1 \right) + \langle J_x \rangle^2 + \langle J_y \rangle^2. \quad (6.18)$$

With $M \geq \frac{N}{k}$, we finally gain an expression

$$\langle J_{\text{eff}}^2 \rangle - J_{\text{max}} \left(\frac{k}{2} + 1 \right) \leq \langle J_x \rangle^2 + \langle J_y \rangle^2 \quad (6.19)$$

that is useful to replace the length of the mean collective spin by the effective spin length in the original Sørensen-Mølmer criterion (6.14). Using the monotony of $F_j(x)$ and Eq. (6.14) we arrive at

$$(\Delta J_z)^2 \geq J_{\text{max}} F_{\frac{k}{2}} \left(\frac{\sqrt{\langle J_{\text{eff}}^2 \rangle - J_{\text{max}} \left(\frac{k}{2} + 1 \right)}}{J_{\text{max}}} \right). \quad (6.20)$$

The right hand side of the inequality is a convex function of the effective spin length and the inequality thus holds for mixed states with an entanglement depth of k .

A measurement result violating this inequality proves that the underlying state has an entanglement depth larger than k . With this method we can prove multi-particle entanglement beyond spin squeezing in the state created by spin dynamics as we will see in the next section.

A numerical test indicates that the new criterion is optimal in the sense that there is no criterion detecting a larger entanglement depth based on a measurement of J_{eff} and ΔJ_z (see Fig. 6.7a). Furthermore, the new criterion is not only useful for the detection of Dicke states but also detects a larger entanglement depth for spin-squeezed states in the presence of noise [34]. This is shown in Fig. 6.7b, where we plot a comparison of the entanglement depths detected by the two criteria applied to squeezed states with a small noise contribution. The noise was modelled as independently fluctuating particles in a statistical mixture of the state $|\uparrow\rangle$ and $|\downarrow\rangle$. This is described by the density matrix

$$\rho_n = \rho_{\text{mix}}^{\otimes N} \quad \text{with} \quad \rho_{\text{mix}} = 0.5 |\uparrow\rangle \langle\uparrow| + 0.5 |\downarrow\rangle \langle\downarrow|. \quad (6.21)$$

The final result is fairly independent of the exact type of the noise. The full state ρ was obtained from mixing this maximally noisy state ρ_n with the ideal spin-squeezed state ρ_{id} .

$$\rho = (1 - p)\rho_{\text{id}} + p\rho_n \quad (6.22)$$

For the results shown in Fig. 6.7b, a noise contribution of $p = 0.05$ was used. The robustness of the new criterion in the presence of phase noise can be understood in the same way as the robustness of the generalized spin-squeezing parameter which is illustrated in Fig. 6.1b. This noise tolerance makes the new criteria very valuable for the experimental application.

6.6. Characterization of the multi-particle entanglement

In a "bottom-up" approach, research groups worldwide try to entangle larger and larger groups of individually addressable particles (see chapter 1). The best result has been reported by the group of R. Blatt, achieving full multi-particle entanglement of 14 ions. Ensembles of neutral atoms provide a "top-down" approach for the creation of large entangled ensembles. This was demonstrated in the group of M. Oberthaler by the creation of spin-squeezed ensembles of about 400 neutral atoms with an entanglement depth of 170 atoms.

With the new criterion at hand, we can use the measurement of the sub-shot-noise fluctuations ΔJ_z and of the effective spin length J_{eff} presented in section 6.3 to estimate the entanglement depth of the created state. The result of such an estimation for all realizations with a total number of atoms between 7500 and 8500 is shown in Fig. 6.8a. With a two standard deviation uncertainty level the created state contains more than 28 particle entanglement. The mean values of the measurements indicate an entanglement depth of 68.

This is the first demonstration of multi-particle entanglement of neutral atoms in a state beyond spin-squeezed states - the Dicke states. The comparably large number

6. Multi-particle entanglement in a spinor Bose-Einstein condensate

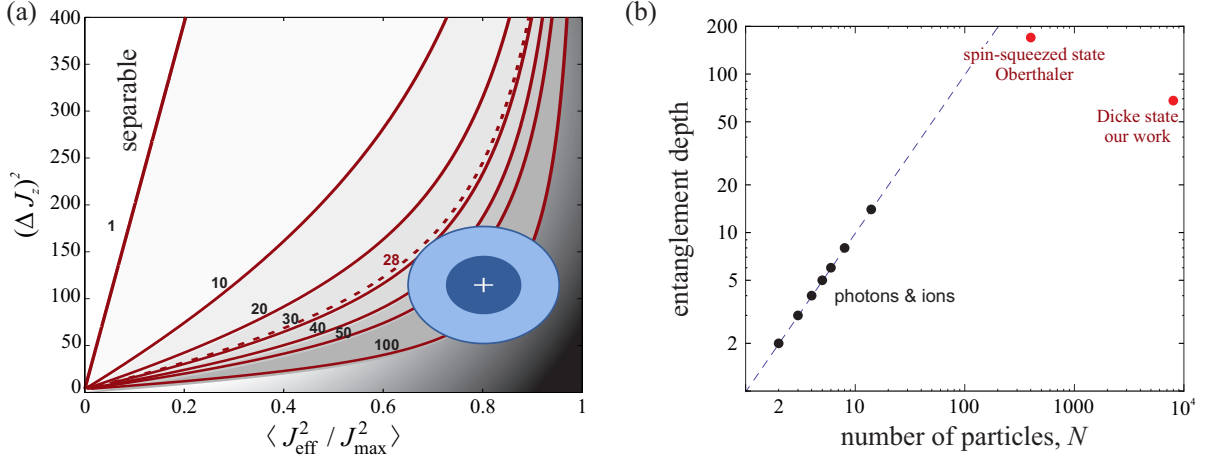


Figure 6.8.: **Experimentally generated multi-particle entanglement.** (a) The red curves correspond to the newly derived boundaries for k -particle entanglement (6.20) for $N = 8000$ atoms. Our measurements of the sub-shot-noise fluctuations ΔJ_z and the effective spin length J_{eff} are shown with one (dark blue) and two standard deviation (light blue) uncertainty ellipses. They are below the boundary for 28-particle entanglement (red dashed line) proving an entanglement depth larger than 28 with a two standard deviation uncertainty level. The mean values of our measurement indicate 68-particle entanglement. (b) As detailed in the introduction of this thesis, multi-particle entanglement of up to 14 particles [3] has been achieved in systems which are well-controllable on the single-particle level. An entanglement depth of 170 atoms has been achieved in an ensemble of about 400 spin-squeezed neutral atoms in the group of M. Oberthaler [13]. In this work, we achieved an entanglement depth of 68 atoms in a new class of states: the Dicke states. This multi-particle entanglement has been created in an ensemble of 8000 neutral atoms. The large number of atoms is important to achieve ultra-high precision in interferometry in realistic applications.

of 8000 particles in the ensemble shows, that large entangled ensembles for realistic applications in metrology can be created with our method. This may lead to a further improvement of the ultra-high precision of sensors based on atom interferometry.

7. Outlook

We have seen that spin dynamics can be used to create a multi-particle entangled state which can be used for precision measurements beyond the shot-noise limit. In the first section, we will show how these results can be improved in the future by reducing the detection noise. In the second section, we present a new type of interferometer for quantum-enhanced sensitivities at large numbers of atoms, which can be implemented using spin dynamics.

7.1. Improving the detection system

The main limitation of the results presented in chapter 5 and 6 are due to detection noise. There is strong evidence that the entanglement depth is limited by a number dependent detection noise. With our new detection system, the results of chapter 5 could already be improved to a phase sensitivity -8 dB below the shot-noise limit. This shows, that the precise counting of the number of atoms in the entangled states is a key requirement for our measurements. Hence, we will discuss possible improvements of the atom detection in this section.

7.1.1. Precision limits of absorption detection

As we have seen in section 4.4.4, the detection noise of absorption imaging can potentially be improved by reducing the area occupied by the atoms. One way to achieve such a compression of the atomic cloud is to use the so-called delta-kick cooling [105, 106]. We implement this technique by first releasing the atoms from the dipole trap. After 1 ms of free expansion, the dipole trap is abruptly switched on again. This stops a further expansion of the cloud while the different Zeeman components split up due to a strong magnetic field gradient. We were able to reduce the cloud radius from $25\text{ }\mu\text{m}$ to $10\text{ }\mu\text{m}$. As shown in Fig. 7.2a, this potentially reduces the photo-electron shot noise from $\Delta N_{\text{est}} \approx 10$ to 4 atoms for our imaging parameters. This corresponds to a noise of 5.7 in terms of the population imbalance J_z .

However, the nonlinearity in the estimation of the number of atoms has to be treated with care. As the diameter of the atomic cloud becomes smaller the impact of the blurring effects described in section 4.4.3 increases and leads to a strong nonlinearity. The number of atoms in a cloud with a radius of $10\text{ }\mu\text{m}$ is underestimated by almost 20% for a resolution $\sigma_B = 5\text{ }\mu\text{m}$ of the imaging system and a total of 5 000 atoms. The fluctuations of the number of atoms are even underestimated by 50% at this point. It is difficult to reduce this nonlinearity without increasing the detection noise simultaneously.

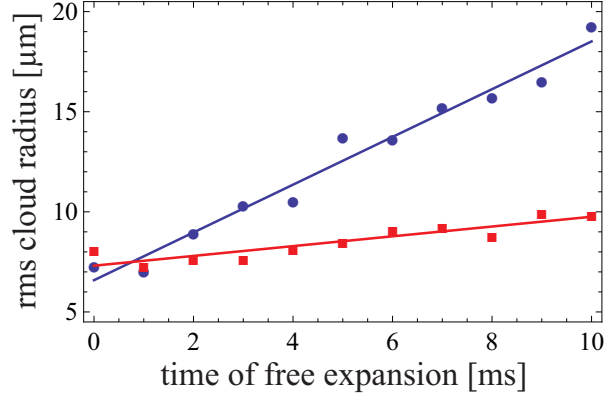


Figure 7.1.: **Reduction of the cloud radius by a delta kick.** The reduced kinetic energy after a delta kick leads to a slow expansion (red squares) compared to the usual expansion (blue dots) of the atomic cloud after releasing the atoms from the dipole trap. This leads to a small root mean square (rms) radius of the cloud after a free expansion time that is necessary to separate the different spin components via a strong magnetic field gradient. Linear fits are provided as guide to the eye (solid lines). We estimate that the cloud radius can be reduced from a rms radius of about $25\,\mu\text{m}$ to $10\,\mu\text{m}$ for our current trap frequencies, densities and expansion times that have changed slightly compared to the measurement shown here.

We could try to improve the optical resolution. However, as we have seen in section 4.4.3, the resolution is limited by the illumination time to $\sigma_B = 5\,\mu\text{m}$. A shorter illumination time would allow for a further improvement of the imaging resolution, but leads to an increased detection noise. The nonlinearity can also be reduced by increasing the intensity of the imaging beam. Unfortunately, this leads again to an increased detection noise.

Nonetheless, a moderate reduction of the root mean square (rms) cloud radius to $15\,\mu\text{m}$ leads only to a slightly increased nonlinearity. According to our simulation, the number of atoms is underestimated by 2.5% and the fluctuations are underestimated by less than 7% for this cloud size. If this effect is measured carefully, it is possible to correct the recorded numbers accordingly. Thereby, the photo-electron shot noise can be reduced to $\delta N_{\text{est}} \approx 7$ atoms.

For a smaller number of atoms, the constraints set by the nonlinearity are less rigid and an improved detection noise can be obtained by using very small clouds as demonstrated in the group of M. Oberthaler [97].

In summary, for a realistic imaging resolution the absorption detection of atomic clouds containing 5 000 atoms is limited to a detection noise on the order of $\Delta N_{\text{est}} \approx 7$ corresponding to a noise of 5 atoms in terms of J_z . It is thus worthwhile to look for new detection schemes for a further improvement.

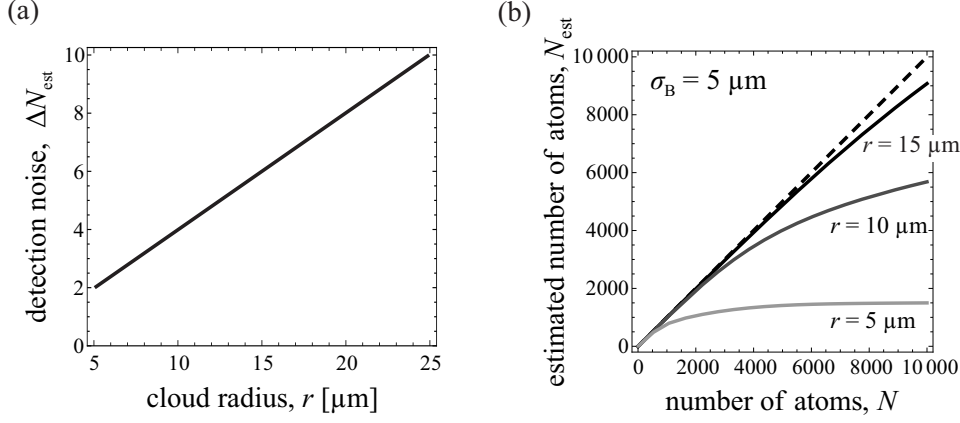


Figure 7.2.: **Detection noise and nonlinearity for different cloud sizes.** (a) The detection noise due to photo-electron shot noise at $N = 0$ decreases linearly with the cloud radius if all other imaging parameters stay fixed. (b) However, the nonlinearity due to blurring effects has a larger effect for smaller clouds. For an imaging resolution $\sigma_B = 5 \mu\text{m}$, the cloud size could be reduced to a rms radius of $15 \mu\text{m}$ without suffering too strong from the nonlinearity at 5 000 atoms in a single cloud. Provided that the illumination time and other imaging parameters can be left unchanged, this would lead to a photo-electron shot noise of $\Delta N_{\text{est}} \approx 7$ atoms. For ensembles containing less atoms, the restrictions by the nonlinearity are relaxed and the detection noise can be further reduced by compressing the atomic cloud.

7.1.2. Fluorescence detection

A new promising technique is to transfer the atoms in a MOT and use the fluorescence signal for the estimation of the number of atoms as demonstrated in Ref. [98]. For small ensembles of about $N = 100$ atoms, steps in the fluorescence signal corresponding to single atoms can be resolved. These discrete steps can only be observed for $\Delta N_{\text{est}} \ll 1$. For an ensemble of $N = 100$ atoms, $\Delta N_{\text{est}} = 0.14$ was measured, and for $N = 1080$, the detection noise is on the order of a single atom $\Delta N_{\text{est}} = 1$. If we extrapolate the data of Ref. [98] to $N = 5000$ atoms, we calculate a detection noise of $\Delta N_{\text{est}} = 3.9$ which would be a significant improvement compared to our current absorption detection setup. The optimal illumination time of 100 ms yields a detection of 9 031 photons per atom. The photon shot noise becomes small compared to other effects at such a large number of photons. Besides the atomic shot noise, which is mainly caused by one-body losses, fluorescence noise is the dominant limitation to this detection scheme as shown in Fig. 7.3. It is most probably caused by small deviations of the laser detuning due to its finite line width on the order of 100 kHz.

The main drawback of this detection technique is that the population of different internal states cannot be measured within a single realization. However, this is crucial for our main objective: the measurement of sub-shot-noise fluctuations. In order to overcome this limitation, atoms with internal states have to be trapped in different

7. Outlook

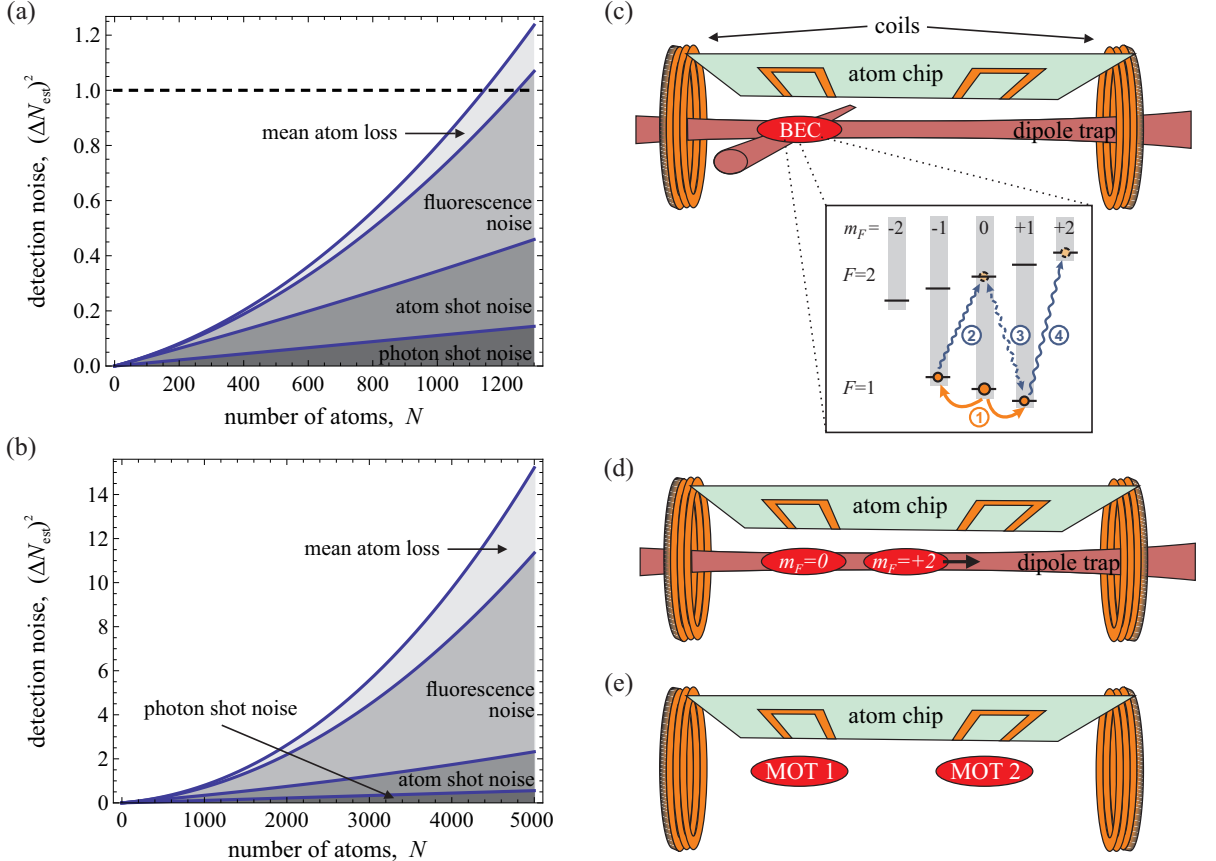


Figure 7.3.: **Fluorescence detection in a MOT.** (a) For a fluorescence detection in a MOT with parameters found in Ref. [98], different noise contributions add up to the detection noise as presented in this figure. (b) These noise contributions can be extrapolated to larger numbers of atoms. This yields a detection noise of $\Delta N_{\text{est}} = 3.9$ at $N = 5000$ atoms. (c) Schematic drawing of a possible setup for the generation and detection of entangled ensembles using the MOT fluorescence technique. With two coils and a U-shaped wire on an atom chip a quadrupole magnetic field for a MOT can be created. These atoms from the initial MOT are transferred into a magnetic trap and cooled until a BEC is formed. This has to be transferred into a crossed-beam dipole trap for spin dynamics (1). The inset shows the pulse sequence as discussed in section 6.3 which transfers the entangled atoms into the states $|F, m_F\rangle = |2, 0\rangle$ and $|2, +2\rangle$ (pulses (2) and (4)) and couples them if needed (pulse (3)). (d) With a strong magnetic field gradient, the atoms in $|2, +2\rangle$ can be pushed towards a second U-shaped wire on the atom chip providing a quadrupole field for a second MOT while the atom in $|2, 0\rangle$ stay in place. (e) The atoms are recaptured in the two MOTs and their fluorescence can be used to estimate the number of atoms in both states.

MOTs. This could be achieved by splitting the MOT in two parts with a far blue detuned light sheet. After separating the different Zeeman components with a strong magnetic field gradient, the atoms can be recaptured in the MOT on either side of the light sheet. However, at realistic optical powers in the light sheet, atoms will hop from one side to the other and cause an increased noise.

A different approach is to create two MOTs by generating two quadrupole fields close to each other. If they are separated by a few millimetres only, the atoms could be moved to the center of the traps with a strong magnetic field gradient and then recaptured. Additionally, a delta-kick could reduce the width of the atomic clouds for an efficient retrapping in the MOTs. The generation of the two quadrupole fields at small distances can be achieved by using an atom chip [129] as schematically shown in Fig. 7.3c.

Such a dual-MOT detection scheme involves several technical challenges. First, the atoms need to be transferred in either of the MOTs depending on their internal state with very low losses. Due to the large magnetic field gradients generated by an atom chip, the densities within the MOTs might be larger compared to the proof of principle experiment of Ref. 98. This leads to higher densities and larger collision rates. Thereby, the atomic shot-noise can be increased. Scattering of light at the chip surface can increase the background noise level. On the other hand, the major noise source, the fluorescence noise, is common to both MOTs and is thus suppressed in the estimation of the population imbalance J_z .

With this fluorescence detection setup, the detection noise would be reduced to 1.8 in terms of the population imbalance J_z . As shown in Fig. 5.6a, this allows for a phase sensitivity more than -20 dB below shot noise. Moreover, at small numbers of atoms, effects on the single particle level like the odd-even oscillation shown in Fig. 5.6b may become visible.

7.2. The Fock interferometer

In a recent publication L. Pezzé and A. Smerzi introduced a new technique to achieve sub-shot-noise phase sensitivity [130]. They considered an arbitrary state ρ_\uparrow at one input port of the interferometer with a mean number of atoms $\langle n_\uparrow \rangle$ and a Fock-state $|n_\downarrow\rangle$ at the other input port.

$$\rho = \rho_\uparrow \otimes |n_\downarrow\rangle \langle n_\downarrow| \quad (7.1)$$

The quantum Fisher information of this state is found to be $F_Q = 2n_\downarrow \langle n_\uparrow \rangle + n_\downarrow + \langle n_\uparrow \rangle$ and the quantum Cramer-Rao bound for the phase sensitivity (see section 5.1) is thus

$$\Delta\phi_{\text{QCR}} = \frac{1}{\sqrt{m} \sqrt{2n_\downarrow \langle n_\uparrow \rangle + n_\downarrow + \langle n_\uparrow \rangle}} \quad (7.2)$$

where m is the number of independent measurements that are performed for the phase estimation. In the limit $\langle n_\uparrow \rangle \gg n_\downarrow$ of a large mean number of particles $\langle n_\uparrow \rangle$ in the state ρ_\uparrow compared to the n_\downarrow particles in the Fock-state, a gain of

$$\frac{\Delta\phi_{\text{QCR}}}{\Delta\phi_{\text{SN}}} = \frac{\sqrt{\langle n_\uparrow \rangle + n_\downarrow}}{\sqrt{2n_\downarrow \langle n_\uparrow \rangle + n_\downarrow + \langle n_\uparrow \rangle}} \approx \frac{1}{\sqrt{2n_\downarrow + 1}} \quad (7.3)$$

7. Outlook

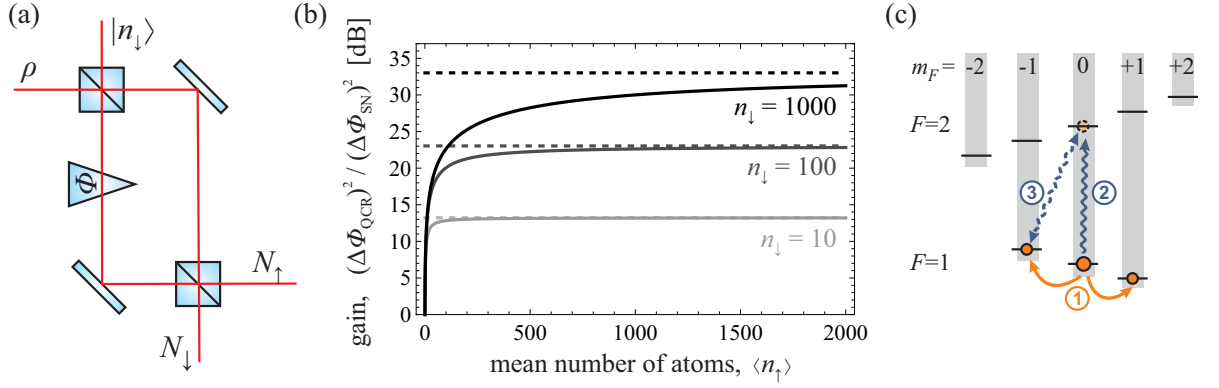


Figure 7.4.: **Quantum-enhanced interferometry due to a single Fock state.** (a) L. Pezzé and A. Smerzi showed that a Fock state $|n_{\downarrow}\rangle$ in one input port and an arbitrary state with a mean number of atoms $\langle n_{\uparrow} \rangle$ can be used to obtain sub-shot-noise phase sensitivity [130]. (b) The interferometric gain depends on the number of atoms in the Fock state n_{\downarrow} and reaches a constant level for $\langle n_{\uparrow} \rangle \gg n_{\downarrow}$. (c) Such an interferometer could be implemented with the pulse sequence shown here. After spin dynamics (1), the atoms from $|F, m_F\rangle = |1, 0\rangle$ are transferred to $|2, 0\rangle$. Coupling pulses between $|1, -1\rangle$ and $|2, 0\rangle$ are used to realize an interferometer sequence (3). Finally, the population of all 3 states is detected. The detected number of atoms in $m_F = +1$ can be used to infer the number of atoms that have been in $m_F = -1$ before the interferometer sequence.

compared to shot noise $\Delta\phi_{\text{SN}} = \frac{1}{\sqrt{m}\sqrt{\langle N \rangle}}$ can be achieved as shown in Fig. 7.4b. The quantum Cramer-Rao bound can be saturated for small phase shifts $\phi \approx 0$ by measuring the number of atoms N_{\downarrow} at a single output port. For $\phi = 0$ we find the same number of atoms at the input port as at the output port and thus have $N_{\downarrow} = n_{\downarrow}$ without any fluctuations. For an increasing phase shift $\phi > 0$ these fluctuations will grow rapidly and could be used for the phase estimation similar to the case of the twin-Fock interferometer presented in chapter 5.

For a proof of principle, this proposal can be realized in our experiment as illustrated in Fig. 7.4c. After spin dynamics we apply microwave pulses for an interferometer sequence between the atoms in $m_F = -1$ and $m_F = 0$. Subsequently, the number of atoms in all 3 internal states is measured. The atoms in the $m_F = +1$ level are not affected by the interferometer sequence. However, the number of atoms detected in this state can be used to estimate the number of atoms n_{\downarrow} in $m_F = -1$ before the interferometer sequence. In this sense, we can use the third mode to create an heralded Fock state at the input of the interferometer.

Additionally, the measurement of the number of atoms in both output modes N_{\uparrow} and N_{\downarrow} instead of only N_{\downarrow} as proposed by L. Pezzé and A. Smerzi can be used to measure the total number of atoms $N = N_{\uparrow} + N_{\downarrow}$. From this, we gain information about the number of atoms that have been at the second input port of the interferometer $n_{\uparrow} = N - n_{\downarrow}$.

Effectively, the input state is thus a heralded Dicke state $|n_{\uparrow}\rangle \otimes |n_{\downarrow}\rangle$. This reveals the entanglement of the input state. Furthermore, it shows the connection to the twin-Fock interferometer presented in chapter 5, which can also be operated with Dicke states close to a twin-Fock state.

This interferometer scheme has the advantage that it does not make any assumptions on the state ρ_{\uparrow} in one of the input ports. This facilitates the preparation even for a large number of particles. In particular, existing interferometers that are operated with uncorrelated atoms can be improved by simply replacing the vacuum state at one of the two input ports by a Fock state. A demonstration of sub-shot-noise sensitivity at a large number of atoms would pave the way from proof of principle experiments to applications in metrology.

A. Symmetric spin states

Here we will derive some of the spatial properties of spin states that are symmetric with respect to particle exchange. Naturally, such states can be found for indistinguishable Bosons with a symmetric spatial wave function. For particles that can be distinguished by their position, for example in an optical lattice, such states are also common, if the measurements and spin manipulations are homogeneous and do not resolve the spatial position of the individual particles.

A.1. Spin length of symmetric states

The length squared of the collective spin is defined as

$$\begin{aligned}\langle \mathbf{J}^2 \rangle &= \left\langle \left(\sum_{i=1}^N \mathbf{s}^{(i)} \right)^2 \right\rangle = \left\langle \left(\sum_{i=1}^N \mathbf{s}^{(i)} \right) \left(\sum_{j=1}^N \mathbf{s}^{(j)} \right) \right\rangle \\ &= \left\langle \sum_{i=1}^N (\mathbf{s}^{(i)})^2 \right\rangle + \left\langle \sum_{i \neq j} \mathbf{s}^{(i)} \otimes \mathbf{s}^{(j)} \right\rangle.\end{aligned}\tag{A.1}$$

For symmetric states the expectation values of the operators for the individual spins $\mathbf{s}^{(i)}$ and higher moments of these operators do not depend on the particle labels (i) and (j) and in this case we can thus write

$$\begin{aligned}\langle \mathbf{J}^2 \rangle &= N \langle (\mathbf{s}^{(1)})^2 \rangle + N(N-1) \sum_{k=x,y,z} \langle \mathbf{s}_k^{(1)} \otimes \mathbf{s}_k^{(2)} \rangle \\ &= N \frac{1}{2} \left(\frac{1}{2} + 1 \right) + \frac{1}{4} N(N-1) \sum_{k=x,y,z} \langle \sigma_k^{(1)} \otimes \sigma_k^{(2)} \rangle\end{aligned}\tag{A.2}$$

with the Pauli matrices σ_k . For a general symmetric pure state for two spin- $\frac{1}{2}$ particles

$$|\psi\rangle = a |\uparrow\uparrow\rangle + \frac{b}{\sqrt{2}} (|\uparrow\downarrow\rangle + |\downarrow\uparrow\rangle) + c |\downarrow\downarrow\rangle\tag{A.3}$$

it is easy to calculate

$$\langle \sigma_x^{(1)} \otimes \sigma_x^{(2)} \rangle = |b|^2\tag{A.4}$$

$$\langle \sigma_y^{(1)} \otimes \sigma_y^{(2)} \rangle = |b|^2\tag{A.5}$$

$$\langle \sigma_z^{(1)} \otimes \sigma_z^{(2)} \rangle = |a|^2 - |b|^2 + |c|^2.\tag{A.6}$$

A. Symmetric spin states

With the normalization condition $|a|^2 + |b|^2 + |c|^2 = 1$ we hence get

$$\sum_{k=x,y,z} \langle \sigma_k^{(1)} \otimes \sigma_k^{(2)} \rangle = |a|^2 + |b|^2 + |c|^2 = 1 \quad (\text{A.7})$$

which is not surprising since it is well known that symmetric coupling of two spin- $\frac{1}{2}$ particles leads to a collective spin-1 system. For the length of the collective spin for a symmetric state we thus get

$$\langle \mathbf{J}^2 \rangle = \frac{3}{4}N + \frac{1}{4}N(N-1) = \frac{N}{2}(\frac{N}{2} + 1) \quad (\text{A.8})$$

which equals $J(J+1)$ for $J = \frac{N}{2}$.

A.2. Number squeezing and entanglement of symmetric states

The connection between number squeezing $\Delta J_z < \frac{N}{2}$ and entanglement for symmetric states is shown in [62] as follows. The projection on the z-axis of the total spin is

$$J_z = \frac{1}{2} \sum_i \sigma_z^{(i)}. \quad (\text{A.9})$$

If its expectation value vanishes the variance is

$$(\Delta J_z)^2 = \langle J_z^2 \rangle = \frac{1}{4} \sum_{i,j} \langle \sigma_z^{(i)} \otimes \sigma_z^{(j)} \rangle = \frac{1}{4} \sum_i \langle (\sigma_z^{(i)})^2 \rangle + \frac{1}{4} \sum_{i \neq j} \langle \sigma_z^{(i)} \otimes \sigma_z^{(j)} \rangle \quad (\text{A.10})$$

Since $\sigma_z^2 = 1$ the first term simply equates to $\frac{N}{4}$ with N being the total number of particles. If we assume to have a symmetric state¹ the expectation value $\langle \sigma_z^{(i)} \otimes \sigma_z^{(j)} \rangle$ has to give the same result for each of the $N(N-1)$ pairs of particles $i \neq j$. We get

$$4(\Delta J_z)^2 = N + N(N-1) \langle \sigma_z^{(1)} \otimes \sigma_z^{(2)} \rangle \quad (\text{A.11})$$

This shows that for sub-shot-noise fluctuations

$$4(\Delta J_z)^2 < N \quad \Rightarrow \quad \langle \sigma_z^{(1)} \otimes \sigma_z^{(2)} \rangle < 0 \quad (\text{A.12})$$

This means if spin 1 is measured to point up we have a higher probability to measure that spin 2 points down. However, $\langle \sigma_z^{(1)} \rangle = 0$ shows that the measurement of the spin of a single particle gives up or down with equal probability.

To prove that this correlation can only be due to entanglement we need to show that $\langle \sigma_z^{(1)} \otimes \sigma_z^{(2)} \rangle \geq 0$ for any unentangled symmetric state

$$\rho_{\text{sep}} = \sum_k p_k \rho_k \otimes \rho_k \otimes \cdots \otimes \rho_k \quad (\text{A.13})$$

¹This is a rather strong assumption and a key ingredient here.

This is easy to check:

$$\begin{aligned}
 \langle \sigma_z^{(1)} \otimes \sigma_z^{(2)} \rangle &= \sum_k p_k \text{Tr} [(\rho_k \otimes \rho_k)(\sigma_z^{(1)} \otimes \sigma_z^{(2)})] \\
 &= \sum_k p_k \langle \sigma_z^{(2)} \rangle_k \langle \sigma_z^{(2)} \rangle_k = \sum_k p_k \langle \sigma_z^{(1)} \rangle_k^2 \geq 0
 \end{aligned} \tag{A.14}$$

Here $\langle \cdot \rangle_k$ denotes the expectation value with respect to the single particle pure state described by ρ_k .

B. The spin-squeezing parameter as an entanglement witness

In the last section we saw that sub-shot-noise fluctuations imply entanglement for symmetric states. It is not easy to verify experimentally whether a state is symmetric. But as symmetric states live on the surface of the many particle Bloch sphere it might be a good idea to include the length of the total spin $\langle J \rangle$ into an entanglement criterion, since $J \approx N/2$ for an almost symmetric state. Thus the spin-squeezing parameter by Wineland *et al.* $\xi^2 = \frac{N(\Delta J_z)^2}{\langle J_x \rangle^2}$ [61] can be used for an entanglement criterion as has been shown by Sørensen *et al.* [45]. The proof is as follows: By definition a general separable state can be written as

$$\rho_{\text{sep}} = \sum_k p_k \rho_k^{(1)} \otimes \rho_k^{(2)} \otimes \cdots \otimes \rho_k^{(N)} \quad \text{with} \quad \sum_k p_k = 1 \quad \text{and} \quad p_k \geq 0 \quad (\text{B.1})$$

where $\rho_k^{(i)} = \rho_k^{(j)} \forall i, j, k$ is only true for symmetric separable states. Using this similar to the last section we can calculate

$$\begin{aligned} (\Delta J_z)^2 &= \langle J_z^2 \rangle - \langle J_z \rangle^2 = \frac{1}{4} \sum_k p_k \left\langle \left(\sum_i \sigma_z^{(i)} \right) \left(\sum_j \sigma_z^{(j)} \right) \right\rangle_k - \langle J_z \rangle^2 \\ &= \frac{1}{4} \sum_k p_k \left[\sum_i \langle (\sigma_z^{(i)})^2 \rangle_k + \sum_{i \neq j} \langle \sigma_z^{(i)} \rangle_k \langle \sigma_z^{(j)} \rangle_k \right] - \langle J_z \rangle^2 \\ &= \frac{N}{4} + \frac{1}{4} \sum_k p_k \left[\sum_{i,j} \langle \sigma_z^{(i)} \rangle_k \langle \sigma_z^{(j)} \rangle_k - \sum_i \langle \sigma_z^{(i)} \rangle_k^2 \right] - \langle J_z \rangle^2 \\ &= \frac{N}{4} - \frac{1}{4} \sum_k p_k \sum_i \langle \sigma_z^{(i)} \rangle_k^2 + \sum_k p_k \langle J_z \rangle_k^2 - \langle J_z \rangle^2 \end{aligned} \quad (\text{B.2})$$

To estimate a lower bound for $(\Delta J_z)^2$ we can drop the last two terms since $\sum_k p_k \langle J_z \rangle_k^2 \geq \langle J_z \rangle^2 = (\sum_k p_k \langle J_z \rangle_k)^2$ and get

$$(\Delta J_z)^2 \geq \frac{N}{4} - \frac{1}{4} \sum_k p_k \sum_i \langle \sigma_z^{(i)} \rangle_k^2 \quad (\text{B.3})$$

Now we can use $\langle \sigma_x \rangle^2 + \langle \sigma_y \rangle^2 + \langle \sigma_z \rangle^2 \leq 1$ to get

$$(\Delta J_z)^2 \geq \frac{1}{4} \sum_k p_k \sum_i \left[\langle \sigma_x^{(i)} \rangle_k^2 + \langle \sigma_y^{(i)} \rangle_k^2 \right] \quad (\text{B.4})$$

B. The spin-squeezing parameter as an entanglement witness

Finally we use $(\sum_i a_i)^2 = \sum_{i,j} a_i a_j \leq N \sum_i a_i^2$ and have

$$(\Delta J_z)^2 \geq \frac{\langle J_x \rangle^2 + \langle J_y \rangle^2}{N} \quad (\text{B.5})$$

and hence

$$\Leftrightarrow \quad \xi^2 = \frac{N(\Delta J_z)^2}{\langle J_x \rangle^2 + \langle J_y \rangle^2} \geq 1. \quad (\text{B.6})$$

Note that in section 2.4 we assumed that the state is oriented along J_x and thus $\langle J_y \rangle = 0$. In this case the spin-squeezing parameters ξ^2 in eq. (B.6) and (2.50) are identical.

C. Time evolution of the \mathbf{K} -vector

For the spin dynamics Hamiltonian $H = 2\Omega K_y$ the time evolution of the \mathbf{K} operator is

$$i \frac{d}{dt} \mathbf{K} = 2\Omega [K_y, \mathbf{K}]. \quad (\text{C.1})$$

Using the commutation relations

$$\begin{aligned} [K_x, K_y] &= -iK_z \\ [K_y, K_z] &= iK_x \\ [K_z, K_x] &= iK_y \end{aligned} \quad (\text{C.2})$$

we get

$$i \frac{d}{dt} \mathbf{K} = i2\Omega \begin{pmatrix} K_z \\ 0 \\ K_x \end{pmatrix} = i2\Omega \begin{pmatrix} 0 & 0 & 1 \\ 0 & 0 & 0 \\ 1 & 0 & 0 \end{pmatrix} \begin{pmatrix} K_x \\ K_y \\ K_z \end{pmatrix} \quad (\text{C.3})$$

Obviously, the K_y component will stay constant. For the remaining two components we have

$$\frac{d}{dt} \begin{pmatrix} K_x \\ K_y \end{pmatrix} = 2\Omega M \begin{pmatrix} K_x \\ K_y \end{pmatrix} \quad \text{with} \quad M = \begin{pmatrix} 0 & 1 \\ 1 & 0 \end{pmatrix} \quad (\text{C.4})$$

with the formal solution

$$\begin{pmatrix} K_x(t) \\ K_y(t) \end{pmatrix} = e^{t2\Omega M} \begin{pmatrix} K_x \\ K_y \end{pmatrix}. \quad (\text{C.5})$$

Since

$$M^2 = \begin{pmatrix} 1 & 0 \\ 0 & 1 \end{pmatrix} \quad (\text{C.6})$$

it is beneficial to split the power series of the exponential function in its even and odd parts yielding

$$e^{t2\Omega M} = \begin{pmatrix} 0 & 1 \\ 1 & 0 \end{pmatrix} \sum_{n=0}^{\infty} \frac{(t2\Omega)^{2n+1}}{(2n+1)!} + \begin{pmatrix} 1 & 0 \\ 0 & 1 \end{pmatrix} \sum_{n=0}^{\infty} \frac{(t2\Omega)^{2n}}{(2n)!} \quad (\text{C.7})$$

$$= \begin{pmatrix} \cosh(t2\Omega) & \sinh(t2\Omega) \\ \sinh(t2\Omega) & \cosh(t2\Omega) \end{pmatrix} \quad (\text{C.8})$$

Hence, in total the time evolution vector operator \mathbf{K} is

$$\begin{pmatrix} K_x(t) \\ K_y(t) \\ K_z(t) \end{pmatrix} = \begin{pmatrix} \cosh(t2\Omega) & 0 & \sinh(t2\Omega) \\ 0 & 1 & 0 \\ \sinh(t2\Omega) & 0 & \cosh(t2\Omega) \end{pmatrix} \begin{pmatrix} K_x \\ K_y \\ K_z \end{pmatrix} \quad (\text{C.9})$$

D. CCD camera calibration

For a correct atom number estimation we need a precise calibration of our CCD camera (Princeton instruments, pixis 1024_BR eXcelon) as pointed out in section 4.4.3.

D.1. Calibration of the camera gain

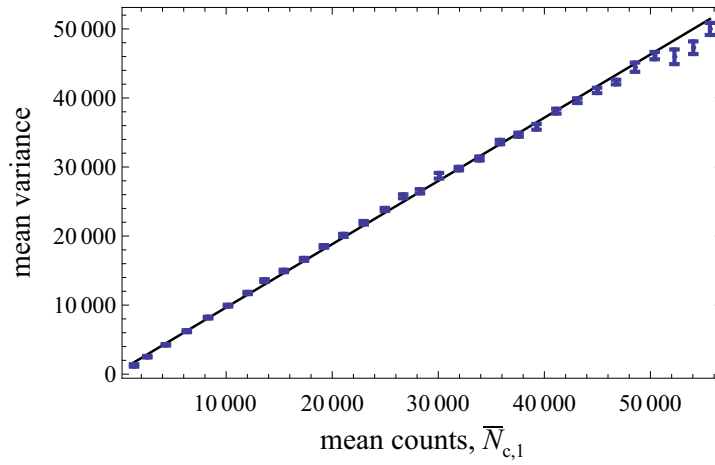


Figure D.1.: **Calibration of the camera gain.** From the slope of the variance $\frac{1}{2} \left(\Delta(N_{c,1}^{(i)} - N_{c,2}^{(i)}) \right)^2$ as a function of the mean number of digital counts $\bar{N}_{c,1}$ we can estimate the gain of the camera to be $g = 1.09$.

The first quantity of the camera is the so-called gain g giving the number of digital counts per primary electron which has been created by an detected photon on a CCD pixel. The number of primary electrons N_{el} is subject to shot-noise fluctuations $\Delta N_{\text{el}} = \sqrt{N_{\text{el}}}$. The number of digital counts N_c thus fluctuates with

$$\Delta N_c = g \Delta N_{\text{el}} = g \sqrt{N_{\text{el}}} = \sqrt{\frac{N_c}{g}} \quad (\text{D.1})$$

If we vary the number of primary electrons and plot the variance $(\Delta N_{\text{el}})^2$ against the number of primary electrons N_{el} we can extract the camera gain g from the slope of the expected linear dependence.

We have to take care that the shot noise is the dominant noise source such that all technical noise sources can be neglected. Such noise sources would lead to a variance

D. CCD camera calibration

$\Delta N_c \propto N_c^2$ and spoil the calibration. We thus have to achieve a very homogeneous illumination to suppress the influence of mechanical vibrations. Additionally, the illumination intensity has to be constant in time.

To achieve a homogeneous illumination of the CCD camera we choose an ordinary torch as an incoherent light source to avoid diffraction fringes as described in section 4.4.5. Note, that the wavelength of the light used for the calibration of the gain factor is not important since it only depends on the electronics which amplify the primary electrons and the analogue-digital converters which convert the resulting signal into digital counts. The light has to pass through three sheets of white paper before it reaches the camera which diffuses the light to avoid a bright spot in the middle and achieve homogeneous illumination. The influence of spatial inhomogeneity can be further suppressed by considering the fluctuations of the difference in the number of counts $N_{c,1}^{(i)} - N_{c,2}^{(i)}$ on one pixel in two successive images. If an other camera pixel is illuminated with another mean intensity leading to another mean number of digital counts $\langle N_c^{(i)} \rangle \neq \langle N_c^{(j)} \rangle$ this does not effect the variance

$$\frac{1}{2} \left(\Delta(N_{c,1}^{(i)} - N_{c,2}^{(i)}) \right)^2 = \frac{N_c}{g}. \quad (\text{D.2})$$

Furthermore, shot to shot power fluctuations can be suppressed by comparing the average counts of two successive images $\bar{N}_{c,1} = \sum_i N_{c,1}^{(i)}$ and $\bar{N}_{c,2} = \sum_i N_{c,2}^{(i)}$ and adjusting the counts of the second image $N_{c,2}^{(i)} \rightarrow \frac{\bar{N}_{c,1}}{\bar{N}_{c,2}} N_{c,2}^{(i)}$ such that both images have the same average number of counts.

With this method we record the data presented in Fig. D.1. We estimate a gain of $g = 1.09$ digital counts per detected photon in reasonable agreement with the specified gain of $g = 1.0$.

D.2. Calibration of the quantum efficiency

Here we present the estimation of the quantum efficiency $\eta = \frac{N_{\text{el}}}{N_{\text{ph}}}$, which is the number of detected photons N_{el} which have been converted to primary electrons divided by the number of incident photons. The number of primary electrons can be readily calculated $N_{\text{el}} = \frac{N_c}{g}$ from the number of digital counts N_c with the camera gain g which has been measured as described in the last section.

We illuminate the camera with a coherent laser beam resonant to the cycling transition in ^{87}Rb used for the absorption detection. We make sure that the beam is much smaller than the CCD chip such that it completely fits on the camera. With a calibrated diode detector we can measure the power of the laser beam. The number of photons incident on the camera is

$$N_{\text{ph}} = \frac{t P}{h\nu} \quad (\text{D.3})$$

with the illumination time t .

D.2. Calibration of the quantum efficiency

We measure a quantum efficiency of $\eta = 0.97(1)$ in reasonable agreement with the specified quantum efficiency of $\eta = 0.98$ at this wavelength. We checked that the result does not depend on the illumination intensity and time.

E. Statistically correct error bars for estimated variances

For our experiments, we determine the second central moment μ_2 of an unknown probability distribution $p(x)$. A quantity x is measured with the probability $p(x)$ of the underlying probability distribution. To estimate the second central moment μ_2 of this distribution we repeat the experiment and record a sample of these quantities $\{x_1, x_2, \dots, x_n\}$. In the limit of an infinitely large sample, the second central moment of the sample

$$m_2 = \frac{1}{n} \sum_i \left(x_i - \frac{1}{n} \sum_j x_j \right)^2 \quad (\text{E.1})$$

is equal to the second central moment of the underlying distribution

$$\lim_{n \rightarrow \infty} m_2 = \mu_2. \quad (\text{E.2})$$

For a finite sample size n , there will be deviations. Moreover, the expectation value Em_2 of the second central moment of the sample, i.e. the average result of such an experiment, is not equal to the second central moment of the underlying distribution

$$Em_2 \neq \mu_2 \quad (\text{E.3})$$

Thus, m_2 is called a *biased* estimator for the second central moment of the distribution. Explicit calculations yield

$$Em_2 = \frac{n-1}{n} \mu_2 \quad (\text{E.4})$$

This shows that

$$\hat{\mu}_2 = \frac{n}{n-1} m_2 \quad (\text{E.5})$$

is an *unbiased* estimator for μ_2 since according to Eq. (E.4) the expectation value of $\hat{\mu}_2$ is precisely μ_2 .

A more subtle question is to ask how much the expectation value of the estimator $\hat{\mu}_2$ will fluctuate from sample to sample and thus to determine its error bars. In other words we need to find an estimator for $\text{var}(\hat{\mu}_2) = \text{var}(\frac{n}{n-1} m_2)$.

In the following we will derive such an estimator that can be applied without further assumptions about the (unknown) probability distribution of $\{x_i\}$.

E.1. Augmented and monomial symmetric functions

As we will see, for this task it is very useful to use augmented and monomial symmetric functions (see [131] p. 416). The augmented symmetric function is defined as

$$[p_1^{\pi_1} p_2^{\pi_2} \dots p_s^{\pi_s}] = \sum x_i^{p_1} x_j^{p_1} \dots x_q^{p_2} x_r^{p_2} \dots x_u^{p_s} x_v^{p_s} \quad (\text{E.6})$$

where there are π_1 powers of p_1 , π_2 powers of p_2 and so on. All suffixes in the sum are supposed to be different $i \neq j \neq \dots \neq v$ and, subject to this, the summation takes place over all values of x . Thus there are $n(n-1)\dots(n-p)$ terms in the summation with $p = \sum_{i=1}^s \pi_i$. Hence by taking the expectation value we get

$$E([p_1^{\pi_1} p_2^{\pi_2} \dots p_s^{\pi_s}]) = n(n-1)\dots(n-p)(\mu'_{p_1})^{\pi_1}(\mu'_{p_2})^{\pi_2}\dots(\mu'_{p_s})^{\pi_s} \quad (\text{E.7})$$

where μ'_r denotes the r th (non-central) moment of the distribution.

The monomial functions are defined as

$$(p_1^{\pi_1} p_2^{\pi_2} \dots p_s^{\pi_s}) = [p_1^{\pi_1} p_2^{\pi_2} \dots p_s^{\pi_s}] / (\pi_1! \pi_2! \dots \pi_s!) \quad (\text{E.8})$$

In Appendix 10 of reference [131] there are tables giving these functions in terms of each other which will be used in the following.

E.2. $\text{var}(\hat{\mu}_2)$ in terms of μ_4 and μ_2^2

As a first step to find an estimator for $\text{var}(\hat{\mu}_2)$, let us express it in terms of μ_4 and μ_2^2 .

$$\begin{aligned} \text{var}(\hat{\mu}_2) &= \frac{n^2}{(n-1)^2} \text{var}(m_2) = \frac{n^2}{(n-1)^2} (Em_2^2 - (Em_2)^2) \\ &= \frac{n^2}{(n-1)^2} Em_2^2 - \mu_2^2 \end{aligned} \quad (\text{E.9})$$

where Eq. (E.4) has been used for the last step.

The expectation value Em_2^2 can be found using the augmented and monomial symmetric functions as follows.

$$\begin{aligned} m_2^2 &= \left(\frac{1}{n} \sum x_i^2 - \left(\frac{1}{n} \sum x_i \right)^2 \right)^2 \\ &= \left(\frac{(2)}{n} - \frac{(1)^2}{n^2} \right)^2 = \frac{(2)^2}{n^2} - 2 \frac{(2)(1)^2}{n^3} + \frac{(1)^4}{n^4} \end{aligned} \quad (\text{E.10})$$

Now the table in Appendix 10 of reference [131] can be used to transform the monomial symmetric functions into augmented symmetric functions giving the following result

$$m_2^2 = \frac{[4] + [2^2]}{n^2} - 2 \frac{[4] + 2[31] + [2^2] + [21^2]}{n^3} + \frac{[4] + 4[31] + 3[2^2] + 6[21^2] + [1^4]}{n^4} \quad (\text{E.11})$$

To shorten the calculation all terms containing $[\dots 1^{\pi_i} \dots]$ can be dropped directly for the following reason: all of these terms would result in a term $\dots \mu_1^{\pi_i} \dots$ containing the first moment when taking the average. However, m_2 should not depend on the position of the center of the distribution and thus it does not depend on μ_1 . Hence, we know that these terms will cancel in the following calculation. We thus get

$$\begin{aligned} m_2^2 &= \frac{[4] + [2^2]}{n^2} - 2 \frac{[4] + [2^2]}{n^3} + \frac{[4] + 3[2^2]}{n^4} \\ &= \frac{(n-1)^2}{n^4} [4] + \frac{n^2 - 2n + 3}{n^4} [2^2] \end{aligned} \quad (\text{E.12})$$

Using Eq. (E.7) we get for the expectation value

$$Em_2^2 = \frac{(n-1)^2}{n^3} \mu_4 + \frac{(n-1)(n^2 - 2n + 3)}{n^3} \mu_2^2 \quad (\text{E.13})$$

Finally we have

$$\text{var}(\hat{\mu}_2) = \frac{\mu_4}{n} - \frac{n-3}{n(n-1)} \mu_2^2 \quad (\text{E.14})$$

This equation reduces the problem of finding an estimator for $\text{var}(\hat{\mu}_2)$ to finding estimators for μ_4 and μ_2^2 . This will be done in the following two sections using the same technique.

E.3. Finding estimators for μ_4 and μ_2^2

Using the same technique as in the previous section, we calculate for Em_4

$$\begin{aligned} m_4 &= \frac{1}{n} \sum_i \left(x_i - \frac{1}{n} \sum_j x_j \right)^4 \\ &= \frac{1}{n} \sum_i \left(x_i^4 - \frac{4}{n} x_i^3 \sum_j x_j + \frac{6}{n^2} x_i^2 \left(\sum_j x_j \right)^2 - \frac{4}{n^3} x_i \left(\sum_j x_j \right)^3 + \frac{1}{n^4} \left(\sum_j x_j \right)^4 \right) \\ &= \frac{(4)}{n} - 4 \frac{(1)(3)}{n^2} + 6 \frac{(2)(1)^2}{n^3} - 4 \frac{(1)^4}{n^4} + \frac{(1)^4}{n^4} \\ &= \frac{[4]}{n} - 4 \frac{[4]}{n^2} + 6 \frac{[4] + [2^2]}{n^3} - 3 \frac{[4] + 3[2^2]}{n^4} \\ &= \frac{1}{n^4} ((n^3 - 4n^2 + 6n - 3)[4] + (6n - 9)[2^2]) \\ \Rightarrow Em_4 &= \frac{n^3 - 4n^2 + 6n - 3}{n^3} \mu_4 + \frac{3(n-1)(2n-3)}{n^3} \mu_2^2. \end{aligned} \quad (\text{E.15})$$

Solving the Eqs. (E.15) and (E.13) for μ_4 and μ_2^2 finally yields

$$\mu_4 = \frac{n}{(n-1)(n-1)(n-3)} ((n^2 - 2n + 3)Em_4 - 3(2n-3)Em_2^2) \quad (\text{E.16})$$

$$\mu_2^2 = \frac{n}{(n-1)(n-2)(n-3)} ((n^2 - 3n + 3)Em_2^2 - (n-1)Em_4) \quad (\text{E.17})$$

We thus found the following estimators for μ_4 and μ_2^2

$$\hat{\mu}_4 = \frac{n}{(n-1)(n-1)(n-3)} ((n^2 - 2n + 3)m_4 - 3(2n-3)m_2^2) \quad (\text{E.18})$$

$$\hat{\mu}_2^2 = \frac{n}{(n-1)(n-2)(n-3)} ((n^2 - 3n + 3)m_2^2 - (n-1)m_4) \quad (\text{E.19})$$

E.4. The estimator for $\text{var}(\hat{\mu}_2)$

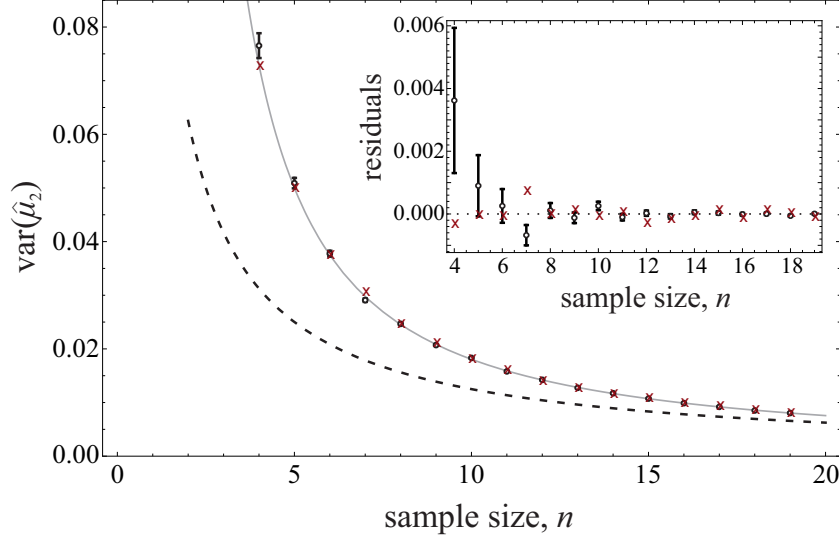


Figure E.1.: Application of the new estimator to a set of generated random numbers. We have generate random numbers according to a probability distribution $p(x)$. For each sample size n , we have applied the new estimator to 10^4 samples. The open circles present the mean of the calculated estimator with their statistical uncertainties. These results compare well to the directly calculated variance of the 10^4 sample variances (red crosses). It is statistically equal to the exact prediction of Eq. (E.14) (black solid line) and completely incompatible with the naive guess $\text{var}(\hat{\mu}_2) \approx \frac{1}{n}(\mu_4 - \mu_2^2)$ (dashed line).

By plugging Eq. (E.18) and (E.19) in Eq. (E.14)) and further simplifying the equation, we find the desired estimator for $\text{var}(\hat{\mu}_2)$

$$\text{var}(\hat{\mu}_2) \approx n \frac{m_4(n-1)^2 - m_2^2(n^2-3)}{(n-3)(n-2)(n-1)^2} \quad (\text{E.20})$$

For a verification of the correctness of this estimator, we numerically generate random samples $\{x_1, x_2, \dots, x_n\}$ with different sample lengths n . For each sample length, we generate 10^4 samples and apply the estimator and the results are shown in Fig. E.1 as black circles with error bars. The estimator agrees with the fluctuations of the 10^4

estimations of the central second moment $\hat{\mu}_2$ shown as red crosses and the exact value of Eq. (E.14). We performed this test for a variety of probability distributions $p(x)$ yielding similar results and thus confirmed that the estimator gives correct results independent of the shape of the probability distribution.

Bibliography

- [1] E. Schrödinger. Discussion of probability relations between separated systems. *Math. Proc. Cambridge*, **31**, 555 (1935).
- [2] W. H. Zurek. Decoherence, einselection, and the quantum origins of the classical. *Rev. Mod. Phys.*, **75**, 715 (2003).
- [3] T. Monz, P. Schindler, J. T. Barreiro, M. Chwalla, D. Nigg, W. A. Coish, M. Harlander, W. Hänsel, M. Hennrich, and R. Blatt. 14-qubit entanglement: Creation and coherence. *Phys. Rev. Lett.*, **106**, 130506 (2011).
- [4] X.-C. Yao, T.-X. Wang, P. Xu, H. Lu, G.-S. Pan, X.-H. Bao, C.-Z. Peng, C.-Y. Lu, Y.-A. Chen, and J.-W. Pan. Observation of eight-photon entanglement. *Nature Photon.*, **6**, 225 (2012).
- [5] D. Bouwmeester, J.-W. Pan, M. Daniell, H. Weinfurter, and A. Zeilinger. Observation of three-photon Greenberger-Horne-Zeilinger entanglement. *Phys. Rev. Lett.*, **82**, 1345 (1999).
- [6] C. A. Sackett, D. Kielpinski, B. E. King, C. Langer, V. Meyer, C. J. Myatt, M. Rowe, Q. A. Turchette, W. M. Itano, D. J. Wineland, and C. Monroe. Experimental entanglement of four particles. *Nature (London)*, **404**, 256 (2000).
- [7] H. Häffner, W. Hänsel, C. F. Roos, J. Benhelm, D. Chek-al kar, M. Chwalla, T. Körber, U. D. Rapol, M. Riebe, P. O. Schmidt, C. Becher, O. Gühne, W. Dür, and R. Blatt. Scalable multiparticle entanglement of trapped ions. *Nature (London)*, **438**, 643 (2005).
- [8] Z. Zhao, Y.-A. Chen, A.-N. Zhang, T. Yang, H. J. Briegel, and J.-W. Pan. Experimental demonstration of five-photon entanglement and open-destination teleportation. *Nature (London)*, **430**, 54 (2004).
- [9] C.-Y. Lu, X.-Q. Zhou, O. Gühne, W.-B. Gao, J. Zhang, Z.-S. Yuan, A. Goebel, T. Yang, and J.-W. Pan. Experimental entanglement of six photons in graph states. *Nat. Phys.*, **3**, 91 (2007).
- [10] M. Neeley, R. C. Bialczak, M. Lenander, E. Lucero, M. Mariantoni, A. D. O'Connell, D. Sank, H. Wang, M. Weides, J. Wenner, Y. Yin, T. Yamamoto, A. N. Cleland, and J. M. Martinis. Generation of three-qubit entangled states using superconducting phase qubits. *Nature (London)*, **467**, 570 (2010).

- [11] L. DiCarlo, M. D. Reed, L. Sun, B. R. Johnson, J. M. Chow, J. M. Gambetta, L. Frunzio, S. M. Girvin, M. H. Devoret, and R. J. Schoelkopf. Preparation and measurement of three-qubit entanglement in a superconducting circuit. *Nature (London)*, **467**, 574 (2010).
- [12] P. Neumann, N. Mizuochi, F. Rempp, P. Hemmer, H. Watanabe, S. Yamasaki, V. Jacques, T. Gaebel, F. Jelezko, and J. Wrachtrup. Multipartite entanglement among single spins in diamond. *Science*, **320**, 1326 (2008).
- [13] C. Gross, T. Zibold, E. Nicklas, J. Estève, and M. K. Oberthaler. Nonlinear atom interferometer surpasses classical precision limit. *Nature (London)*, **464**, 1165 (2010).
- [14] P. Fritschel and the LIGO Scientific Collaboration. Ligo: the laser interferometer gravitational-wave observatory. *Rep. Prog. Phys.*, **72**, 076901 (2009).
- [15] H. Grote and the LIGO Scientific Collaboration. The GEO 600 status. *Classical Quantum Gravity*, **27**, 084003 (2010).
- [16] K. U. Schreiber, T. Klügel, J.-P. R. Wells, R. B. Hurst, and A. Gebauer. How to detect the Chandler and the annual wobble of the Earth with a large ring laser gyroscope. *Phys. Rev. Lett.*, **107**, 173904 (2011).
- [17] I. K. Kominis, T. W. Kornack, J. C. Allred, and M. V. Romalis. A subfemtotesla multichannel atomic magnetometer. *Nature (London)*, **422**, 596 (2003).
- [18] P. Böhi, M. F. Riedel, T. W. Hänsch, and P. Treutlein. Imaging of microwave fields using ultracold atoms. *Appl. Phys. Lett.*, **97**, (2010).
- [19] T. L. Gustavson, P. Bouyer, and M. A. Kasevich. Precision rotation measurements with an atom interferometer gyroscope. *Phys. Rev. Lett.*, **78**, 2046 (1997).
- [20] G. Tackmann, P. Berg, C. Schubert, S. Abend, M. Gilowski, W. Ertmer, and E. M. Rasel. Self-alignment of a compact large-area atomic Sagnac interferometer. *New J. Phys.*, **14**, 015002 (2012).
- [21] A. Gauguier, B. Canuel, T. Lévêque, W. Chaibi, and A. Landragin. Characterization and limits of a cold-atom Sagnac interferometer. *Phys. Rev. A*, **80**, 063604 (2009).
- [22] S. Merlet, Q. Bodart, N. Malossi, A. Landragin, F. Pereira Dos Santos, O. Gitlein, and L. Timmen. Comparison between two mobile absolute gravimeters: optical versus atomic interferometers. *Metrologia*, **47**, L9 (2010).
- [23] J. K. Stockton, K. Takase, and M. A. Kasevich. Absolute geodetic rotation measurement using atom interferometry. *Phys. Rev. Lett.*, **107**, 133001 (2011).

- [24] A. Peters, K. Y. Chung, and S. Chu. Measurement of gravitational acceleration by dropping atoms. *Nature (London)*, **400**, 849 (1999).
- [25] J. Appel, P. J. Windpassinger, D. Oblak, U. B. Hoff, N. Kærgaard, and E. S. Polzik. Mesoscopic atomic entanglement for precision measurements beyond the standard quantum limit. *Proc. Natl. Acad. Sci. U. S. A.*, **106**, 10960 (2009).
- [26] Z. Chen, J. Bohnet, S. Sankar, J. Dai, and J. Thompson. Conditional spin squeezing of a large ensemble via the vacuum Rabi splitting. *Phys. Rev. Lett.*, **106**, 133601 (2011).
- [27] M. H. Schleier-Smith, I. D. Leroux, and V. Vuletić. States of an ensemble of two-level atoms with reduced quantum uncertainty. *Phys. Rev. Lett.*, **104**, 073604 (2010).
- [28] J. Estève, C. Gross, A. Weller, S. Giovanazzi, and M. K. Oberthaler. Squeezing and entanglement in a bose-einstein condensate. *Nature (London)*, **455**, 1216 (2008).
- [29] M. Riedel, P. Böhi, Y. Li, T. Hänsch, A. Sinatra, and P. Treutlein. Atom-chip-based generation of entanglement for quantum metrology. *Nature (London)*, **464**, 1170 (2010).
- [30] C. Klempt, O. Topic, G. Gebreyesus, M. Scherer, T. Henninger, P. Hyllus, W. Ertmer, L. Santos, and J. J. Arlt. Multiresonant spinor dynamics in a Bose-Einstein condensate. *Phys. Rev. Lett.*, **103**, 195302 (2009).
- [31] C. Klempt, O. Topic, G. Gebreyesus, M. Scherer, T. Henninger, P. Hyllus, W. Ertmer, L. Santos, and J. J. Arlt. Parametric amplification of vacuum fluctuations in a spinor condensate. *Phys. Rev. Lett.*, **104**, 195303 (2010).
- [32] C. Gross, H. Strobel, E. Nicklas, T. Zibold, N. Bar-Gill, G. Kurizki, and M. K. Oberthaler. Atomic homodyne detection of continuous-variable entangled twin-atom states. *Nature (London)*, **480**, 219 (2011).
- [33] C. D. Hamley, C. S. Gerving, T. M. Hoang, E. M. Bookjans, and M. S. Chapman. Spin-nematic squeezed vacuum in a quantum gas. *Nat. Phys.*, **8**, 305 (2012).
- [34] B. Lücke, J. Peise, G. Vitagliano, J. Arlt, L. Santos, G. Tóth, and C. Klempt. Detecting multiparticle entanglement of Dicke states. *Phys. Rev. Lett.*, **112**, 155304 (2014).
- [35] B. Lücke, M. Scherer, J. Kruse, L. Pezzé, F. Deuretzbacher, P. Hyllus, O. Topic, J. Peise, W. Ertmer, J. Arlt, L. Santos, A. Smerzi, and C. Klempt. Twin matter waves for interferometry beyond the classical limit. *Science*, **334**, 773 (2011).
- [36] A. Einstein, B. Podolsky, and N. Rosen. Can quantum-mechanical description of physical reality be considered complete? *Phys. Rev.*, **47**, 777 (1935).

- [37] J. S. Bell. On the Einstein-Podolsky-Rosen paradox. *Physics*, **1**, 195 (1964).
- [38] A. Aspect, J. Dalibard, and G. Roger. Experimental test of Bell’s inequalities using time-varying analyzers. *Phys. Rev. Lett.*, **49**, 1804 (1982).
- [39] A. Aspect. Bell’s inequality test: more ideal than ever. *Nature (London)*, **398**, 189 (1999).
- [40] S. Gröblacher, T. Paterek, R. Kaltenbaek, C. Brukner, M. Zukowski, M. Aspelmeyer, and A. Zeilinger. An experimental test of non-local realism. *Nature*, **446**, 871 (2007).
- [41] D. Dieks. Communication by EPR devices. *Phys. Lett. A*, **92**, 271 (1982).
- [42] R. Horodecki, P. Horodecki, M. Horodecki, and K. Horodecki. Quantum entanglement. *Rev. Mod. Phys.*, **81**, 865 (2009).
- [43] H. Ollivier and W. H. Zurek. Quantum discord: A measure of the quantumness of correlations. *Phys. Rev. Lett.*, **88**, 017901 (2001).
- [44] P. Hyllus, L. Pezzé, A. Smerzi, and G. Tóth. Entanglement and extreme spin squeezing for a fluctuating number of indistinguishable particles. *Phys. Rev. A*, **86**, 012337 (2012).
- [45] A. Sørensen, L.-M. Duan, J. I. Cirac, and P. Zoller. Many-particle entanglement with Bose-Einstein condensates. *Nature (London)*, **409**, 63 (2001).
- [46] A. Ekert and R. Jozsa. Quantum computation and Shor’s factoring algorithm. *Rev. Mod. Phys.*, **68**, 733 (1996).
- [47] N. Gisin and R. Thew. Quantum communication. *Nat. Photonics*, **1**, 165 (2007).
- [48] B. J. Bloom, T. L. Nicholson, J. R. Williams, S. L. Campbell, M. Bishof, X. Zhang, W. Zhang, S. L. Bromley, and J. Ye. An optical lattice clock with accuracy and stability at the 10^{-18} level. *Nature (London)*, **advance online publication**, (2014).
- [49] The LIGO Scientific Collaboration. Enhanced sensitivity of the ligo gravitational wave detector by using squeezed states of light. *Nat. Photonics*, **7**, 613 (2013).
- [50] D. Johnson. *Long baseline atom interferometry*. PhD thesis, Stanford University. Dept. of Physics (2011).
- [51] Z. Y. Ou. Fundamental quantum limit in precision phase measurement. *Phys. Rev. A*, **55**, 2598 (1997).
- [52] M. Napolitano, M. Koschorreck, B. Dubost, N. Behbood, R. J. Sewell, and M. W. Mitchell. Interaction-based quantum metrology showing scaling beyond the Heisenberg limit. *Nature (London)*, **471**, 486 (2011).

- [53] H. F. Hofmann. All path-symmetric pure states achieve their maximal phase sensitivity in conventional two-path interferometry. *Phys. Rev. A*, **79**, 033822 (2009).
- [54] P. M. Anisimov, G. M. Raterman, A. Chiruvelli, W. N. Plick, S. D. Huver, H. Lee, and J. P. Dowling. Quantum metrology with two-mode squeezed vacuum: Parity detection beats the Heisenberg limit. *Phys. Rev. Lett.*, **104**, 103602 (2010).
- [55] R. P. Feynman, F. L. Vernon, and R. W. Hellwarth. Geometrical representation of the Schrödinger equation for solving maser problems. *J. Appl. Phys.*, **28**, 49 (1957).
- [56] T. Mayer-Kuckuk. *Atomphysik: Eine Einführung (Teubner Studienbücher Physik) (German Edition)*. Vieweg+Teubner Verlag (1997).
- [57] B. Yurke, S. L. McCall, and J. R. Klauder. SU(2) and SU(1,1) interferometers. *Phys. Rev. A*, **33**, 4033 (1986).
- [58] T. Kim, O. Pfister, M. J. Holland, J. Noh, and J. L. Hall. Influence of decorrelation on Heisenberg-limited interferometry with quantum correlated photons. *Phys. Rev. A*, **57**, 4004 (1998).
- [59] M. Kitagawa and M. Ueda. Squeezed spin states. *Phys. Rev. A*, **47**, 5138 (1993).
- [60] X. Wang and B. C. Sanders. Relations between bosonic quadrature squeezing and atomic spin squeezing. *Phys. Rev. A*, **68**, 033821 (2003).
- [61] D. J. Wineland, J. J. Bollinger, W. M. Itano, F. L. Moore, and D. J. Heinzen. Spin squeezing and reduced quantum noise in spectroscopy. *Phys. Rev. A*, **46**, R6797 (1992).
- [62] X. Wang and B. C. Sanders. Spin squeezing and pairwise entanglement for symmetric multiqubit states. *Phys. Rev. A*, **68**, 012101 (2003).
- [63] A. Sørensen and K. Mølmer. Entanglement and extreme spin squeezing. *Phys. Rev. Lett.*, **86**, 4431 (2001).
- [64] J. Dalibard. Collisional dynamics of ultra-cold atomic gases. In M. Inguscio, S. Stringari, and C. E. Wieman, editors, *Proceedings of the International School of Physics - Enrico Fermi*, volume 321. IOS Press (1999).
- [65] J.-W. Pan, Z.-B. Chen, C.-Y. Lu, H. Weinfurter, A. Zeilinger, and M. Żukowski. Multiphoton entanglement and interferometry. *Rev. Mod. Phys.*, **84**, 777 (2012).
- [66] L.-A. Wu, H. J. Kimble, J. L. Hall, and H. Wu. Generation of squeezed states by parametric down conversion. *Phys. Rev. Lett.*, **57**, 2520 (1986).

- [67] H. Vahlbruch, S. Chelkowski, B. Hage, A. Franzen, K. Danzmann, and R. Schnabel. Demonstration of a squeezed-light-enhanced power- and signal-recycled Michelson interferometer. *Phys. Rev. Lett.*, **95**, 211102 (2005).
- [68] C. K. Law, H. Pu, and N. P. Bigelow. Quantum spins mixing in spinor Bose-Einstein condensates. *Phys. Rev. Lett.*, **81**, 5257 (1998).
- [69] O. Topic. *Resonante Spindynamik in Bose-Einstein-Kondensaten*. PhD thesis, Leibniz Universität Hannover (2010).
- [70] C. C. Gerry and P. Knight. *Introductory quantum optics*. Cambridge University Press (2005).
- [71] N. Bogolubov. On the theory of superfluidity. *J. Phys*, **11**, 23 (1947).
- [72] J. Kronjäger, C. Becker, P. Navez, K. Bongs, and K. Sengstock. Magnetically tuned spin dynamics resonance. *Phys. Rev. Lett.*, **97**, 110404 (2006).
- [73] M. Scherer, B. Lücke, G. Gebreyesus, O. Topic, F. Deuretzbacher, W. Ertmer, L. Santos, J. J. Arlt, and C. Klempt. Spontaneous breaking of spatial and spin symmetry in spinor condensates. *Phys. Rev. Lett.*, **105**, 135302 (2010).
- [74] T. Henninger. *Ultrakalte heteronukleare Feshbach Moleküle*. PhD thesis, Leibniz Universität Hannover (2008).
- [75] C. Klempt, T. van Zoest, T. Henninger, O. Topic, E. Rasel, W. Ertmer, and J. Arlt. Ultraviolet light-induced atom desorption for large rubidium and potassium magneto-optical traps. *Phys. Rev. A*, **73**, 13410 (2006).
- [76] C. Klempt, T. Henninger, O. Topic, J. Will, S. Falke, W. Ertmer, and J. Arlt. Transport of a quantum degenerate heteronuclear Bose-Fermi mixture in a harmonic trap. *Eur. Phys. J. D*, **48**, 121 (2008).
- [77] C. Klempt. *Wechselwirkung in Bose-Fermi-Quantengasen*. PhD thesis, Leibniz Universität Hannover (2007).
- [78] J. Will. Realisierung einer magneto-optischen Falle für ^{41}K . Master's thesis, Leibniz Universität Hannover (2007).
- [79] L. Kattner. Detection and stabilization of ultracold Feshbach-molecules. Master's thesis, Leibniz Universität Hannover (2008).
- [80] A. P. Kulosa. Aufbau eines Lasersystems zur Detektion und Manipulation von Atomen. Staatsexamensarbeit, Leibniz Universität Hannover (2009).
- [81] T. Esslinger, I. Bloch, and T. W. Hänsch. Bose-Einstein condensation in a quadrupole-Ioffe-configuration trap. *Phys. Rev. A*, **58**, R2664 (1998).

- [82] W. Ketterle and N. V. Druten. Evaporative cooling of trapped atoms. In B. Bederson and H. Walther, editors, *Advances In Atomic, Molecular, and Optical Physics*, volume 37 of *Advances In Atomic, Molecular, and Optical Physics*, pages 181 – 236. Academic Press (1996).
- [83] R. Grimm, M. Weidemüller, and Y. B. Ovchinnikov. Optical dipole traps for neutral atoms. *Adv. At. Mol. Opt. Phys.*, **42**, 95 (2000).
- [84] C. S. Adams, H. J. Lee, N. Davidson, M. Kasevich, and S. Chu. Evaporative cooling in a crossed dipole trap. *Phys. Rev. Lett.*, **74**, 3577 (1995).
- [85] F. Gerbier, A. Widera, S. Fölling, O. Mandel, and I. Bloch. Resonant control of spin dynamics in ultracold quantum gases by microwave dressing. *Phys. Rev. A*, **73**, 041602 (2006).
- [86] S. R. Leslie, J. Guzman, M. Vengalattore, J. D. Sau, M. L. Cohen, and D. M. Stamper-Kurn. Amplification of fluctuations in a spinor Bose-Einstein condensate. *Phys. Rev. A*, **79**, 043631 (2009).
- [87] E. M. Bookjans, C. D. Hamley, and M. S. Chapman. Strong quantum spin correlations observed in atomic spin mixing. *Phys. Rev. Lett.*, **107**, 210406 (2011).
- [88] M. Born and V. Fock. Beweis des Adiabatenatzes. *Zeitschrift für Physik*, **51**, 165 (1928).
- [89] T. Kato. On the adiabatic theorem of quantum mechanics. *J. Phys. Soc. Jpn.*, **5**, 435 (1950).
- [90] W. Warren. Effects of pulse shaping in laser spectroscopy and nuclear magnetic resonance. *Science*, **242**, 878 (1988).
- [91] M. Scherer. *Nichtklassische Zustände in Spinor-Bose-Einstein-Kondensaten*. PhD thesis, Leibniz Universität Hannover (2012).
- [92] N. F. Ramsey. A new molecular beam resonance method. *Phys. Rev.*, **76**, 996 (1949).
- [93] N. F. Ramsey. A molecular beam resonance method with separated oscillating fields. *Phys. Rev.*, **78**, 695 (1950).
- [94] J. F. Sherson, C. Weitenberg, M. Endres, M. Cheneau, I. Bloch, and S. Kuhr. Single-atom-resolved fluorescence imaging of an atomic Mott insulator. *Nature (London)*, **467**, 68 (2010).
- [95] W. S. Bakr, J. I. Gillen, A. Peng, S. Fölling, and M. Greiner. A quantum gas microscope for detecting single atoms in a Hubbard-regime optical lattice. *Nature (London)*, **462**, 74 (2009).

- [96] R. Bücker, A. Perrin, S. Manz, T. Betz, C. Koller, T. Plisson, J. Rottmann, T. Schumm, and J. Schmiedmayer. Single-particle-sensitive imaging of freely propagating ultracold atoms. *New J. Phys.*, **11**, 103039 (2009).
- [97] W. Muessel, H. Strobel, M. Joos, E. Nicklas, I. Stroescu, J. Tomkovič, D. B. Hume, and M. K. Oberthaler. Optimized absorption imaging of mesoscopic atomic clouds. *Applied Physics B*, **113**, 69 (2013).
- [98] D. B. Hume, I. Stroescu, M. Joos, W. Muessel, H. Strobel, and M. K. Oberthaler. Accurate atom counting in mesoscopic ensembles. *Phys. Rev. Lett.*, **111**, 253001 (2013).
- [99] T. Gericke, P. Wurtz, D. Reitz, T. Langen, and H. Ott. High-resolution scanning electron microscopy of an ultracold quantum gas. *Nat. Phys.*, **4**, 949 (2008).
- [100] P. Würtz, T. Langen, T. Gericke, A. Koglbauer, and H. Ott. Experimental demonstration of single-site addressability in a two-dimensional optical lattice. *Phys. Rev. Lett.*, **103**, 080404 (2009).
- [101] H. Metcalf and P. Van der Straten. *Laser cooling and trapping of atoms*. Springer, New York (1999).
- [102] G. Reinaudi, T. Lahaye, Z. Wang, and D. Guéry-Odelin. Strong saturation absorption imaging of dense clouds of ultracold atoms. *Opt. Lett.*, **32**, 3143 (2007).
- [103] W. Ketterle, D. Durfee, and D. Stamper-Kurn. Making, probing and understanding Bose-Einstein condensates. In *In Bose-Einstein condensation in atomic gases, Proceedings of the International School of Physics "Enrico Fermi", Course CXL* (1999).
- [104] A. Bick. Detektion und Untersuchung von mehrkomponentigen Bose-Einstein-Kondensaten in hexagonalen optischen Gittern. Master's thesis, Universität Hamburg (2010).
- [105] S. Chu, J. E. Bjorkholm, A. Ashkin, J. P. Gordon, and L. W. Hollberg. Proposal for optically cooling atoms to temperatures of the order of 10^{-6} K,. *Opt. Lett.*, **11**, 73 (1986).
- [106] H. Ammann and N. Christensen. Delta kick cooling: A new method for cooling atoms. *Phys. Rev. Lett.*, **78**, 2088 (1997).
- [107] C. F. Ockeloen, A. F. Tauschinsky, R. J. C. Spreeuw, and S. Whitlock. Detection of small atom numbers through image processing. *Phys. Rev. A*, **82**, 061606 (2010).
- [108] L. Pezzé and A. Smerzi. Entanglement, nonlinear dynamics and the Heisenberg limit. *Phys. Rev. Lett.*, **102**, 100401 (2009).

- [109] S. L. Braunstein and C. M. Caves. Statistical distance and the geometry of quantum states. *Phys. Rev. Lett.*, **72**, 3439 (1994).
- [110] P. Hyllus, L. Pezzé, and A. Smerzi. Entanglement and sensitivity in precision measurements with states of a fluctuating number of particles. *Phys. Rev. Lett.*, **105**, 120501 (2010).
- [111] J. Ma, X. Wang, C. Sun, and F. Nori. Quantum spin squeezing. *Phys. Rep.*, **509**, 89 (2011).
- [112] M. J. Holland and K. Burnett. Interferometric detection of optical phase shifts at the Heisenberg limit. *Phys. Rev. Lett.*, **71**, 1355 (1993).
- [113] Z. Y. Ou, J.-K. Rhee, and L. J. Wang. Observation of four-photon interference with a beam splitter by pulsed parametric down-conversion. *Phys. Rev. Lett.*, **83**, 959 (1999).
- [114] T. Nagata, R. Okamoto, J. L. O’Brien, K. Sasaki, and S. Takeuchi. Beating the standard quantum limit with four-entangled photons. *Science*, **316**, 726 (2007).
- [115] V. Meyer, M. A. Rowe, D. Kielpinski, C. A. Sackett, W. M. Itano, C. Monroe, and D. J. Wineland. Experimental demonstration of entanglement-enhanced rotation angle estimation using trapped ions. *Phys. Rev. Lett.*, **86**, 5870 (2001).
- [116] G. Breit and I. I. Rabi. Measurement of nuclear spin. *Phys. Rev.*, **38**, 2082 (1931).
- [117] C. K. Hong, Z. Y. Ou, and L. Mandel. Measurement of subpicosecond time intervals between two photons by interference. *Phys. Rev. Lett.*, **59**, 2044 (1987).
- [118] A. White, D. James, P. Eberhard, and P. Kwiat. Nonmaximally entangled states: Production, characterization, and utilization. *Phys. Rev. Lett.*, **83**, 3103 (1999).
- [119] C. Schwemmer, G. Tóth, A. Niggebaum, T. Moroder, D. Gross, O. Gühne, and H. Weinfurter. Efficient tomographic analysis of a six photon state (2014).
- [120] M. Paris and J. Řeháček, editors. *Quantum State Estimation*, volume 649 of *Lecture Notes in Physics*, Springer Berlin Heidelberg (2004).
- [121] R. H. Dicke. Coherence in spontaneous radiation processes. *Phys. Rev.*, **93**, 99 (1954).
- [122] A. Chiuri, C. Greganti, M. Paternostro, G. Vallone, and P. Mataloni. Experimental quantum networking protocols via four-qubit hyperentangled Dicke states. *Phys. Rev. Lett.*, **109**, 173604 (2012).
- [123] R. Krischek, C. Schwemmer, W. Wieczorek, H. Weinfurter, P. Hyllus, L. Pezzé, and A. Smerzi. Useful multiparticle entanglement and sub-shot-noise sensitivity in experimental phase estimation. *Phys. Rev. Lett.*, **107**, 080504 (2011).

- [124] G. Tóth. Multipartite entanglement and high-precision metrology. *Phys. Rev. A*, **85**, 022322 (2012).
- [125] P. Hyllus, W. Laskowski, R. Krischek, C. Schwemmer, W. Wieczorek, H. Weinfurter, L. Pezzé, and A. Smerzi. Fisher information and multiparticle entanglement. *Phys. Rev. A*, **85**, 022321 (2012).
- [126] G. Tóth, C. Knapp, O. Gühne, and H. Briegel. Optimal spin squeezing inequalities detect bound entanglement in spin models. *Phys. Rev. Lett.*, **99**, 250405 (2007).
- [127] G. Vitagliano, I. Apellaniz, I. n. L. Egusquiza, and G. Tóth. Spin squeezing and entanglement for an arbitrary spin. *Phys. Rev. A*, **89**, 032307 (2014).
- [128] L.-M. Duan. Entanglement detection in the vicinity of arbitrary Dicke states. *Phys. Rev. Lett.*, **107**, 180502 (2011).
- [129] R. Folman, P. Krueger, J. Schmiedmayer, J. Denschlag, and C. Henkel. Microscopic atom optics: from wires to an atom chip. *Adv. At. Mol. Opt. Phys.*, **48**, 263 (2002).
- [130] L. Pezzé and A. Smerzi. Ultrasensitive two-mode interferometry with single-mode number squeezing. *Phys. Rev. Lett.*, **110**, 163604 (2013).
- [131] A. Stuart and K. Ord. *Kendall's Advanced Theory of Statistics: Volume 1: Distribution Theory*. Wiley (2009).

Publications

- *Detecting multiparticle entanglement of Dicke states*
B. Lücke, J. Peise, G. Vitagliano, J. J. Arlt, L. Santos, G. Tóth, and C. Klempt
Phys. Rev. Lett., 112:155304 (2014)
- *Spontaneous symmetry breaking in spinor Bose-Einstein condensates*
M. Scherer, B. Lücke, J. Peise, O. Topic, G. Gebreyesus, F. Deuretzbacher, W. Ertmer, L. Santos, C. Klempt and J. J. Arlt
Phys. Rev. A, 88:053624 (2013)
- *Twin matter waves for interferometry beyond the classical limit*
B. Lücke, M. Scherer, J. Kruse, L. Pezzé, F. Deuretzbacher, P. Hyllus, O. Topic, J. Peise, W. Ertmer, J. Arlt, L. Santos, A. Smerzi and C. Klempt
Science, 334(6057):773-776 (2011)
- *Spontaneous breaking of spatial and spin symmetry in spinor condensates.*
M. Scherer, B. Lücke, G. Gebreyesus, O. Topic, F. Deuretzbacher, W. Ertmer, L. Santos, J. J. Arlt and C. Klempt
Phys. Rev. Lett., 105(13):135302 (2010)
- *Parametric amplification of matter waves in dipolar spinor Bose-Einstein condensates*
F. Deuretzbacher, G. Gebreyesus, O. Topic, M. Scherer, B. Lücke, W. Ertmer, J. Arlt, C. Klempt, and L. Santos
Phys. Rev. A, 82:053608 (2010)
- *Aufbau und Planung einer Hybridfalle zur Erzeugung ultrakalter Quantengase*
B. Lücke
Diploma thesis (2009)

Lebenslauf

Persönliche Daten

Name	Bernd Lücke
Geburtsdatum/-ort	30.11.1982 in Clausthal-Zellerfeld, Deutschland
Familienstand	ledig

Promotions-Studium

seit August 2009	Doktorarbeit am <i>Institut für Quantenoptik</i> der <i>Leibniz Universität Hannover</i>
------------------	--

Studium

06/2008 - 06/2009	Diplomarbeit am <i>Institut für Quantenoptik</i> der <i>Leibniz Universität Hannover</i> mit dem Thema "Aufbau und Planung einer Hybridfalle zur Erzeugung ultrakalter Quantengase"
2007-2008	Auslandsaufenthalt in Lyon an der <i>Université Claude Bernard</i> im Rahmen des <i>Erasmus</i> -Programms
2003-2009	Studium der Physik an der <i>Leibniz Universität Hannover</i>

Zivildienst

2002-2003	Zivildienst in der <i>Klinik Erbprinzentanne</i> in Clausthal-Zellerfeld
-----------	--

Schulabschluss

2002	Abitur am <i>Robert-Koch-Gymnasium</i> in Clausthal-Zellerfeld
------	--